A Modular and Scalable Architecture for Millimeter-Wave Beam-forming Antenna Systems

by

HUSSAM HUSSIEN ALI AL-SAEDI

A thesis
presented to the University of Waterloo
in fulfillment of the
thesis requirement for the degree of
Doctor of Philosophy
in
Electrical and Computer Engineering

Waterloo, Ontario, Canada, 2018

Examination Committee Members

The following served on the Examining Committee for this thesis.

External Examiner	Lotfollah Shafai Professor
Supervisor(s)	Safieddin Safavi-Naeini Professor
Internal Member	Slim Boumaiza Professor
Internal Member	Raafat Mansour Professor
Internal-external Member	Ehsan Toyserkani Professor

AUTHOR'S DECLARATION

I hereby declare that I am the sole author of this thesis. This is a true copy of the thesis, including any required final revisions, as accepted by my examiners.

I understand that my thesis may be made electronically available to the public.

Abstract

As the demand for higher data rates increases, wireless technologies (e.g., satellite communications, fifth Generation (5G) wireless communications, and automotive radars) are migrating toward millimeter-wave (mm-W) frequencies (30-300 GHz) to utilize the numerous unused spectra available over this frequency band. For truly ubiquitous coverage over the globe, high throughput Ka-band satellite communication (SATCOM) offers the most optimal and a unique solution for providing world-wide information and sensing. Of particular interest is the development of land, or close-to-land, mobile systems for high data rate communications with continuous coverage for on-the-move commercial platforms, including cars, airplanes, ships, and trains. A modular and scalable phased-array antenna (PAA) architecture wherein the entire phased-array system is made of identical sub-array modules (building blocks) is the most promising approach to develop cost effective and flexible systems for mass market applications. Obviously, such architecture depends on the availability of a high-performance antenna element, antenna subarray modules, and beam-forming circuits. These are the main topics investigated in this PhD thesis. Two approaches were extensively studied in this PhD research to develop intelligent steerable antenna array modules as building blocks for large-scale Ka-band SATCOM applications.

The first approach targeted the development of a working prototype for a wide-angle beam-steering Ka-band active PAA (APAA). In this approach, two APAA architectures were proposed, designed, fabricated, and measured to validate the proposed concepts. Both approaches exhibit wide beam-steering angles and fast beam-forming capabilities with full control on amplitude and phase of each antenna element by utilizing an intelligent beam-forming circuit that was developed at CIARS (Centre for Intelligent Antenna and Radio Systems). The first architecture comprises a novel single-fed CP antenna element integrated with the intelligent beam-forming circuit, to construct a wide beam-steering and low-cost CP-APAA. A 4×16 CP-APAA was designed and fabricated using low-cost printed circuit board (PCB) technology and it was tested over the frequency range (29.5-30 GHz) over an angular range of 0^{o}-$\pm 40^{o}$. The second architecture utilized a highly integrated and wide band dually-polarized antenna element as a core component for the realization of a high-performance, compact, and polarization-agile Ka-band APAA module. The proposed antenna module was used to construct a proof-of-concept 16×16 modular APAA to radiate a high polarization purity pattern over a wide beam-steering angles $\geq 70^{o}$.

The second proposed approach investigated two novel wideband and passive steerable antenna concepts as attractive low-cost alternatives suitable for a wide range of emerging mm-W communication systems. Such antenna systems are made of passive components, antennas, phase shifters, and passive feeding networks to reduce the power consumption, cost, and complexity of conventional active electronically steered arrays. In order to build such systems, a high-performance antenna and passive phase shifter (invented at CIARS) were integrated to eliminate the necessity for costly variable gain amplifiers (VGAs). The first proposed concept is a novel CP passive PAA comprised of the proposed single-fed CP antenna integrated with the CIARS phase shifter. The novel high-performance passive phase shifter was controlled by a low-profile and low-power consumption novel magnetic actuator to overcome the limitation of state-of-the-art passive phased arrays. The proposed CP passive PAA was designed, fabricated and tested at Ka-band (29.5-30.5 GHz) over an angular range of 0^{o}-$\pm 38^{o}$. The second concept proposed here is a novel reconfigurable reflectarray antenna (RAA) element with a true-time-delay functionality. Its reconfigurability is realized by utilizing the proposed phase shifter integrated with an aperture-coupled microstrip patch antenna (ACMPA) to receive and re-radiate the electromagnetic energy efficiently. The proposed RAA element was designed and tested at Ka-band (27.5-30 GHz).

Acknowledgements

I would like to express my sincere gratitude to my supervisor Prof. Safieddin Safavi-Naeini for his supervision, brilliant ideas, fruitful discussions, financial support, and continuous support.

My sincere thanks to Prof. Lotfollah Shafai from University of Manitoba for accepting to be the external examiner of my PhD defense. I am thankful to the examination committee members from the University of Waterloo, Prof. Slim Boumaiza, Prof. Raafat Mansour, Prof. Ehsan Toyserkani, and Prof. James Martin.

My deep gratitude, appreciation, and love to my wife who has always supported me patiently and lovingly. I wish also to express my love and gratitude to my family back home in Iraq and here in Canada: my dear father who left this world recently, my dear mother, my brothers, my sisters, and my three cute kids.

Special thank you to Dr. Suren Gigoyan from CIARS for his significant contributions on the BLT-based phase shifters, Dr. Wael M. Abdel-Wahab form CIARS for his important contribution on APAA developments, antenna measurements, and research collaborations, and Prof. Raj Mittra from University of Central Florida for his discussions, valuable ideas, guidance, and fruitful research collaborations.

I also want to thank Dr. Aidin Taeb from CIARS who taught me how to use the planar near-field antenna measurement system. Engineer Ardeshir Palizban from CIARS for his excellent technical support. Dr. Ahmed Ehsandar from CIARS for his help and support on mechanical support structures. Dr. S. Mohsen Raeis-Zadeh former CIARS member and Dr. Ehsan Haj Mirza Alian for their brilliant wok on calibration and beamforming algorithms for APAAs. Thank you to all CIARS members for their help, friendship, and research collaboration; I learned a lot here at CIARS group. Thank you to my special friend Chris Schroeder: grazie amica.

I am thankful to my Professor at the University of Technology, Iraq, Professor Dr. Jawad K. Ali who provided me a unique opportunity to study and work in Electromagnetics.

Finally, I want to thank the Iraqi Ministry of Higher Education and Scientific Research for the financial support as well as the industrial partners C-COM Satellite Systems Inc. and Bombardier Aerospace Inc. for giving me the opportunity to be involved in their R&D plans.

Dedication

To the soul of my Father whom I miss a lot and did not get the chance to say goodbye. I will always miss you.

To my Mother

To my wife

To my Kids

To my family

To my friends

Table of Contents

List of Figures

List of Tables

Chapter 1
Introduction

1.1 Introduction

As the demand for higher data rates increases, wireless technologies (e.g., satellite communications, 5G, and automotive radar) are migrating toward millimeter-wave (mm-W) frequencies (30-300 GHz) to utilize the numerous unused spectra available over this frequency band [1-40]. For truly ubiquitous coverage over the globe, high throughput Ka-band satellite communication (SATCOM) offers the most optimal and a unique solution for providing world-wide information and sensing. Such a system will extend the boundaries of the digital economy to remote areas that terrestrial wireless systems can never reach. Of particular interest is the development of land, or close-to-land, mobile systems for high data rate communications with continuous coverage for on-the-move commercial platforms, including cars, airplanes, ships, and trains [1-2, 4-10, 12-14, 19-23, 31, and 36-39]. Low-profile active intelligent antenna systems, such as phased-array antennas (PAAs), are considered to be the most promising radio architectures for such applications. PAA systems can offer low-profile, highly conformal, and flexible solutions with fast beam-scanning, as compared to reflector antennas or fixed-beam array antennas [1-2, 5, 21, and 36-37]. These unique features are on high demand for emerging Ka-band mobile SATCOMs, for which essential requirements are: low-profile configuration, conformal geometry, rapid multi-beam tracking, high gain, very low side-lobe level (SLL), and a high purity circularly polarized (CP) radiation pattern over the entire scanning range. The PAA beam should be steerable over a wide angular range of $\pm 70^{o}$ in elevation and 360^{o} in azimuth, over a wide frequency range (> 2 GHz) in Ka-band. For commercial satellite mobile terminals, the radiation power density should follow a highly stringent standard mask. Usually, a large antenna aperture is utilized to increase the gain to overcome the path loss at Ka-band and sustain a robust communication link with geostationary earth orbit (GEO) and low earth orbit (LEO) satellites, over the entire range of scan angle [1-2,4, 7, 21, 36-37, and 39]. Moreover, highly complex multilayered feeding and calibration circuitry are required for such systems. As a result, a PAA that meets mobile SATCOMs operational requirements is a highly complex, high performance, and large-scale array antenna structure. Existing phased-array technologies [21], despite their obviously superior performance, have not yet been implemented in large-scale commercial mobile satellite networks to their high-cost, high-profile, and high implementation and manufacturing complexities.

1.2 Drawbacks of current Ka-band SATCOM solutions

Existing relatively low-cost solutions such as reflector antennas [41] and fixed beam antennas with mechanical steering [38] are not suitable for satellite on-the-move (SOTM) applications because of their high-profile and slow mechanical beam-steering [42]. Digital beam-forming based solutions [21 and 56] are high-cost, complex, and high-profile compared to analog PAA. On the other hand, building a complex and large-scale PAA with printed circuit board (PCB) technology is a challenging task for fabrication companies and fabrication errors are inevitable; moreover, such structures required high-cost and time-consuming maintenance servicing [43]. Furthermore, it is very difficult for such large and complex boards to conform over curved surfaces—this is crucial requirement when developing a communication system that will be deployed on moving terminals (e.g., airplanes, cars, trains, and ships) with minimal aerodynamic drag. Other challenges associated with current solutions are the performances limitations of the building blocks (antennas, phase shifters, amplifiers, and feed circuit) of the PAA such as limited operating frequency bandwidth, limited beam-steering range, high mutual coupling, high power consumption, amount of heat generated, large size, and packaging/integration complexities.

1.2.1 Limitations of the building blocks

Electronic beam-scanning capability is the major advantage of active PAAs (APAAs). However, this capability requires high-performance building blocks such as antennas, phase shifters, amplifiers, and switches. Such components need to be simple, compact, wide band, low-cost, low-power consumption, and low loss. Planar antenna technologies typically operate over a limited frequency bandwidth of <5%, and as the spacing between the adjacent elements is reduced to $\leq 0.5\lambda_o$ the mutual coupling increases significantly. In the case of low elevation scanning angles and large-scale phased arrays, this leads to large impedance variation of the antenna elements. As a result, there is a reduction in the overall system efficiency as well as more power consumption and generated heat. Furthermore, the antenna element should be simple and have a wide operating frequency band. It would be required to demonstrate high cross-polarization (X-pol) discrimination over a wide angular beam-width to sustain a high-quality data link and avoid undesired interferences [44-50]. Phase shifter is one of the most critical components in the development of a PAA. By controlling the phase of each individual phase shifter, the beam of the antenna can be steered towards a specific direction. The phase shifter must have low insertion loss (IL) variation over the operating frequency range to eliminate the necessity for costly high-performance variable gain amplifiers (VGAs). State-of-the-art

phase shifters usually suffer from high IL as well as high IL variation; as a consequence, a high dynamic range VGA or attenuator is required to mitigate the phase shifter's performance [51].

1.2.2 Cost and complexity

The cost and complexity of active feed circuits have seriously limited the deployment of active PAA in mass market applications. As a PAA consists of a large number of different components as well as large complex PCBs, the cost of such systems has been beyond the reach of customers for commercial applications. Furthermore, integrating multiple radio frequency (RF) components within a small area is still a challenging task due to cost/complexity of automatized fabrication processes and fine feature patterning. However, recent advances in commercial monolithic microwave/mm-W integrated circuit (MMIC) technologies [29, 35-37], as well as novel passive device technologies [51 and 114-115], have created new possibilities for implementing active beam-steering front-ends in a highly cost-effective manner. Moreover, the advances in multi-layer PCB fabrication and additive manufacturing have contributed hugely to the development of very complicated but cost-effective multi-layer fabrication technologies with flexible and solid substrates [52-55]. As a result, the development of conformal PAAs that use low-cost technology and fabrication processes for mm-W applications are soon becoming affordable.

1.3 Objectives of this research

In this section, the main objectives of this research are explained, and their importance is highlighted. A modular and scalable PAA architecture wherein the entire phased-array system is made of identical sub-array modules (building blocks) is the most promising, flexible, and cost-effective approach to develop large-scale phased-array systems for mass market applications. There are four main advantages with this approach. i) It is low-cost and can be quickly maintained. ii) A flexible and scalable PAA architecture can be developed easily by choosing the optimal array shape without redesign of the antenna modules. iii) It can be deployed on flat or curved platforms. iv) Building a modular PAA with discrete modules reduces undesired surface wave modes and mutual couplings between the antenna modules since the modules do not share the same dielectric substrate and ground. Obviously, such architecture depends on the availability of a high-performance antenna element, antenna subarray modules, and beam-forming circuits. These are the main topics investigated in this PhD thesis. Two approaches were extensively studied in this PhD research to develop an intelligent antenna array module as a building block for Ka-band SATCOM systems.

Figure **1.1** illustrates the proposed solutions that were developed and investigated in this PhD thesis. Figure **1.2** demonstrates CIARS modular and scalable two-way APAA architecture that employs the proposed solutions of this PhD research for commercial SATCOM applications.

1.3.1 A wideband, modular, and scalable mm-W APPA architecture for wide beam-steering

The first approach targeted the development of a working prototype for a wide beam-steering Ka-band active PAA (APAA). In this approach, two APAA architectures were proposed, investigated, fabricated, and measured to validate the proposed concepts. The first architecture uses a novel single-fed CP antenna element integrated with CIARS (Centre for Intelligent Antenna and Radio Systems) intelligent beam-forming module, to construct a high-performance CP-APAA for wide beam-steering SATCOM system. A 4×16 CP-APAA was designed and fabricated using three-metal layers low-cost printed circuit board (PCB) technology as a proof-of-concept. The intelligent beam-forming circuit was used to control both the amplitude and the phase of the 64 antenna elements independently. The proposed CP-APAA was tested over a wide scanning range from 0^o to $\pm 40^o$ in the elevation. Furthermore, the SLL of the radiation pattern was successfully controlled by tapering the power level over the antenna aperture. Also, it was shown that the same structure can be used to generate multiple beams. In one example, two different beams were simultaneously generated with different scan angles and unequal power levels. The second architecture utilized a highly integrated and wide band dually-polarized antenna element as a core component for the realization of a high-performance, compact, and polarization-agile Ka-band APAA module to meet the stringent requirements of on-the-move SATCOM system. The proposed antenna module was used with CIARS intelligent beam-forming circuit to construct a proof-of-concept 16×16 modular APAA. The proof-of-concept was successfully measured over a wide frequency band (28-31 GHz) for wide beam-steering angles (0^o-60^o).

1.3.2 A novel low-cost mm-W steerable antenna

The second proposed approach investigated two novel wideband and passive steerable antenna concepts as attractive low-cost alternatives suitable for wide range of emerging mm-W communication systems. Such antenna systems are made of passive components, antennas, phase shifters, and passive feeding networks to reduce the power consumption, cost, and complexity of conventional active electronically steered arrays. Furthermore, a single passive steerable antenna array made of reciprocal components was investigated to work both as a transmitter element and a

receiving element. In order to build such systems, a high-performance antenna and passive phase shifter, advanced at CIARS, were developed and integrated to eliminate the necessity for costly variable gain amplifiers (VGAs). The first proposed concept is a novel CP passive PAA comprised of a single-fed CP antenna integrated with the aforementioned high-performance passive phase shifter. The novel high-performance passive phase shifter was controlled by a low-profile and low-power consumption novel magnetic actuator to overcome the limitation of state-of-the-art passive phased arrays. The proposed CP passive PAA was designed, fabricated and tested at Ka-band. It showed a high-performance CP radiation with high cross-polarization discrimination over wide scan angles from 0^{o} to $\pm 38^{o}$ over the frequency band (29.5-30.5 GHz). The second concept proposed here is a novel reconfigurable reflectarray antenna (RAA) element with a true-time-delay functionality. Its reconfigurability is realized by utilizing the proposed phase shifter integrated with an aperture-coupled microstrip patch antenna (ACMPA) to receive and re-radiate the electromagnetic energy efficiently. The proposed RAA element was designed and tested over the frequency range of 27.5-30 GHz. Measurements show that a reflection phase of almost 360^{o} can be realized over an 8.7% frequency band with a maximum reflection loss of 4.5 dB.

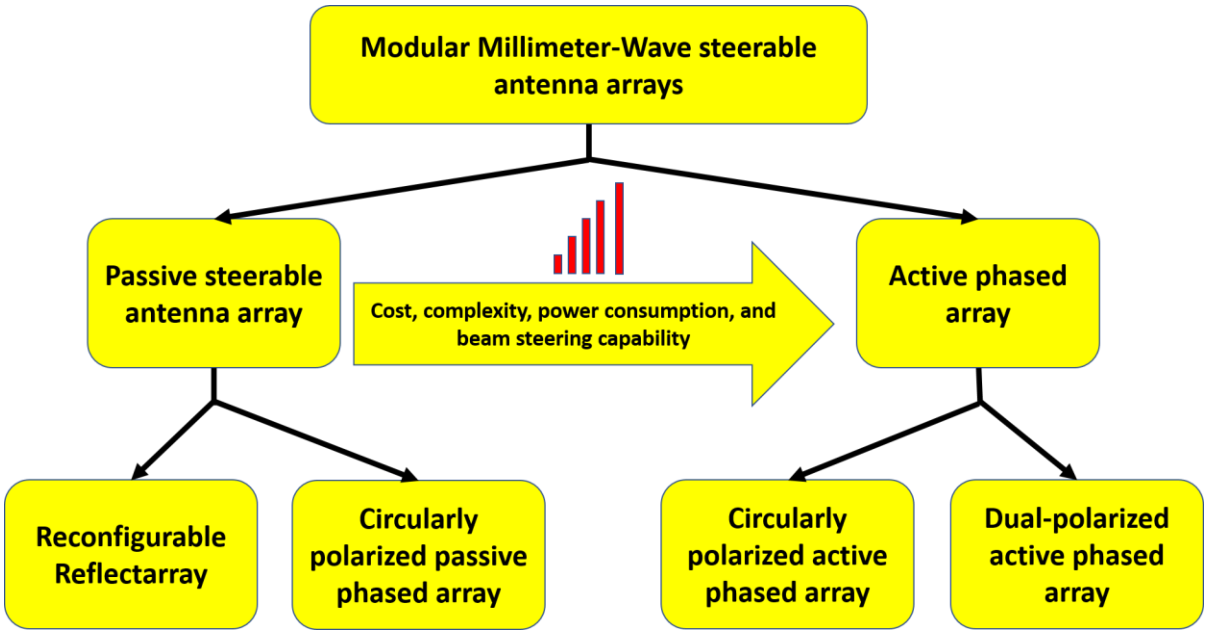

Figure 1.1: Thesis flow.

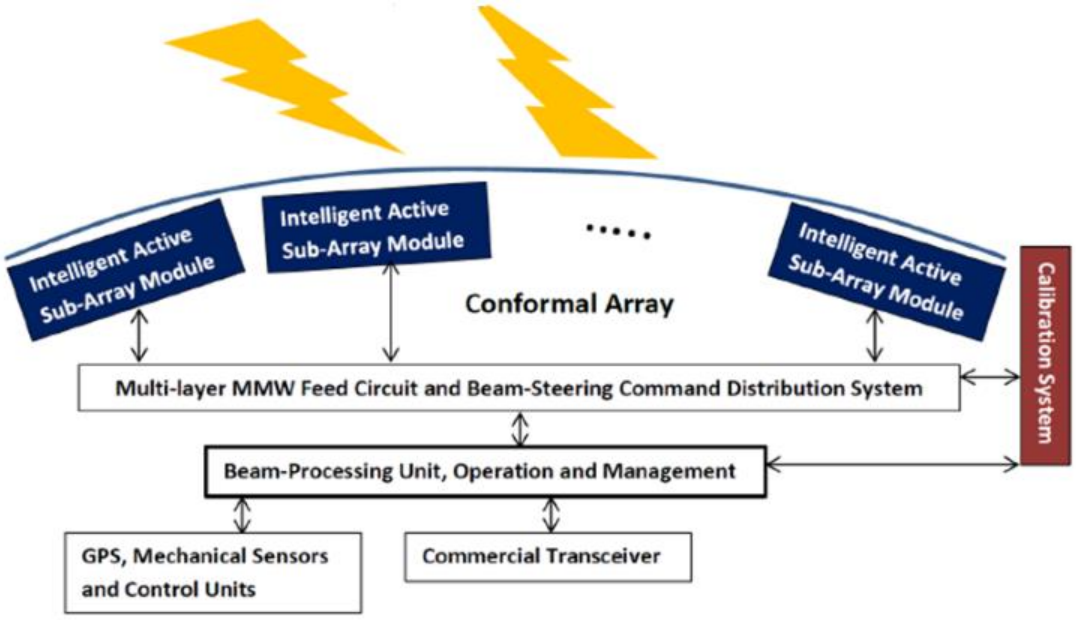

Figure 1.2: CIARS two-way architecture of APAA.

1.4 Outline of this thesis

Chapter 2 of this thesis provides theoretical background and a literature review of state-of-the-art configurations. The limitations and drawbacks of the available solutions are discussed to highlight the importance of this thesis research, which provides new and effective solutions to overcome these limitations and drawbacks.

Chapter 3 introduces a novel single-fed CP antenna with an active reflection coefficient <-10 dB, over the elevation (θ), at angular range of 0°-60° in all azimuthal (φ) ranges. Moreover, it shows a wide AR beam-width to sustain circular polarization over the elevation (θ) angular range of 0°-40° over the entire azimuthal (φ) range (360°). Using a commercial three-metal-layer low-cost PCB process, a 4×16 CP-APAA, incorporating the aforementioned CP antenna element, was developed. This structure was used as a proof-of-concept for the first approach studied. The proposed CP-APAA was tested over a wide scanning range from 0° to ±40° in the elevation. Furthermore, the SLL of the radiation pattern was successfully controlled by tapering the power level over the array antenna aperture. Also, it was shown that the same structure could generate multiple CP beams.

Chapter 4 presents a dual-fed and dual-polarized antenna that, once incorporated into CIARS intelligent beam-forming module, offered an active reflection coefficient <-10 dB over the elevation (θ), at an angular range of 0°-50° in all azimuthal (φ) range (360°). The antenna sub-array was

fabricated by an advanced multi-layer PCB technology to realize a modular APAA for Ka-band SATCOMs. A proof-of-concept for wide band (3 GHz) and wide beam-steering (≥70^{o}) operation was developed and measured.

Chapter 5 discusses the development of a low-cost and high-performance phase shifter. This phase shifter yields a high figure of merit (FOM) that paves the way to develop a high-performance passive PAA. Moreover, a low-cost, low-profile, and low power consumption magnetic actuation developed at CIARS is presented as a practical solution to control the phase response of the proposed phase shifter.

Chapter 6 provides details of a proposed low-cost, low-profile, and a compact CP passive PAA. This passive PAA is presented as a promising solution for mm-W applications. The PAA was investigated, fabricated, and successfully tested. The novel CP antenna proposed in chapter 4 integrated with the high-performance passive phase shifter, developed in Chapter 5, is presented and experimentally verified. The proposed CP passive PAA achieves high performance RHCP radiation with high cross-polarization discrimination over a wide scanning angle from 0^{o} to ±38^{o} over the frequency band (29.5-30.5 GHz). An AR< 3dB is demonstrated over the entire scanning angle. Then, a novel reconfigurable RAA element with true-time-delay functionality is presented. The proposed RAA element was designed and tested over the frequency range of 27.5-30 GHz.

Finally, chapter 7 concludes the thesis by summarizing the findings of the research and suggesting several directions for future research.

Chapter 2
Background and Literature Review

2.1 Introduction

This chapter briefly reviews some basic concepts, techniques, and state-of-the-art technologies available in the literatures. The chapter starts with system requirements for Ka-band SATCOMs. A simple definition of PAA will be provided along with a brief discussion of recent world-wide efforts for applying this technology to SOTM applications, specifically the most promising ones, with an emphasis on array antenna concepts that offer beam-steering features with a conformal or low-profile configuration. The concept of steerable RAA is also presented below followed by a discussion of state-of-the-art methodology in this field. Finally, a review of state-of-the-art phase shifters is provided, and their limitations and drawbacks are highlighted.

2.2 Ka-band SATCOMs

The proliferation of smart phones, tablets and mobile satellite receivers coupled with an increased demand for high quality entertainment, media, and data services for on-the-move terminals (e.g., automobiles, trains, ships, airplanes), emphasizes the need for high data-rate communication links. In this aspect, Ka-band mobile SATCOMs have received considerable attention. Such communication system requires a low-profile robust antenna system to dynamically track the satellite when the terminal is moving and maneuvering [1-2,4, 7, 21, 36-37, and 39]. This thesis research focuses on investigation and development of a steerable-beam modular antenna system architecture for SOTM applications at Ka-band (27.5-31 GHz). Typical applications of a SOTM two-way communication system [31] are shown in Figure 2.1. The most fundamental and stringent requirements of SOTM systems are [1-2,4, 7, 21, 36-37, 39, 60]:

- A high effective isotropic radiated power (EIRP) of the order of 48 to 50 dBW, required to provide users with a reliable high data rate connectivity.
- Dual-band operation, 20 GHz downlink and 30 GHz uplink with 500 MHz frequency bandwidth.
- Fulfill Federal Communications Commission (FCC) mask requirement for the radiation pattern across the entire scanning range (see Figure 2.2) [56-60].

- Switchable CP with cross-polarization (X-pol) discrimination better than 20 dB for all scan angles.
- Fast beam steering capability covering ±70˚ in elevation, and 360˚ in azimuth.
- Low profile, conformal and lightweight.
- High beam pointing accuracy (<0.2º) to prevent interference with the adjacent satellites.

Addressing the abovementioned requirements is a highly challenging task, and to the best of the author's knowledge, there is no existing commercial products or reported R&D prototype that satisfy all of these requirements on APAA. Conventional antennas used in the commercial sector are based on mechanically-scanned beam reflectors or hybrid configurations. Low profile SOTM PAAs are still the subject of intense research and development efforts world-wide [8].

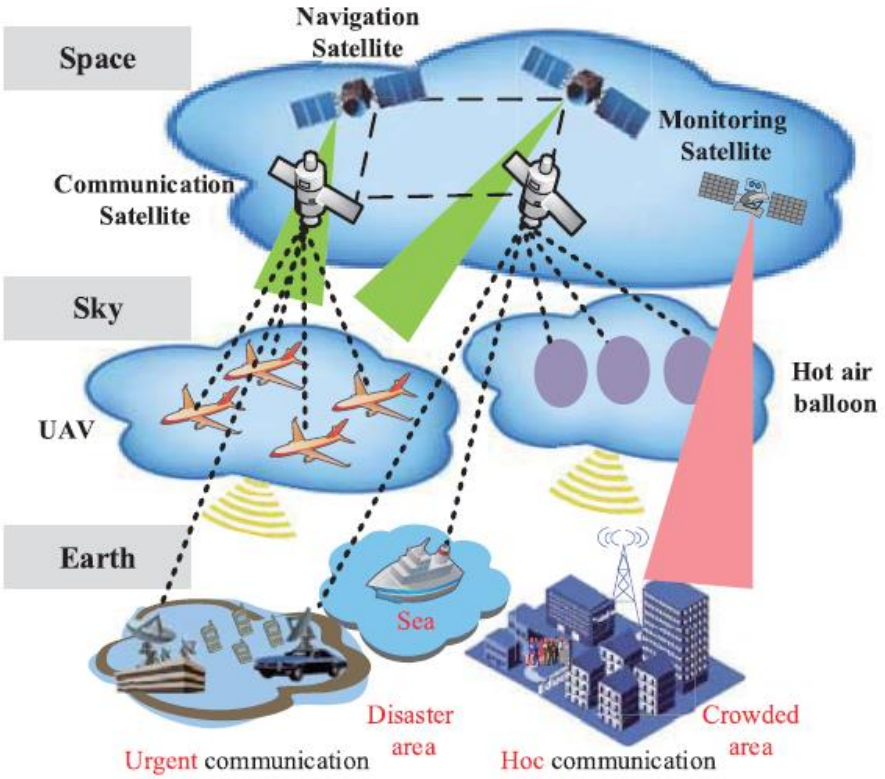

Figure 2.1: SOTM two-way communication system [31] © 2018 IEEE.

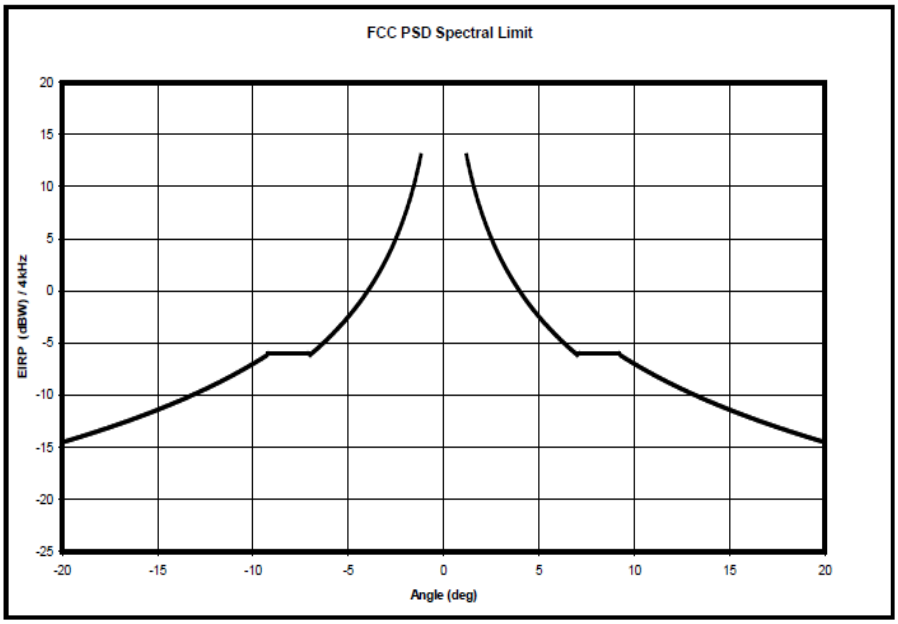

Figure 2.2: FCC spectral mask [60].

2.3 Antenna

2.3.1 Planar antenna

Planar antennas have been extensively employed for a vast number of applications due to their numerous advantages. Lightweight, low profile, mature fabrication technology, ease of integration and packaging, and design flexibility are among the most important features that planar antenna technology offers [7, 21, 42, 44, and 61-63]. The planar antenna in its basic configuration is comprised of two metal layers, namely the radiator and ground, and these metal layers are mounted on a dielectric substrate that is used for mechanical support and size reduction. The radiator can be of any shape as long as it is designed to radiate the required radiation pattern at the operating frequency. However, antenna experts tend to use regular geometries such as rectangles, squares, circles, ellipticals, tringles, and annular rings because of the availability of analytical formulations for such structures, which makes the antenna design and optimization simple and fast [6]. In general, planar antenna feeds are classified into two main types: direct and indirect feed structures. A direct feed antenna is realized through direct physical connection between the feed [e.g., transmission line (TL) or pin] and the radiator. On the other hand, an indirect feed antenna is realized by electromagnetic coupling [e.g., capacitive or inductive] between the feed and the radiator. Microstrip fed and coaxial pin fed are examples of direct feed antennas, and proximity fed and aperture-coupled are examples of

indirect feed antennas [61]. Among all feed structures, ACMPA (aperture-coupled microstrip patch antenna) exhibits better performance—wider operating frequency bandwidth and lower spurious feed radiation, and compatibility for MMIC integration [63].

Typically, an ACMPA consists of three metal layers and two dielectric substrates, as shown in Figure 2.3. The top metal layer is a microstrip patch, the middle metal layer is a common ground with aperture coupling slot, and the bottom metal layer is a TL that couples the electromagnetic field to the microstrip patch through the aperture slot. The ACMPA gives more degrees of freedom to efficiently design both the patch and the TL since two dielectric substrates are employed in its realization. The antenna's substrate usually has a low dielectric constant (ε_r =1-4) chosen to achieve higher radiation efficiency and wider frequency bandwidth. The feed's substrate usually has a high dielectric constant (ε_r =4-12) to miniaturize the TL dimensions and confine the propagating electromagnetic field locally [61]. The microstrip patch usually is a half-guided wave length ($\lambda_g/2$) resonator that generates the dominant resonance mode and can be easily excited with a simple feed structure. The aperture slot behaves as an impedance transformer with a transformation ratio of n:1 to match the patch impedance to the TL feed. The feed line usually has a 50Ω characteristic impedance for ease of integration with MMICs. An open stub with a quarter-wave length ($\lambda_g/4$) is connected to the 50Ω TL for impedance matching [63].

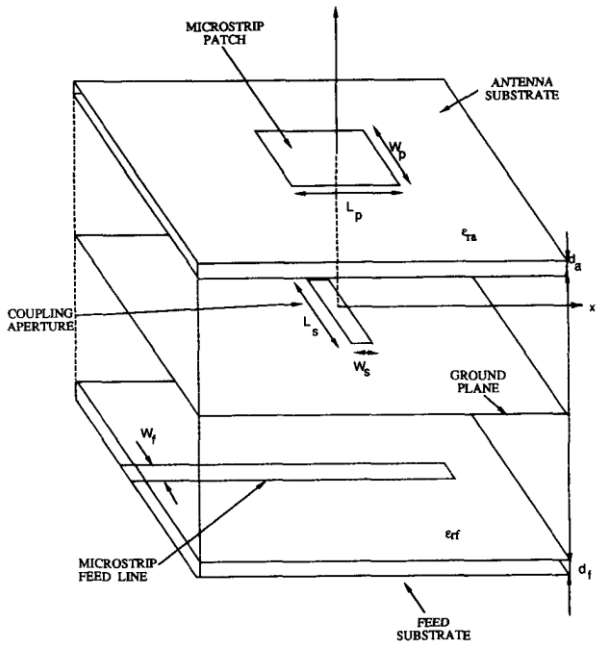

Figure 2.3: ACMPA typical structure [63] © 1989 IEEE.

An ACMPA can be used to generate a linearly polarized (LP) or CP pattern [63-64]. ACMPAs have been reported in the literature with single or dual feeds for CP antenna realization. A Single-fed CP aperture-coupled antenna is a simple structure and requires less beam-forming components than the dual-fed antenna. However, single feed antenna shows a narrower impedance and axial ratio (AR) bandwidths compared with dual feed version. Dual-fed antenna also has the capacity for polarization switchability and polarization purity enhancement. In a single-fed aperture-coupled antenna, CP can be generated by modifying the microstrip patch or the slot to generate two orthogonal degenerate modes with the same amplitude and a 90° phase difference. The microstrip patch can be modified to generate a CP pattern either by adding or subtracting a perturber located at 45° from the feed point, and an analytical formulation has been developed in the literature to calculate the required size of the perturber for some typical patch antennas [62]. On the other hand, the aperture slot can be modified in such a way that the microstrip patch is excited with two orthogonal modes to generate the CP pattern [65].

2.3.2 CP (circularly polarized) antenna

To generate a CP pattern, two electrical-field (E-field) components are required with the same amplitude and a 90° phase difference between them. Despite its design complexity compared to LP antenna, CP is used in SATCOMs due to its immunity to Faraday rotation, mitigation of multipath propagation, and insensitivity to transmitter and receiver misalignment [66-68]. The E-field ($\vec{E}(x,y)$) in the polarization plane can be decomposed into two components [69] x-component ($E_{xo}(x,y)e^{j\emptyset_1}$) and y-component ($E_{yo}(x,y)e^{j\emptyset_2}$)

$$\vec{E}(x,y) = \vec{x}E_{xo}(x,y)e^{j\emptyset_1} + \vec{y}E_{yo}(x,y)e^{j\emptyset_2} \quad (2.1)$$

In order to generate a CP pattern, the following condition must be satisfied $\overrightarrow{|E_{xo}|} = \overrightarrow{|E_{yo}|}$ and $\Delta\emptyset = \emptyset_1 - \emptyset_2 = \pm(\frac{1}{2} + 2n)\pi$ where n=0,1,2, … positive for right hand circular polarization (RHCP) and negative for left hand circular polarization (LHCP).

Axial ratio (AR), which is the ratio of the major axis to the minor axis in the polarization ellipse as shown in Figure 2.4, is a figure of merit to evaluate the polarization purity and it can be calculated by equation (2.2):

$$AR = \frac{Major\ axis}{Minor\ axis} = \frac{OA}{OB} \quad (2.2)$$

where

$$OA = \left[\frac{1}{2}\left\{E_{xo}^2 + E_{yo}^2 + \left[E_{xo}^4 + E_{yo}^4 + 2 \times E_{xo}^2 E_{yo}^2 \cos(2\Delta\emptyset)\right]^{1/2}\right\}\right]^{1/2} \quad (2.3)$$

and

$$OB = \left[\frac{1}{2}\left\{E_{xo}^2 + E_{yo}^2 - \left[E_{xo}^4 + E_{yo}^4 + 2 \times E_{xo}^2 E_{yo}^2 \cos(2\Delta\emptyset)\right]^{1/2}\right\}\right]^{1/2} \quad (2.4)$$

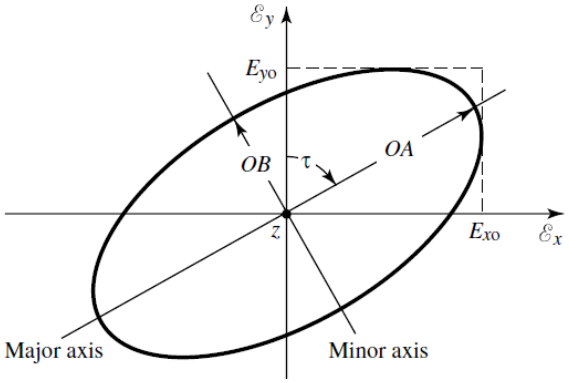

Figure 2.4: Polarization ellipse [69] © 2005 WILLEY.

Typically, if an antenna generates a radiation pattern with AR ≤3 dB, it is considered a CP antenna. Generating a wideband CP pattern is a challenging task since the antenna must be designed with two constraints that are good return loss $|S_{11}|$< -10 dB and good AR < 3dB compared with LP antenna, which usually needs to satisfy only the return loss (RL) condition. Moreover, in PAAs the problem complexity increases as the antenna should also sustain the $|S_{11}|$ and AR levels over a wide angular range. The RL problem arises from the array environment affects due to mutual coupling and surface waves; furthermore, sustaining two orthogonal modes with the same amplitude and a 90^o phase difference over a wide angular beamwidth is an extremely difficult problem due to the fact that the radiation patterns of these two orthogonal-modes are not the same. Therefore, although in one direction, usually boresight (optical axis), the antenna radiates a perfect CP, as the observation angle devatas from the perfect CP angle the radiated electric fields from these two modes become different. In addition, the CP-PAA needs to operate over a wide frequency bandwidth with good polarization purity, wide elevation angular beamwidth, and over the entire azimuthal angular range [32 and 70-72] As a result, designing a wide band CP PAA for wide scanning angle is highly complex and challenging problem, and there are very few works with very limited capabilities, which have been

reported in the literature. Single-fed CP-PAAs are relatively simple, but they exhibit very limited operating frequency bandwidth and scanning range [32, 70-73].

2.3.3 Phased-array concept

A PAA is a multi-antenna system in which the radiation pattern can be shaped to have a maximum in a particular or certain number of desired direction and much less radiation in undesired directions. The direction of phased array maximum radiation can be electronically steered, obviating the need for any mechanical rotation. PAAs with RF beam-forming commonly consist of four building blocks: antenna elements, passive feed circuit, active or passive beam-control devices including amplitude and phase shifters, beam-forming control system incorporating digital processors. They can be classified into two types: active and passive phased arrays as shown in Figure 2.5. As can be seen in the figure, an APAA allows full control of the aperture field (phase and amplitude) since each antenna element excitation is controlled by variable gain power amplifier and phase shifter on the transmitter (Tx) side, and a low noise amplifier with gain control and phase shifter on the receiver (Rx) side. However, this configuration is complex, expensive, large, and power hungry due to the large number of active components. Furthermore, separate Tx and Rx apertures are a must for wide scanning applications. A passive PAA can overcome these drawbacks to a significant extent if a high-performance passive phase shifter and feeding network can be developed. Moreover, it allows to the possibility of sharing the antenna and phase shifter between the Tx and Rx sides and leads to a more compact and low-cost system realization, a highly desirable feature for small platforms such as airplanes and vehicles [74-75].

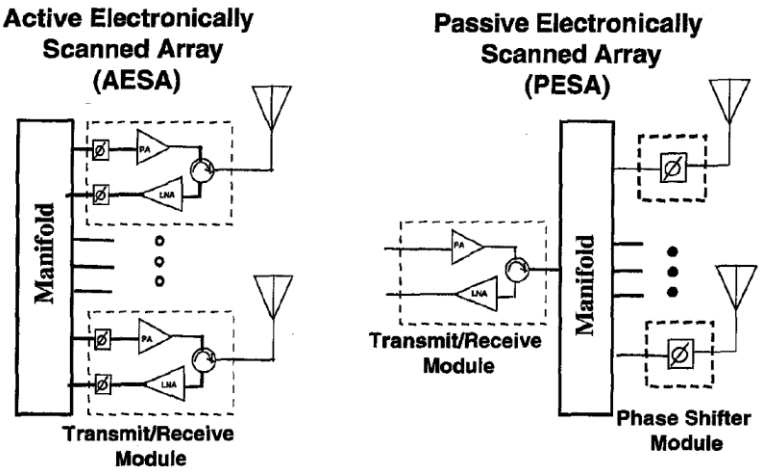

Figure 2.5: Active and passive PAA structures [75] © 1999 IEEE.

Figure 2.6 shows N radiating antenna elements with different orientation and radiation pattern/polarization arbitrarily located in the space. Each antenna element is excited by a complex number (e.g., w_i). Assume that the complex vector pattern of the antenna element number *i* with a unity excitation amplitude to be $\vec{f}_i(\theta,\phi)$. The complex vector pattern $\vec{f}_i(\theta,\phi)$ determines the radiation pattern and polarization of the *i*th element in the far zone. The electric field, $\vec{E}_0(\vec{r})$ of the element number "0", which can be referred to as the reference element, located at the origin, evaluated at a point $\vec{r}$ in the far-field can be found by equation (2.5) [76].

$$\vec{E}_0(\vec{r}) = \vec{f}_0(\theta,\phi)\frac{\exp(-jk_0 r)}{4\pi r} \qquad (2.5)$$

where $k_o = \frac{2\pi}{\lambda}$, denotes the wave constant. The distance from the *i*th antenna element, located at $\vec{r}_i$, to the desired far-field point (*P*), i.e. $\vec{r}_i$, is given by

$$\left|\vec{r} - \vec{r}_i\right| \approx r - \hat{r}\cdot\vec{r}'_i \qquad \text{[Paraxial approximation]} \qquad (2.6)$$

where $\hat{r}$ is the unit vector along $\vec{r}$. Therefore, the far field from the *i*th element can be approximated as:

$$\vec{E}_i(\vec{r}) \approx \vec{f}_i(\theta,\phi)\frac{\exp(-jk_0 r)\exp(jk_0\hat{r}\cdot\vec{r}_i)}{4\pi\left|r - \hat{r}\cdot\vec{r}_i\right|} \approx \vec{f}_i(\theta,\phi)\frac{\exp(-jk_0 r)\exp(jk_0\hat{r}\cdot\vec{r}_i)}{4\pi r}$$

Where in the far-field region, where $r >> \left|\vec{r}_i\right|$, the magnitude of $\left|\vec{r} - \vec{r}_i\right|$ in the denominator of spherical wave factor can be safely replaced by the length of r. Therefore, based on Superposition Principle the total [76] the total electric field, $\vec{E}(\vec{r})$, radiated from an ensemble of dissimilar antenna elements with different orientation is the vector sum of the electric fields radiated by individual antenna elements, and is given by:

$$\vec{E}(\vec{r}) = \frac{\exp(-jk_0 r)}{4\pi r}\sum_{i=1}^{N} w_i\,\vec{f}_i(\theta,\phi)\exp(jk_0\hat{r}\cdot\vec{r}_i) \quad (2.7)$$

This is a generalized expression for the far-field from an ensemble of arbitrary antenna elements. If the array is made of identical antenna elements, which are also *identically oriented*, which means that $\vec{f}_i(\theta,\phi) = \vec{f}(\theta,\phi); i = 0,1,...,N$, then the expression (2.7) reduces to a simpler and more common array factor equation:

$$\vec{E}(\vec{r}) = \left[\vec{f}(\theta,\phi)\frac{\exp(-jk_0 r)}{4\pi r}\right]\left[\sum_{i=1}^{N} w_i\exp(jk_0\hat{r}\cdot\vec{r}_i)\right] \quad (2.8)$$

Equation (2.8), known as the principle of pattern multiplication, consists of a product of two terms: the element pattern given in (2.5) and a summation called array factor (AF), which equals to

$$AF(\theta, \emptyset) = \sum_{i=1}^{N} w_i e^{jk_o \hat{r}.r_i} \qquad (2.9)$$

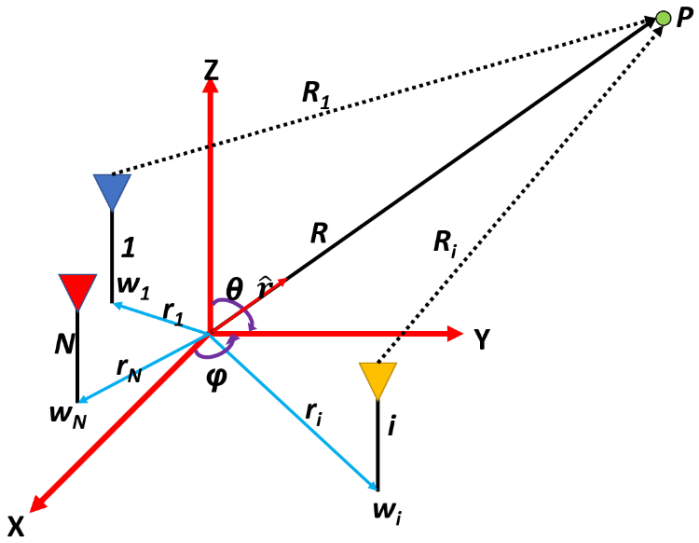

Figure 2.6: Array antenna concept [132].

AF is a function of the array geometry and the elements excitation. As can been seen from equation (2.9) the radiated beam of the antenna array can be steered to any point by changing the excitation phases. This property is known as electronically scanning or electronic beam-steering, and such systems are known as phased-array antennas PAAs. Phase shifters or delay lines are used to adjust the excitation phase of each antenna element in order to steer the array's beam towards the desired direction.

2.3.4 Reflectarray antenna (RAA)

A RAA inherits the advantages of a reflector antenna as a high-gain aperture system. It may require only a simple feed placed at a distance from the RAA to excite the aperture surface with the required amplitude and phase distribution; thereby, eliminating the complex and lossy feed circuit required by a conventional antenna array. Moreover, the feed source can be designed to provide the proper excitation distribution of the RAA surface, so the RAA can radiate either a shaped beam or a multi-beam pattern to prescribed directions simultaneously. On the other hand, similar to the antenna array concept, the RAA aperture consists of multiple small antenna elements in a planar or a conformal

configuration and is both lightweight and low profile compared to bulky reflector antennas. Different mechanisms can be used to adjust the spatial phase (the phase of incident wave emitted from the feed structure at the location of each individual surface element) so that a collimated beam can be re-radiated from the RAA aperture. Such mechanisms are classified mainly into two categories, namely fixed and steerable beams [7 and 77-81].

Figure 2.7 illustrates a general steerable RAA, whose radiation characteristics are analyzed below. Let us assume that the radiation beam is steered to an angle of (ϕ_s, θ_s). A steerable RAA consists of a tunable phase-surface that is illuminated by a feed set at an appropriate distance. The phase-surface is constructed with an array of small antenna elements. The elements are excited by the electromagnetic fields emanating from the feed and then, by complex-weighting the induced signals, the re-radiated signals constructively added in the desired direction. In this structure, a steerable RAA has a general aperture shape represented by a contour which can be square, rectangular, circular, elliptical, or a curved (defined as a function of x and y). The feed has an arbitrary polarization and location and its main beam direction is focused toward a point on the aperture defined by S [82].

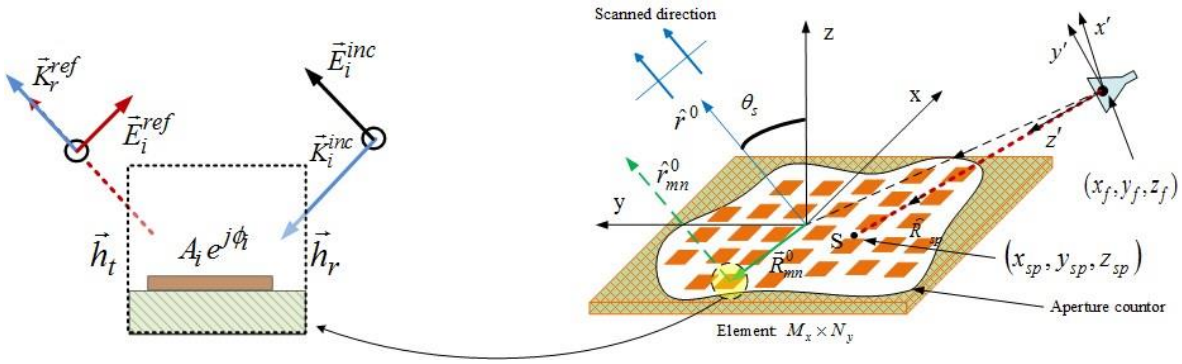

Figure 2.7: Configuration of general steerable RAA and its re-radiation mechanism [82] © 2016 IEEE.

2.4 Literature review

2.4.1 Active phased-array antenna

A demonstrated Ka-band modular 8×8 array element realized using low temperature cofired ceramic (LTCC) technology is briefly described in this subsection. IMST, in cooperation with the Technical University of Hamburg, DLR and Astrium, began to develop digitally

beam-forming Rx/Tx frontend systems in 2001. They have demonstrated a number of versions so far; the first three prototypes being designed under the SANTANA project. Their most recent product has been successfully measured [83], showing an electrically-controlled scanning response up to 60˚. This antenna system is an APAA with digitally beam-forming architecture as demonstrated in Figure 2.8.

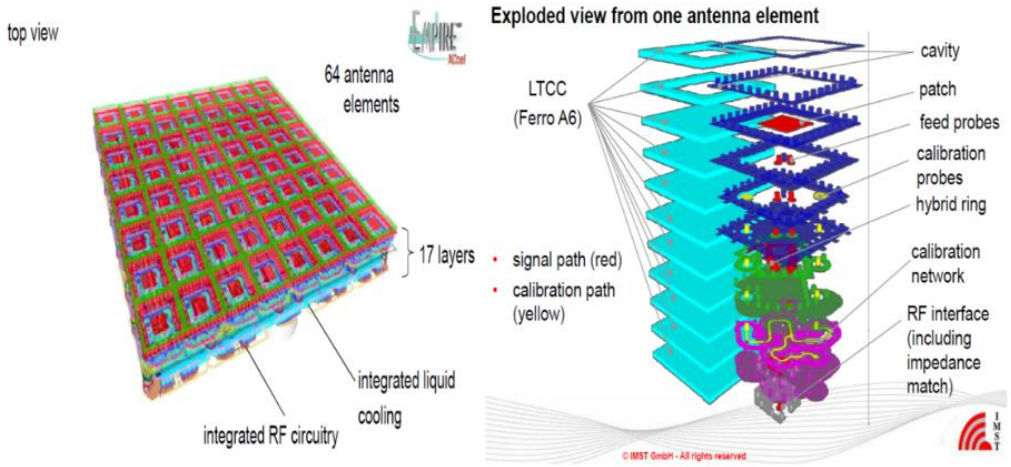

Figure 2.8: Development flow of a Tx 8×8 SANTANA RF-module (LTCC) [83] © 2013 IEEE.

The structure is a very complex frontend module consisting of 17 layers which include antenna elements, hybrid feeding structure, calibration network, active RF circuits, local oscillator (LO) distribution network, IF feeding network power, DC supply, and liquid cooling system making the large-scale fabrication and implementation of such system extremely difficult and costly.

2.4.2 Passive phased-array antennas

A wideband passive PAA can offer an attractive low-cost alternative for a wide range of emerging mm-W communication systems [24, and 84-90]. Such antenna systems are made of passive components (antennas, phase shifters, and passive feeding networks), as shown in Figure 2.9, to reduce the power consumption, cost, and complexity of the system. Furthermore, a single passive PAA made of reciprocal components can be utilized as both transmitter and receiver. In order to build such a system, a high-performance antenna and phase shifter must be developed and integrated. The antenna element should be simple and have a wide operating frequency band. Moreover, it would be required to demonstrate high cross-polarization discrimination over a wide angular beamwidth to sustain a high-quality data link and avoid undesired interferences. In addition, the phase shifter must

have low IL variation over the operating frequency range to eliminate the necessity for costly VGAs. The phase shifter needs to provide a continuous phase shift of 360^{o}, so the beam can be steered to any direction in space precisely and quickly.

A wideband phase shifter that uses a relatively low dielectric tapered slab to perturb the propagating electromagnetic wave in a TL is reported in [24 and 84-90]. This phase shifter was incorporated into a linear antenna array to develop a wideband passive PAA. A piezoelectric transducer (PET) was used to control this phase shifter. However, the passive PAAs presented in [24 and 84-90] have several drawbacks and limitations. A large dielectric slab ($>\lambda_o$) is required to realize a 360^{o} phase shift. Therefore, the inter-element spacing will be $>>0.5\lambda_o$ in one plane of the two-dimensional (2-D) PAA, which leads to the appearance of a grating lobe when the beam is steered in that particular plane. Furthermore, this method is limited to only linear (1-D) phase-array configurations. The PET requires a high voltage to operate, necessitating a high voltage power supply be a component of a large PAA. The PETs used in these structures are bulky. Furthermore, no packaging structure has been presented to date that protects such systems against environmental effects. In references [24 and 84-90], since a single tapered dielectric slab has been used to control the phase state of the antenna elements, the beam of these phased arrays can only be steered in one direction off-boresight. This is the main drawback of such structures. To steer the beam in two directions, a second complementary dielectric slab must be incorporated adding further complexity and increasing the size of the phased array. This type of PAA is prone to large pointing errors due to warpage of the PCB. Any local surface defect can affect the progressive phase state of that specific antenna element and there is no way to correct this phase error. This lack of independence can lead to serious difficulties in phase calibration. It should be noted that none of the reported configurations have been presented in a low-profile and packaged form. Moreover, to the best of the author's knowledge, a CP passive PAA has not been presented in the literature employing this beam-scanning technique.

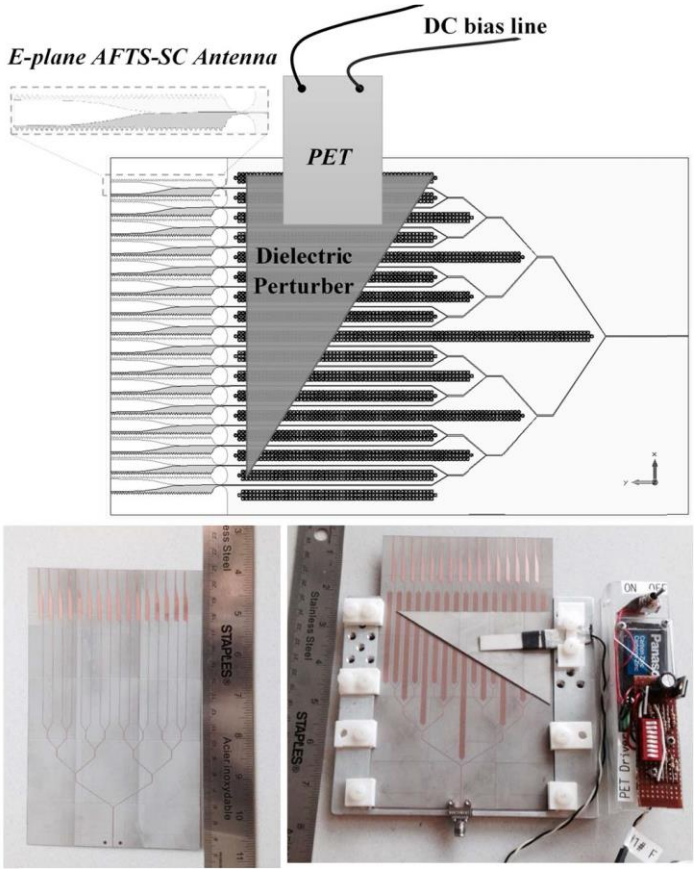

Figure 2.9: Typical passive phased array based on TL loading with dielectric slab [24] © 2017 IEEE.

2.4.3 Reconfigurable reflectarray antennas

A steerable RA is in high demand for a vast number of commercial systems such as SATCOM, wireless communication (e.g., 5G for base stations), space systems, sensors, and radar. In particular, the use of emerging mm-W frequencies appears to offer an attractive solution for an increasing number of ultra-high data rate communication and sensing systems. Given this backdrop, a simple and reconfigurable RAA UC is the core element necessary for the realization of such systems [79-81]. A number of reconfigurable RAA elements have been presented in the literature [91-93] that aim to provide a large tunable reflection phase. An RAA element operating at 5.4 GHz has been presented in [91] by loading two square-shaped rings with tunable varactor diodes. The reported element exhibits a tunable reflection phase range of 380^{o} and a maximum reflection loss of 3.5 dB; however, it has a limited frequency bandwidth of 2.4% and its reflection loss is relatively high even at such a low operating frequency. A tunable high impedance surface has been developed in [92] to realize a

reconfigurable RAA element at 60 GHz. This element not only exhibits a very narrow frequency bandwidth but also it achieves a reflection phase of only 200^{o}, while its reflection loss is 12 dB. Similarly, a tunable BST material has been used in [93] to capacitively load a patch antenna as a building element to develop a reconfigurable reflectarray which operates in the Ka-band. The above element suffers from a very high reflection loss, in the order of 16 dB. Furthermore, the reflection loss varies rapidly with the biasing voltage and leads to an increase of the SLL of the reflectarray, as may be seen in [94].

2.4.4 Phase shifter

The phase shifter is one of the most critical elements in a phased array system. It is the bottleneck in terms of reducing the cost and complexity of such systems and significantly affects the performance of the overall system. There are many factors that are used to evaluate a phase shifter. Phase shift variation range, IL, IL variation, size, cost, speed, integration, bandwidth, passivity, and high-power handling are the most crucial characteristics that should be considered in the choice of phase shifter [75 and 95]. Phase shifters are typically divided into analog and digital types. Despite their main attractive feature, namely their accurately predictable phase shift, digital phase shifters are a suitable choice only for applications that require discrete phase shift and for which power consumption is not a concern.

The most desirable characteristics of a phase shifter, particularly for large phased array applications include low IL, low IL variation, wide operating frequency band, compact size, and reciprocity. Such phase shifters are key elements for realizing a low cost, low power consumption, and low complexity PAA. In particular, for a mm-W phased array system with ($0.5\lambda_o$ x $0.5\lambda_o$) cell size, it is quite important that the phase shifter has a small enough footprint that it can be placed directly underneath the antenna element and share the power amplifiers and low noise amplifiers among a group of antennas. Furthermore, these characteristics enable antennas and phase shifters to be shared between the Tx and Rx, thereby greatly reducing the cost, power consumption, complexity, and size of the PAA [75 and 96]. Therefore, a low cost, compact, and integrated phase shifter with low IL and minimal IL variation is essential for high performance telecommunication phased array systems.

Micro-electro mechanical systems (MEMS)-based phase shifters are mainly of the digital type. Analog MEMS phase shifters are large and show a low FOM (figure of merit) [96-99]. Passive type MMIC phase shifters suffer from high IL, limited resolution and limited operating bandwidths [100-104]. An alternative approach is to use tunable dielectric-based phase shifters such as ferroelectrics

[105-108], and liquid crystal (LC) [109-111]. These materials have dielectric properties that change when exposed to an electric field, causing a phase change. All the aforementioned phase shifters can potentially be low cost and compatible with planar circuits. However, they show low FOM performance (< 50◦/dB) especially at the frequency bands of interest. Additionally, ferroelectric-based phase shifters show a poor return loss over the operating frequency bandwidth [108], and phase shifters based on common LC materials suffer from slow response to the applied electric field [109]. Adding a perturber to the top of a planar TL and using mechanical actuators to change the phase shift [95 and 112-115] is the basis of another type of continuous phase shifter. Among these, elastomer-based phase shifters require a very high biasing voltage [112] and the device occupies a large area. A metallic perturber, used in [95], generates a large phase shift variation and reduces the size of the device. However, the IL rapidly increases with frequency. Furthermore, the measured IL variation is substantially high. In [113-114], a low dielectric slab is used to tune the phase of a planar TL, but the length of the device should be sufficiently large to achieve the required phase shift. Also, the IL increases with frequency. Similarly, phase shifters using a magneto-dielectric disturber suffer from large size and high IL at high frequencies [115].

As a highly promising response to these challenges, a novel low loss phase shifter based on very high dielectric constant materials [e.g., barium lanthanide tetratitanates (BLT) ceramics] was reported in [116-117] (Figure 2.10). Based on this new concept, low IL and compact phase shifters with minimal IL variation have been developed in CIARS. The phase shifter consists of a coplanar waveguide (CPW) on a high resistivity silicon (HRS) substrate loaded by a BLT rectangular slab. By changing the gap between the CPW and BLT, the propagation constant of the CPW mode is perturbed causing a substantial change in phase. Among the proposed designs [116], the CPW-serpentine line loaded with BLT slab is more compact and offers higher phase shift (~369˚ at 30 GHz) than other approaches. However, it suffers from impedance mismatches that limit the operating frequency bandwidth, especially when it is loaded by a BLT slab with a high dielectric constant (ε_r; > 100). To solve this problem, the BLT slab is tapered from both ends to minimize reflections [117]. Although, this technique is successful in enhancing the operating bandwidth (more than 20 GHz), it degrades the phase shifter's dynamic range and increases the complexity of the fabrication process. Moreover, due to the use of nonstandard fabrication methods the proposed designs in [116-117] might not be suitable for high volume low cost phased array systems.

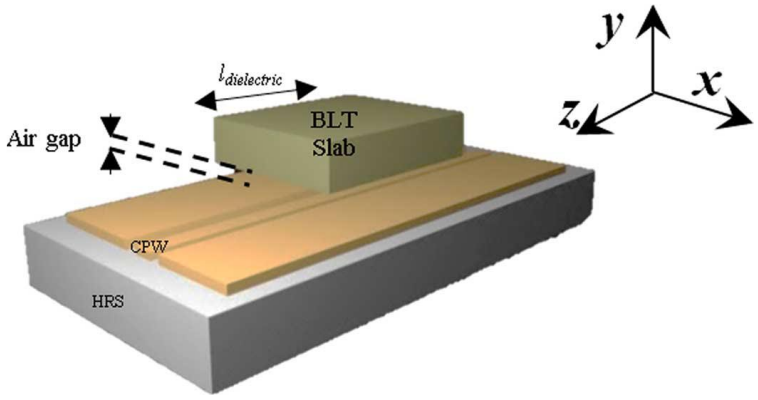

Figure 2.10: CIARS BLT-based phase shifting concept [116] © 2014 IEEE.

2.5 Conclusion

This investigation shows that the design and realization of a CP Ka-band antenna system for SOTM communications has received significant attention during recent years. Specifically, to the best of author's knowledge, a low profile and fully electronically steered beam antenna that fulfills the standard FCC mask requirement and frequency bandwidth over a wide angular scan range has not been demonstrated to date by any company or research team. Accordingly, there is a huge demand for a high performance, low cost, and simple CP PAA and steerable RAA with electronically-steerable beam functionality for SOTM operating at Ka-band frequencies. In the following chapters, the results of investigation of a number of enabling technologies for a new modular architecture for high performance but affordable phased-array systems for emerging KA-band SOTM applications will be presented. Although the proposed concepts are general, as a particular example, a number of new designs for high performance antenna elements with wide angular beamwidth capabilities and wide operating bandwidth as suitable antenna elements for Ka-band SATCOM system will be proposed, analyzed, and tested. Then the proposed antenna elements will be utilized to construct working prototype antenna sub-array modules and will be integrated with CIAR novel phase-shifter technology and multi-layer active array platform for CP Ka-band steerable antenna arrays for SOTM applications.

Chapter 3
Ka-band Single-fed CP APAA for Wide Beam-steering

3.1 Introduction

The objective of this chapter is to develop and analyze a mm-W planar antenna element that is suitable for large-scale wide beam-steering PAA systems. The proposed antenna element was developed based on an ACMPA fed by a grounded coplanar waveguide (GCPW) transmission line (TL) and is intended to be directly integrated with different beam-steering networks. The antenna element was proposed as a candidate to build a proof-of-concept prototype Ka-band CP steerable PAA for SOTM applications. The single-fed CP antenna is comprised of a multimode slot resonator (MSR) to excite an elliptical microstrip patch (EMP) with a CP field. A simple design procedure was developed for the proposed antenna concept and a full-wave numerical simulation tool based on finite elements method (FEM) from ANSYS corporation was used to validate the proposed antenna. The antenna element was then utilized to construct a 4×4 CP fixed-beam antenna array module to validate the proposed antenna. The modularity concept was studied by implementing a 16×16 antenna array based on the 4×4 module as a proof-of-concept of a low-cost, simple, and modular Ka-band CP antenna array.

A 4×16 CP-APAA was designed and fabricated using a three-metal-layer low-cost PCB technology as a proof-of-concept for the proposed antenna. The developed antenna array was used in CIARS active 4×16 active array platform containing eight-channel MMIC to control both the amplitude and phase of each individual antenna element in a 64-element array. The proposed CP-APAA was tested over a wide scanning range from 0^o to $\pm 40^o$ in the elevation. Furthermore, the SLL of the radiation pattern was successfully controlled by tapering the power level over the antenna aperture. It was demonstrated that the developed array can generate multiple beams simultaneously at different scanning angles with arbitrary radiated power levels.

3.2 Proposed single-fed aperture-coupled CP antenna I

3.2.1 Proposed concept

A CP PAA with a wide scanning angle requires an antenna element with a wide angular AR< 3 dB beam-width. In addition, the inter-element separation must be $\leq \lambda_o/2$ to avoid the grating lobe effect. A novel CP antenna element based on an ACMPA was proposed for Ka-band applications. The

proposed structure employs a new slot resonator to degenerate two orthogonal modes; these modes are then coupled to an elliptical shaped microstrip patch to radiate a CP pattern. In order to directly integrate the proposed antenna with different beam-forming circuits, a GCPW TL was utilized as a feed line. The first prototype of the proposed antenna concept was developed on 4000 series RT/duriod material from ROGERS corporation, a low-cost material and preferred by fabrication facilities.

A proposed new aperture slot is the core component, its shape initially developed by modifying an annular square ring resonator (ASRR). A single mode ASRR can be designed to resonate at a frequency f_n based on equation (4.1) [118].

$$f_n = \frac{nc}{4(L_1 - s)\sqrt{\varepsilon_{eff}}} \ldots \quad n = 1,2,3 \ldots \qquad (3.1)$$

Where c is the speed of light in mm/s, L_1 is the length of the ASRR arms in mm, S is width of the ASRR arms in mm, and ε_{eff} is the effective permittivity of the dielectric substrate. **Figure 3.1** shows the configuration of the ASRR. It was developed on a substrate of RO3003 with ε_r=3. Using the equation (3.1), the arm's length and width were calculated for the resonator to operate at 30 GHz. The ASRR was designed and simulated in full-wave simulator to validate the obtained dimensions based on weak excitation [119]. **Figure 3.2**a shows the RL of the simulated ASRR; it resonates at 30.15 GHz. The small shift in frequency is attributed to the effect of the feed line and the resonance can be tuned easily. The ASRR generates a single mode Y-polarized standing wave as shown in **Figure 3.2**b.

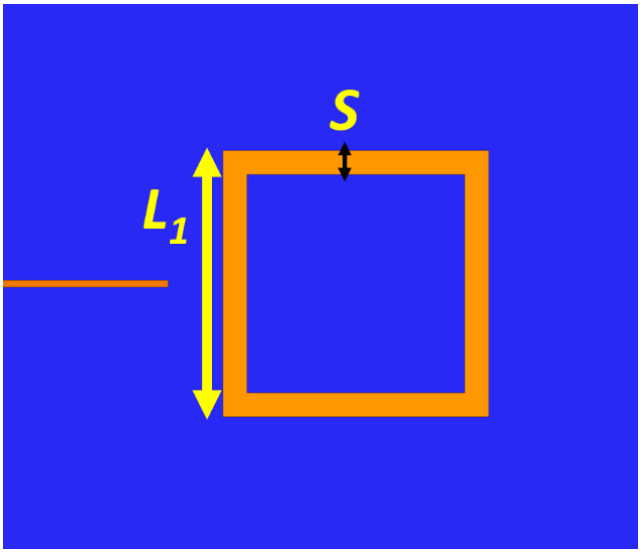

Figure 3.1: ASRR configuration.

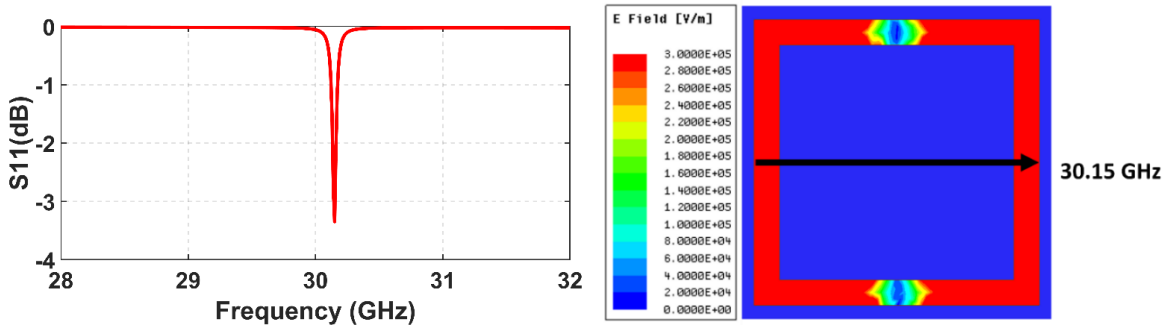

(a) (b)

Figure 3.2: Resonance response of ASRR: (a) S_{11} (dB) and (b) the average electrical field (V/m).

Dual orthogonal modes can be degenerated if an asymmetry is imposed on the ASRR. This can be achieved by utilizing a perturbation mechanism [118-119]. By modifying one of the corners of the ASRR, dual-mode orthogonal resonances can be realized with resonance frequencies of $f^e < f_n$, and $f^o > f_n$ respectively, resulting in a dual-mode ASRR (DM-ASRR). By optimizing the shape and size of this perturber, the amplitudes of the two resonances (f^e, *and* f^o) can be adjusted to be equal at f_o and the phase difference to equal 90°. This is the condition under which a CP pattern is generated with an AR of 0 dB in the boresight [118]; however, the frequency bandwidth of such a structure is usually narrow (< 2.5%) [122]. In this research, the perturbation was achieved by bending one of the corners of the ASRR so that dual orthogonal modes are realized as shown in **Figure 3.3**a. Full-wave simulation was used to optimize the lengths of the perturber's arms to generate a CP pattern at 30 GHz. The first resonance occurs at 29.55 GHz and the second resonance appears at 30.56 GHz, as shown in **Figure 3.3**b.

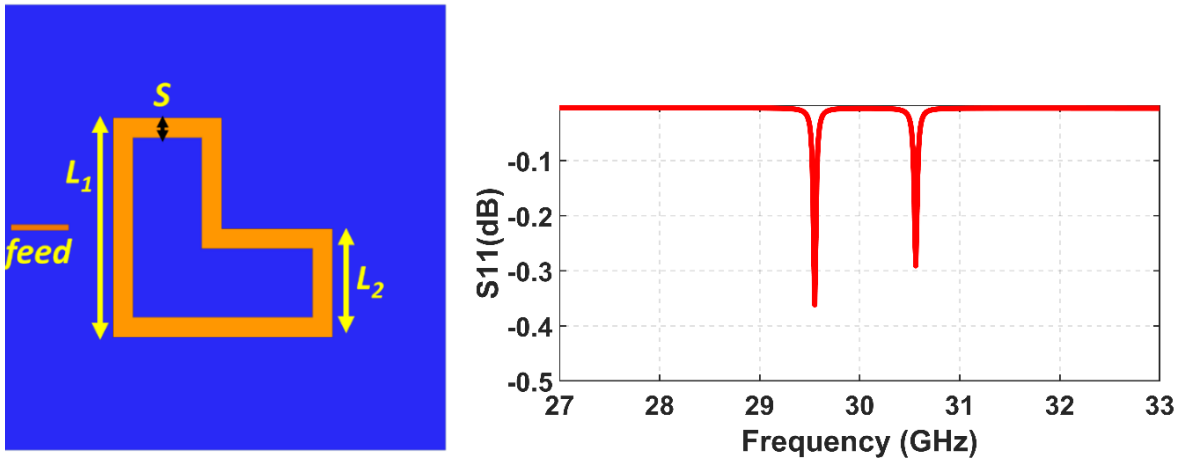

(a) (b)

Figure 3.3: (a) DM-ASRR configuration, (b) S_{11} (dB).

For this specific structure, the first resonance (f^e) appears at φ=+45° (lower than f_n as the length> L_1; shown in **Figure 3.4**a black arrow), and the second resonance (f^o) appears at φ=-45° (higher than f_n as the length < L_1; shown in **Figure 3.4**b black arrow). As a result, with this configuration a CP wave can be generated at 30.05 GHz.

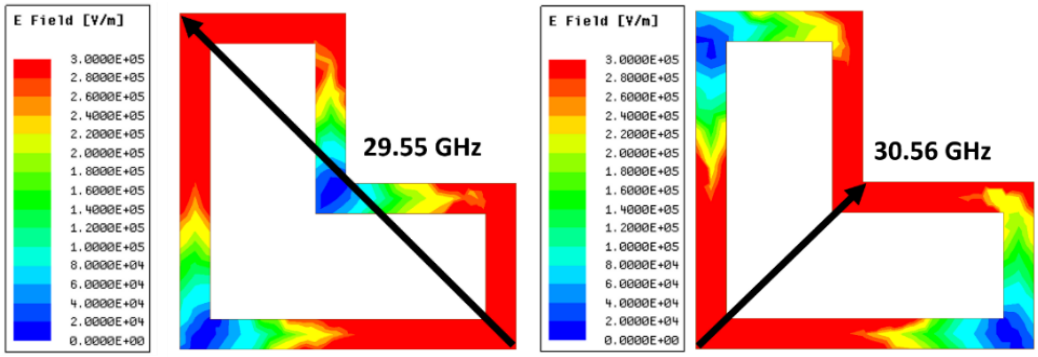

(a) (b)

Figure 3.4: Average electrical field (V/m) response of DM-ASRR: (a) at f^e, (b) at f^o.

A slot-type DM-ASRR was developed by utilizing the electromagnetic duality theorem. The resulting slot was used to modify the aperture slot shape of an ACMPA as a method to excite the microstrip patch with two orthogonal modes with the same amplitude and a 90° phase difference at the center of the operating frequency bandwidth. The shape of the microstrip patch was chosen to have asymmetrical length and width shapes (e.g., rectangular, elliptical, and diamond), so it could be coupled with the degenerated modes of the slot ASRR. As a result, the proposed antenna consists of

two main radiators (a slot-type DM-ASRR as a driven element, and an elliptical patch as a parasitic radiator), both of which can be used to generate a CP pattern [118, and 120]. The advantages of the proposed concept include the widening of the AR frequency bandwidth of the ASRR to > 5% through employing a stacked radiators concept [121] and improving the AR angular beam-width of the ACMPA to > 100^o in elevation (θ).

3.2.2 Design of the proposed Ka-band CP antenna I

The antenna structure consists of three metal layers (M1, M2, and M3) as shown in **Figure 3.5**a. An EMP was etched on the top substrate with a major axis of $2R_1$ and a minor axis of $2R_2$, values chosen to achieve a wide impedance bandwidth. The middle metal layer forms the ground plane and contains the proposed slot-type DM-ASRR. The slot ring has six arms with lengths labeled (L_{s1}-L_{s6}) and a slot gap of *S*. With this slot configuration, two orthogonal modes can be generated over the slot gap. The length of the arms $L_{s1} = L_{s2}$ were chosen to ensure the square ring slot has an electrical length of nλ at the resonance frequency, and the arms L_{s3}, L_{s4}, L_{s5}, and L_{s6} were chosen to excite two orthogonal modes with a 90^o phase difference. The slot is coupled to a GCPW line that was etched at the backside of the bottom substrate through a series transverse slot. The ground size of the antenna element is 5×5mm^2(0.5λ_o×0.5λ_o) at 30 GHz. RO4003 substrate (ε_r=3.55, tanδ=0.0027) was used to design the radiating patch and RO4360G2 substrate (ε_r=6.15, tanδ=0.0038) was used to design the GCPW feed line. In addition, RO4450F substrate (ε_r=3.52, tanδ=0.004) was used to bond the two substrates. The DM-ASRR was designed based on design equations (3.2) and (3.3).

$$L_{s1} = L_{s2} = 0.5\lambda_{g1} \qquad (3.2)$$

And

$$L_{s3} = L_{s4} = L_{s5} = L_{s6} = 0.25\lambda_{g1} \qquad (3.3)$$

Where λ_{g1} is the guided wavelength of the DM-ASRR. The GCPW line width W_f and gap width S_f are calculated for 50 Ω characteristic impedance and the transverse slot has a length of 1.525 mm. An electrical vias wall was employed between the grounds of the GCPW line and the DM-ASRR to suppress the spurious radiation of the feeding network, surface waves, and to reduce the mutual coupling between the adjacent antenna elements. Mutual coupling is one of the major problems in steerable antenna arrays, especially for wide angle beam-steering where the antenna impedance usually deteriorates significantly [44, and 50].

The major and minor axes of the EMP were optimized for better radiation and coupling. The major axis ($2R_1$) and minor axis ($2R_2$) can initially be set based on the closed-form equations derived in

[115]. The elliptical patch has two dominant resonance modes: $TM_{11}^{o,e}$ odd and even. The resonance frequency of these modes can be calculated from equations (3.4)- (3.8) [122].

$$f_{11}^{o,e} = \frac{15}{\pi e R_{1eff}} \sqrt{\frac{q_{11}^{o,e}}{\varepsilon_r}} \tag{3.4}$$

Where $f_{11}^{o,e}$ are the dual resonant frequencies, R_{1eff} is the effective major radius due to fringing field, $q_{11}^{o,e}$ is the approximate zeros of Mathieu function for dominant ($TM_{11}^{o,e}$), and e is the ellipse eccentricity.

$$e = \sqrt{1 - \left(\frac{R_2}{R_1}\right)^2} \tag{3.5}$$

$$q_{11}^{o} = -0.0063e + 0.38316e^2 - 1.1351e^3 + 5.2229e^4 \tag{3.6}$$

$$q_{11}^{e} = -0.0049e + 3.7888e^2 - 0.7278e^3 + 2.314e^4 \tag{3.7}$$

$$R_{1eff} = \left[R_1 + \frac{hR_1}{0.3525\pi\varepsilon_r}\left\{ln\left(\frac{R_1}{2h}\right) + (1.41\varepsilon_r + 1.77)\cdot + \frac{h}{R_1}(0.268\varepsilon_r + 1.65)\right\}\right]^{1/2} \tag{3.8}$$

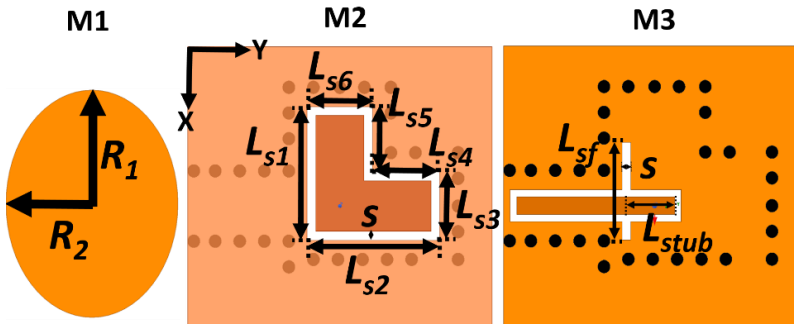

(a)

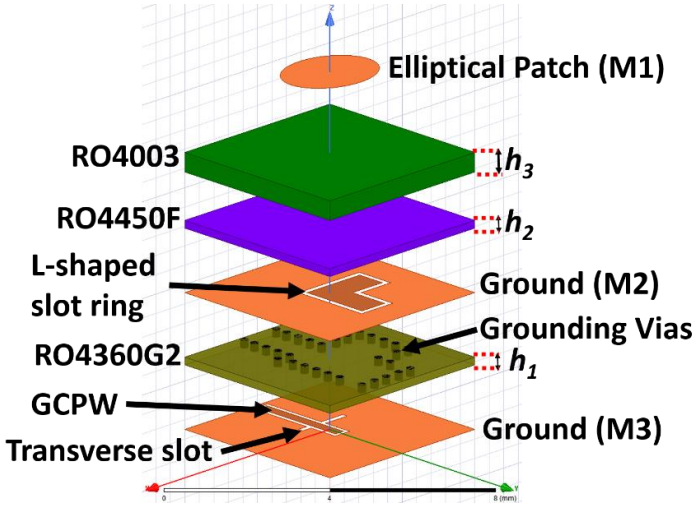

(b)

Figure 3.5: Proposed CP antenna structure: (a) metal layers, (b) 3-D exploded view.

3.2.3 Simulation results

A full-wave simulator was used to analyze and optimize the antenna parameters. An extensive parametric study was conducted on the antenna's parameters to examine their impacts on the overall antenna's performance. It was found that the slot arms L_{s3}-L_{s6}, and the eccentricity of the elliptical patch, *e*, are the most critical parameters affecting the purity of the circular polarization pattern over a wide angular beam-width. The major axis $2R_1$, the slot arms L_{s1}, L_{s2}, the feeding point, and the length of the transverse slot L_{sf} were found to be mainly responsible for the impedance bandwidth. The antenna parameters were optimized by using the HFSS optimization tool, the goal being to achieve the optimum AR and impedance matching over the operating frequency band (i.e., 29-31 GHz). The optimized parameters of the antenna are shown in **Table 3.1**. Using state-of-the-art multi-layer fabrication technology, high quality planar antennas and feed circuits can be realized with a dimensional accuracy better than 20μm. Extensive full-wave sensitivity analyses (**Figure 3.6**) were conducted on the proposed antenna with ±25 μm variation from the nominal values of some critical design parameters (e.g., R_1, R_2, L_{s1}, L_{s3}, *S*, L_{sf}, and L_{stub}). Simulation results revealed that the proposed antenna is less sensitive to parameter variation within the range of the fabrication tolerances.

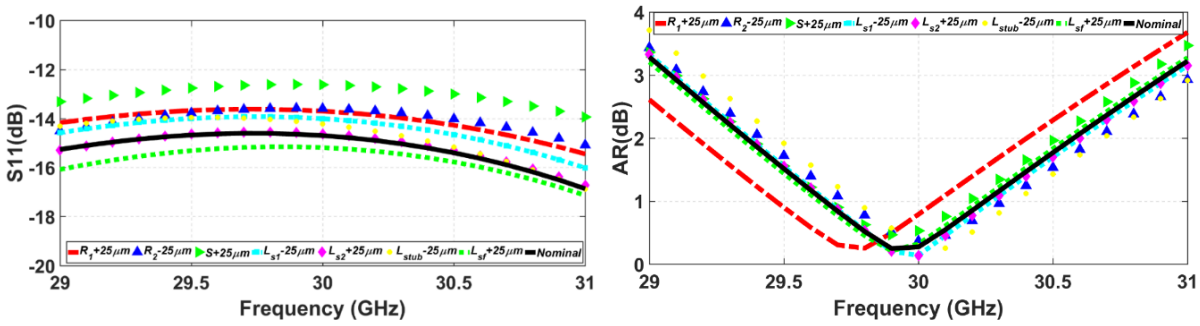

(a) (b)

Figure 3.6: Sensitivity analysis of proposed antenna element: (a) S_{11} (dB) and (b) AR (dB).

The simulation results show an impedance bandwidth (S_{11} <-10 dB) of almost 8 GHz centered at 30 GHz. The two resonances of the elliptical patch appeared at 28 GHz and 32.75 GHz, as shown in **Figure 3.7**a. The proposed antenna shows an AR< 3dB bandwidth of 1.8 GHz (6 %) centered at 30 GHz at the boresight, and an AR bandwidth of 1.3 GHz over an angular beam-width from -70° to +70° off-boresight, as shown in **Figure 3.7**b. These results demonstrate that the antenna satisfies most of the stringent Ka-band system requirements in terms of the RL, size, and AR and angular beam-widths. It has a 5 dBic gain over the operating frequency, with an almost symmetrical pattern over the azimuth angles (ϕ); moreover, it shows an X-pol discrimination better than 35 dB at 30 GHz, as shown in **Figure 3.8**.

Table 3.1: Optimized Parameters of CP Antenna (mm).

Parameter	R_1	R_2	Ls_1	Ls_2	Ls_3	Ls_4	Ls_5
Dimension	1.345	1.06	2.13	2.13	1.07	1.07	1.07
Parameter	Ls_6	S	L_{sf}	L_{stub}	h_1	h_2	h_3
Dimension	1.07	0.14	1.525	0.8	0.203	0.203	0.508

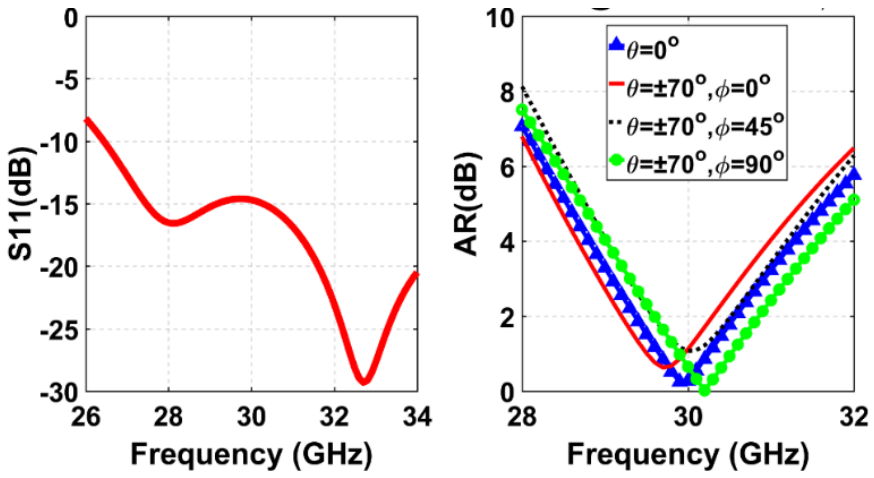

(a) (b)

Figure 3.7: Simulated RL and axial ratio: (a) S_{11} (dB), (b) AR (dB) for ϕ=0°, 45°, and 90°; and θ =0° and ±70°.

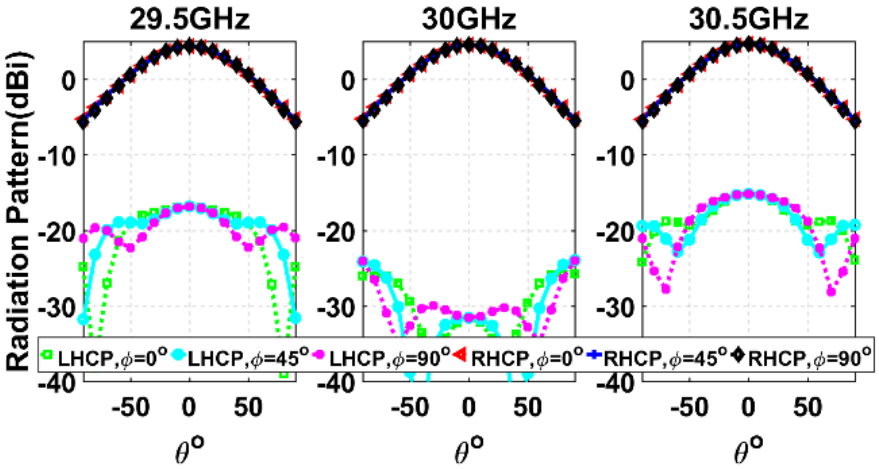

Figure 3.8: Simulated radiation patterns at 29.5, 30, and 30.5 GHz for ϕ=0°, 45°, and 90°.

The element radiation pattern azimuthal symmetry is essential for a phased-array with full 360° azimuthal scan range. The other main challenge in wide-scan-angle phased-arrays is the variation of the antenna active impedance versus scan angle, particularly in active phased-array configurations where the delivered power from the semiconductor amplifying devices strongly depends on the antenna's active impedance, as reported in [49-50]. As a result, the antenna element has to show a symmetrical CP radiation pattern with a minimal impedance variation as the scan angle varies with high X-pol discrimination over the operating frequency band. Extensive full-wave simulation and design optimization was performed to realize the aforementioned characteristics to their full extent.

All the simulations were carried out under periodic boundary conditions (PBCs) (infinite array environment) to evaluate the performance of the proposed antenna in a large array environment for different scanning angles (see **Figure 3.9**). The mutual coupling effects were fully taken into consideration. The antenna was simulated over the SOTM frequency band of 29.5-30 GHz.

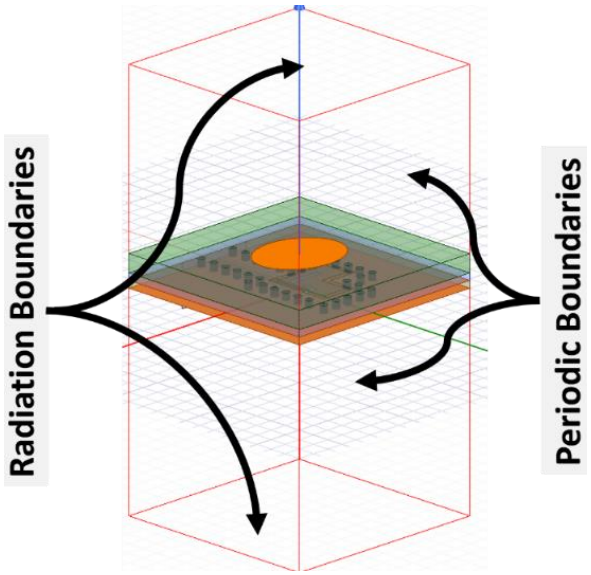

Figure 3.9: Simulation setup of antenna in infinite array boundaries.

The antenna was simulated over the scanning range 0-90º and azimuth range 0º, 45º, and 90º. The antenna showed a wide active impedance of< -10 dB in φ =0º over the scanning angle θs=0-60º, φ =45º over the scanning angle θs=~0-60º, and φ =90º over the scanning angle θs=0-50º, as shown in **Figure 3.10** (a-c) respectively.

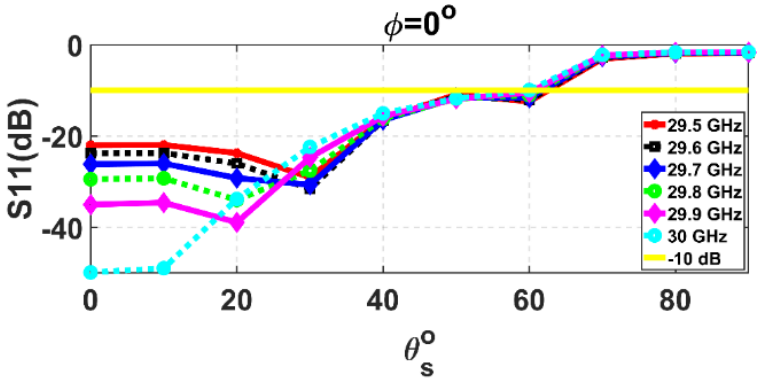

(a)

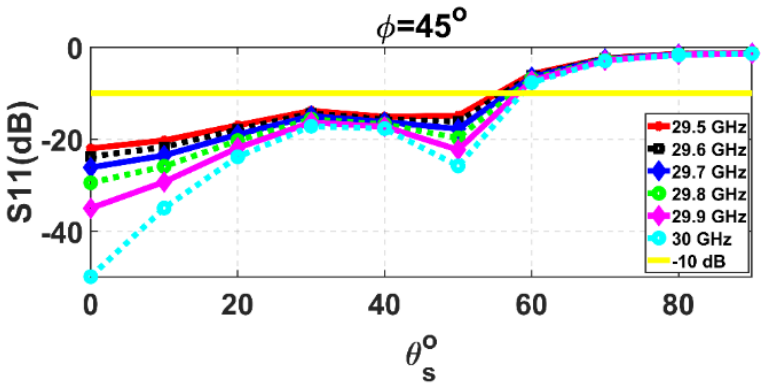

(b)

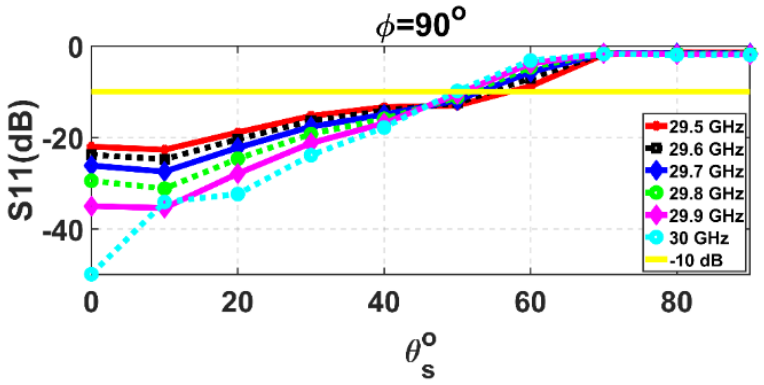

(c)

Figure 3.10: Simulated RL (S_{11}) versus scanning angle at: (a) phi=0°, (b) phi=45°, and (c) phi=90°.

The antenna shows an AR < 3 dB in the φ =0° over the scanning angle θs=0-30°, φ =45° over the scanning angle θs=0-50°, and φ =90° over the scanning angle θs=0-50°, as shown in **Figure 3.11**(a-c) respectively.

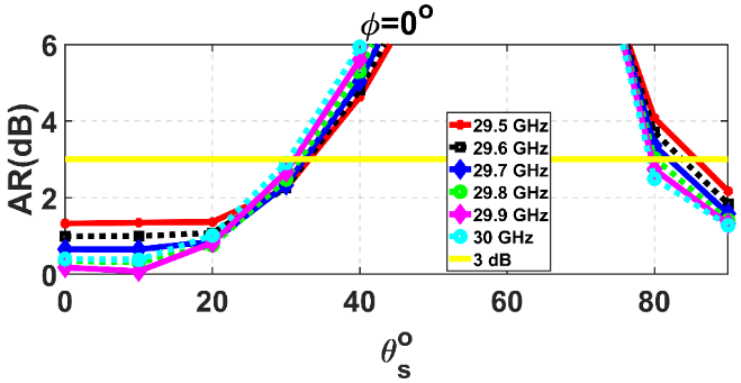

(a)

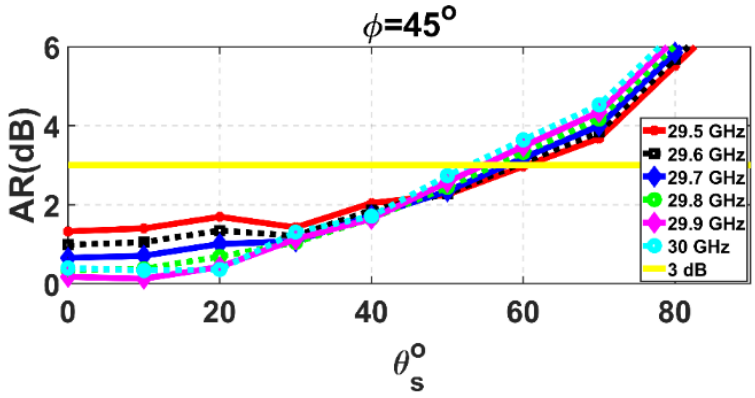

(b)

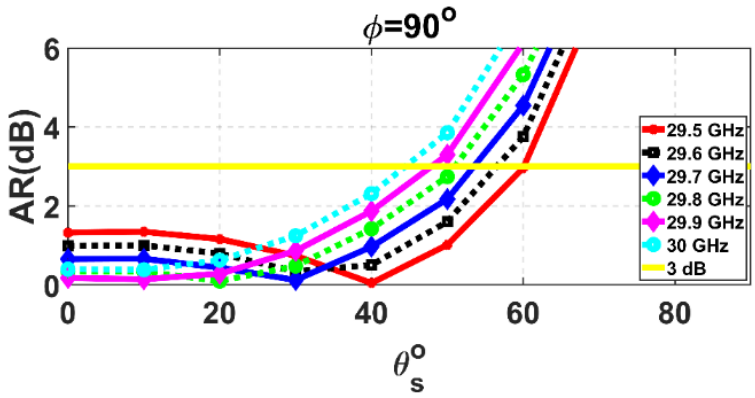

(c)

Figure 3.11: Simulated AR versus scanning angle at: (a) phi=0°, (b) phi=45°, and (c) phi=90°.

In addition, the proposed antenna realizes an RHCP radiation pattern with very high X-pol (LHCP) discrimination (>50 dB at the boresight) at 29.9 GHz, as shown in **Figure 3.12**. The simulation results show that the antenna is a good building block for low-cost large-scale mm-W CP PAA applications, such as SATCOM, as will be discussed later in Section 3.4.

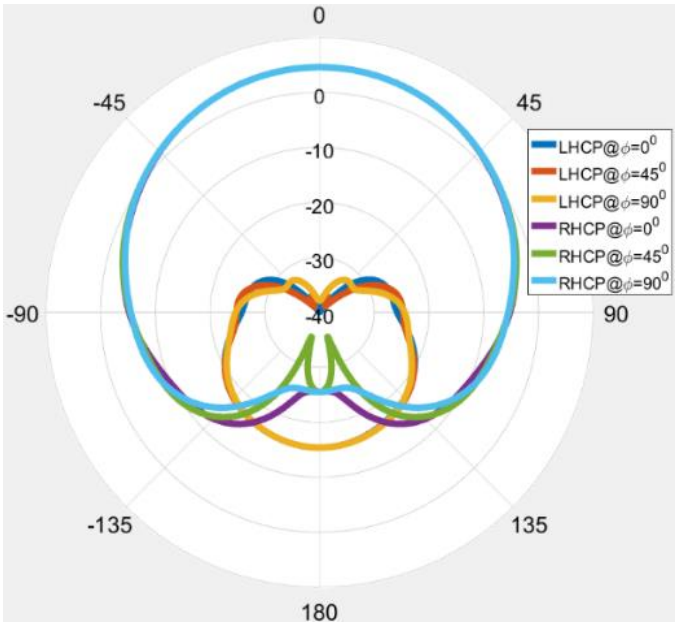

Figure 3.12: Simulated radiation pattern (dBic).

3.3 Proposed single-fed aperture-coupled CP antenna II

3.3.1 Single-fed aperture coupled CP antenna II

Utilizing a mechanism similar to that adopted in Section 3.2, the perturbed slot ASRR can be modified further with another perturber at one of the corners to excite another dual orthogonal mode centered at f_{n2} with resonance frequencies of f^{e}_{2} and f^{o}_{2}. Accordingly, a quad mode resonator can be developed to widen the CP frequency bandwidth in order to cover the entire operating frequency of the SATCOMs (27.5 GHz -30 GHz). The new quad-mode resonator is shown in **Figure 3.13**. The second orthogonal modes are excited when an open circuit gap is imposed on the DM-ASRR at -45°. By proposer optimization of the open circuit cut and the ASRR arms, the generated four resonances can be adjusted. A full-wave simulator was used to study the proposed concept. If a 0.2 mm gap cut of the DM-ASRR, four resonance are generated at 27.85 GHz, 28.4 GHz, 30.4 GHz, and 30.5 GHz, as shown in **Figure 3.14**. This concept was used with the proposed CP antenna element to increase the AR< 3 dB bandwidth.

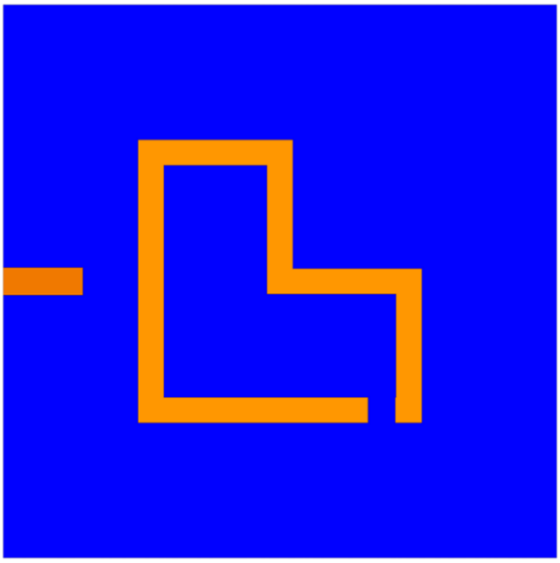

Figure 3.13: Quad mode-ASRR concept.

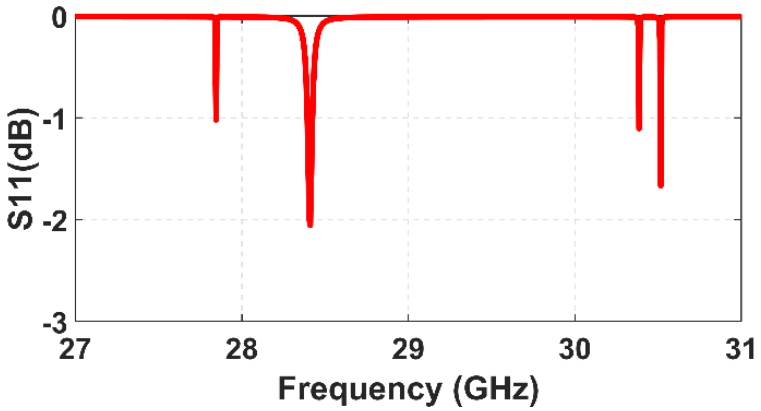

Figure 3.14: Simulated S_{11} of proposed quad mode-ASRR.

In order to generate a similar sense of CP pattern to that generated by the first two orthogonal modes, the location of the open circuit was chosen to be -45°. This method was applied on the proposed CP ACMPA to validate the concept. The new antenna is shown in **Figure 3.15**. A short circuit (width of 0.185 mm) and bending were used to modify the slot ASRR so that a quad-mode resonator could be obtained, and an elliptical cut (major radius of 0.325 mm) was used on the EMP to enhance the reflection frequency bandwidth. The resultant antenna was simulated in PBCs and optimized with full-wave simulator over the frequency bandwidth of 27-31 GHz.

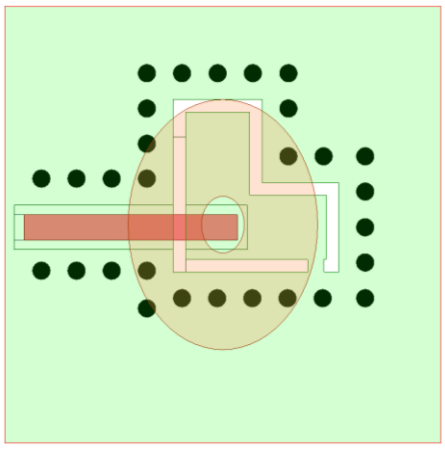

Figure 3.15: Proposed Ka-band CP antenna II

To realize high circular polarization purity, the four resonance modes were chosen to be close to each other so that the proposed structure realizes an AR< 1dB over a wide frequency band (28.6-30.3 GHz) as shown in **Figure 3.16**.

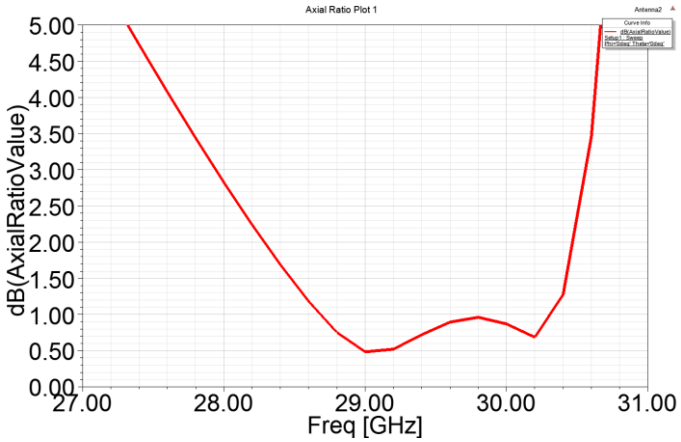

Figure 3.16: Simulated AR (dB).

The optimized antenna was simulated in PBCs over the frequency band 27-31 GHz in θs=0°-80° and in φ=0°,45°, and 90°. Simulation results show that the proposed antenna concept yields a wide frequency band (28-30.4 GHz) and $|S_{11}|$ < -10dB over the θs=0-60° in all azimuth angles (φ=0°,45°, and 90°), as depicted in **Figure 3.17**(a-c). To the best of author's knowledge, the presented performance is superior when compared to state-of-the-art single-fed CP antennas. Moreover, the antenna element shows an AR < 3dB θs=0°-30° and in φ=0°, θs=0-30° and in φ=0°, respectively, as shown in **Figure 3.18**(a-c).

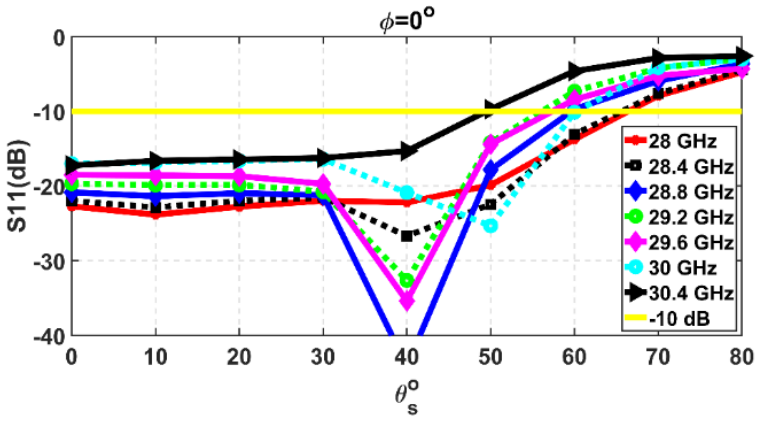

(a)

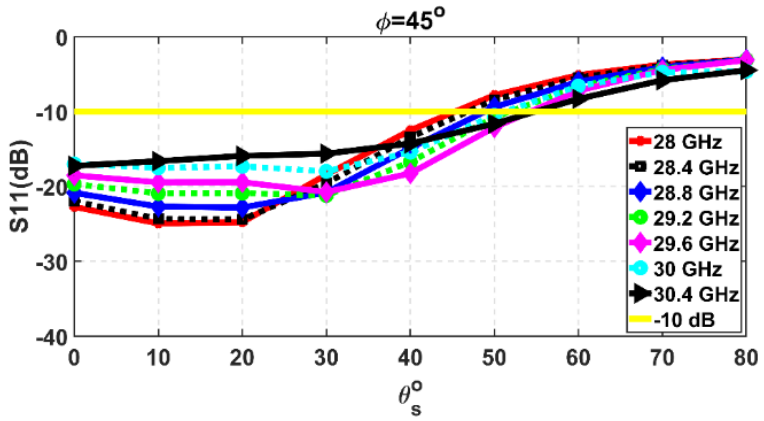

(b)

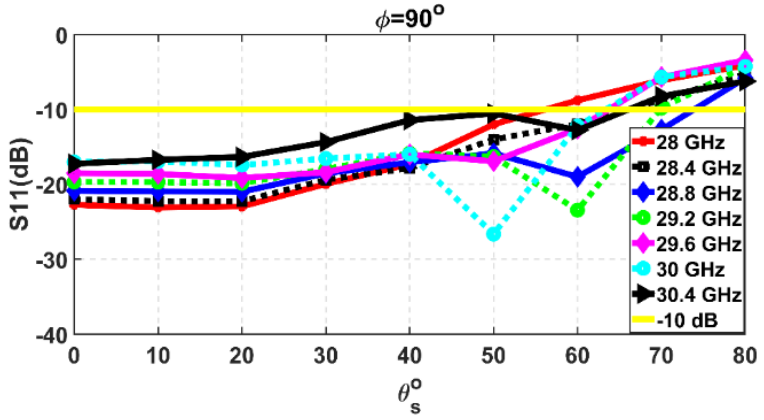

(c)

Figure 3.17: Simulated RL (S_{11}) versus scanning angle at: (a) phi=0°, (b) phi=45°, and (c) phi=90°.

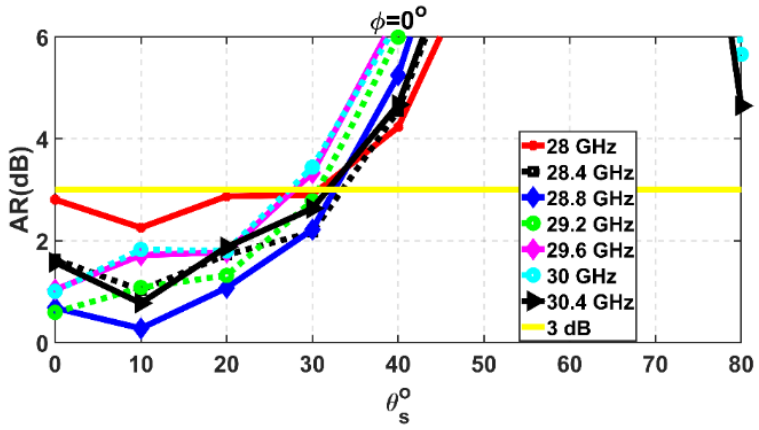

(a)

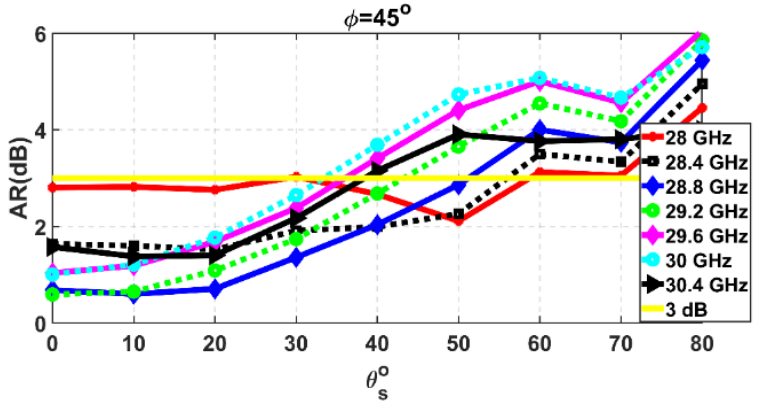

(b)

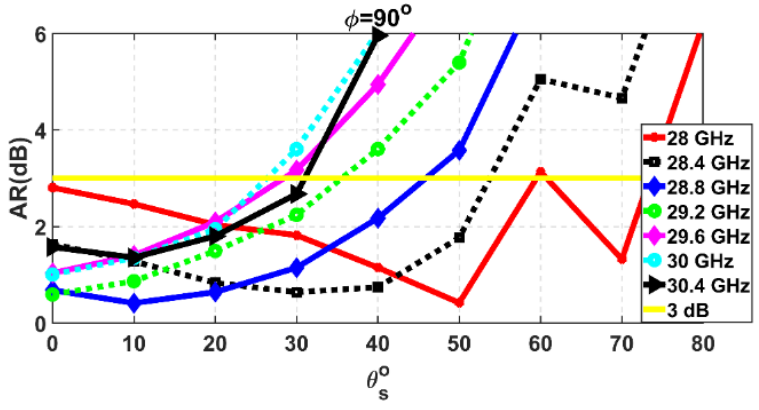

(c)

Figure 3.18: Simulated AR versus scanning angle at: (a) phi=0°, (b) phi=45°, and (c) phi=90°.

3.3.2 4×4 CP antenna subarray module

The antenna element proposed in Section 3.2 was used as a building block to construct a 4×4 fixed-beam CP antenna array module. The antenna module was implemented in a 20×20 mm^2 area with elements spacing of 5 mm ($0.5\lambda_o$ at 30 GHz). A corporate feeding network was used to excite the antenna element with uniform excitation, and a mini-connector with a diameter of 2 mm was used to feed the antenna module. The module was simulated with HFSS and the optimized structure, shown in **Figure 3.19**, was fabricated using a low-cost PCB technology. The fabricated antenna module is shown in **Figure 3.20**. A PNA-X from Keysight Technologies was employed to measure the RL of the fabricated antenna modules. Measurements showed that the proposed antenna module operates over a very wide frequency bandwidth with measured $|S_{11}| < -10$ dB over the frequency 27-31 GHz (~13.8% bandwidth). Furthermore, there is good agreement between the measured and simulated S_{11}, as shown in **Figure 3.21**. The small discrepancy seen between the measured and simulated S_{11} results is attributed to fabrication that allowed the two frequency resonances to shift apart from each other. The measured S_{11} bandwidth is wider than the simulated bandwidth with a marginal $|S_{11}| < -10$ dB, over the frequency band between the two resonance frequencies, especially at 28.5 GHz.

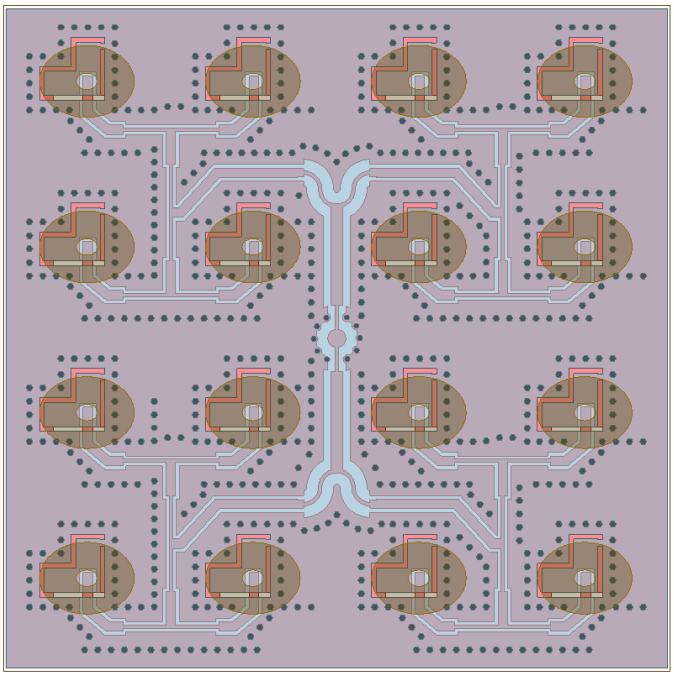

Figure 3.19: Proposed 4×4 antenna module.

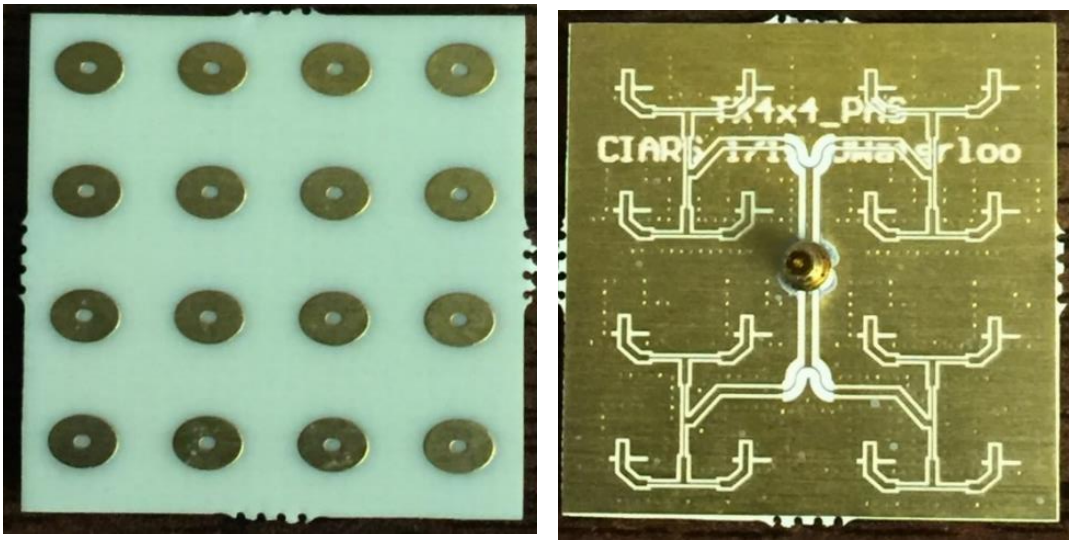

(a) (b)

Figure 3.20: Fabricated 4×4 antenna module: (a) top view, (b) bottom view.

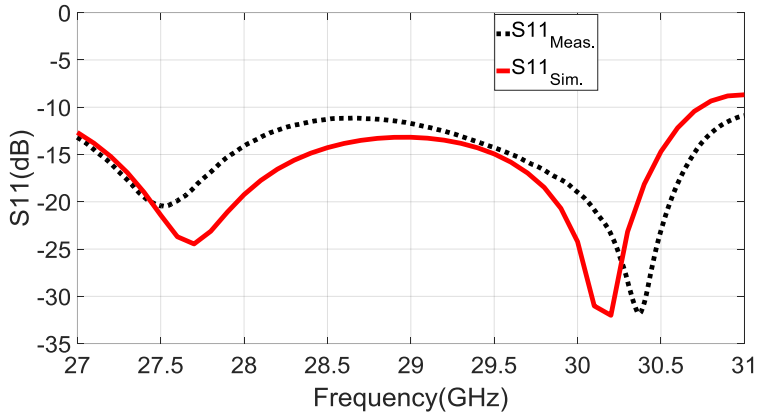

Figure 3.21: Measured and simulated S_{11} (dB).

A planar near-field (PNF) measurement system from NSI was utilized to measure the radiation characteristics (radiation pattern, AR, and directivity) of the fabricated module. The measured and simulated radiation patterns in the X-Z plane over the frequencies 27.6, 28.6, 29.6, and 30.6 GHz are shown in **Figure 3.22**. The antenna module shows an RHCP [Co-polarized (Co-pol)] pattern with a small LHCP [cross-polarized (X-pol)] component, and the realized X-pol discrimination (difference between the Co-pol and X-pol at boresight) is 16 dB, 42 dB, 18.5 dB, and 20 dB at the frequencies 27.6 GHz, 28.6 GHz, 29.6 GHz, and 30.6 GHz, respectively. As can be seen in **Figure 3.22**, the

measured RHCP and LHCP patterns match the simulated patterns very well, and both follow the simulated patterns over the entire measurement range.

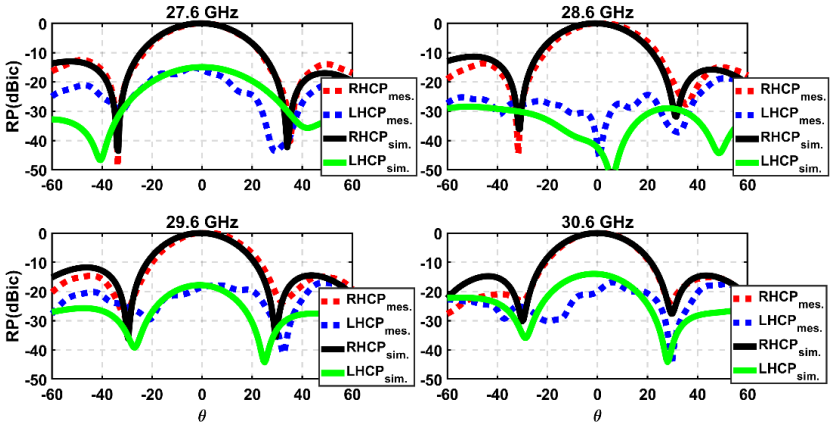

Figure 3.22: Measured and simulated radiation pattern (dBic).

Furthermore, the AR of the proposed antenna module was measured to validate the proposed concept as a novel structure to radiate a wide-band CP pattern. The measured and simulated AR are shown in **Figure 3.23**a. The proposed antenna module exhibits a measured AR <3 dB over the frequency range of 27.5-30.7 GHz (~11% bandwidth); such wide-band CP performance generated from a single-fed planar microstrip antenna array is one of the highest to be reported. The proposed antenna module shows a maximum measured directivity of 17 dB at 30.6 GHz and a minimum measured directivity of 15.7 dB at 27.5 GHz, within the frequency band of AR< 3 dB (27.5-30.7) GHz. The measured directivity (**Figure 3.23**b) showed good agreement with the simulated result with some discrepancy attributed to fabrication error.

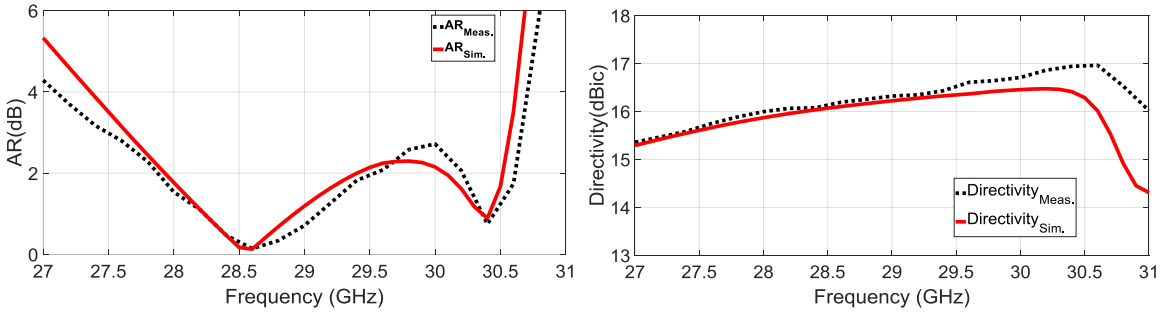

(a) (b)

Figure 3.23: Measured and simulated (a) AR (dB) and (b) directivity (dBic).

3.3.3 16×16 CP modular fixed-beam antenna array

Finally, the proposed antenna module was employed to build a 16×16 antenna array that consists of 16 antenna modules arranged in a square-shaped grid in order to evaluate the modularity concept. The developed array is shown in **Figure 3.24**a. A 1×16 substrate integrated waveguide (SIW)-based power splitter was utilized to excite the 16 antenna modules so that it mimicked the final configuration of a modular and scalable active phased array fed with hybrid feed networks. The simulation results for the 4×4 antenna module was used with AF to estimate the performance of the proposed 16×16 antenna array to reduce the simulation resources and computation time. The 16×16 array showed a measured $|S_{11}| < -10$ dB over the frequency band of 28.2-30.5 GHz (~8% bandwidth). The reduction in the S_{11} bandwidth is mainly attributed to the limited bandwidth of the SIW power splitter, which dominates over the bandwidth of the antenna modules. To validate this claim, the measured S_{11} of the SIW power splitter is plotted in **Figure 3.25**. As can be seen from the figure, the measured S_{11} of the SIW power splitter matches the measured S_{11} of the 16×16 antenna array.

The PNF measurement system was used to validate the simulated radiation characteristics of the proposed modular 16×16 antenna array. The radiation measurement setup is depicted in **Figure 3.24**b. The radiation pattern of the proposed modular 16×16 antenna array for different frequencies, compared to the simulated results of the single module multiplied by the AF, is plotted in **Figure 3.26**. Despite the mechanical misalignments and the amplitude and phase variations generated by the SIW power splitter, the modular 16×16 antenna array showed very symmetrical RHCP and LHCP components. Very good agreement was seen between the measurement and simulation results for the majority of the measurement frequency range. The measured X-pol discrimination is 13 dB at 27.6 GHz, 27.5 dB at 28.6 GHz, 18 dB at 29.6 GHz, and 19 dB at 30.6 GHz, respectively.

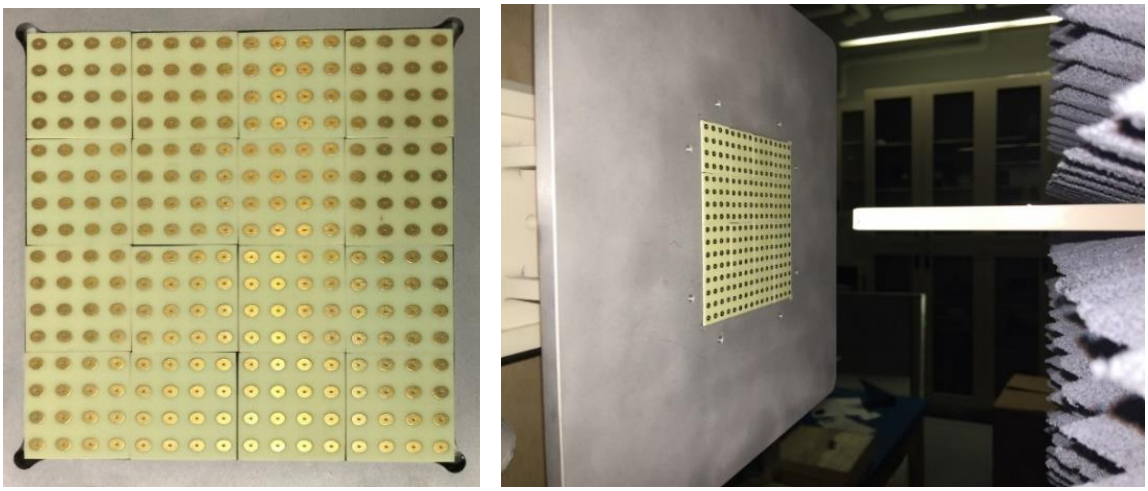

(a) (b)

Figure 3.24: (a) Modular 16×16 antenna array, (b) PNF measurement system.

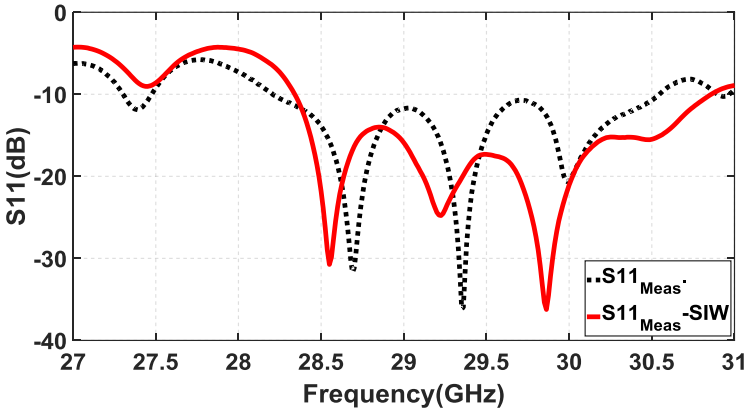

Figure 3.25: Measured S_{11} (dB) of modular 16×16 antenna array and SIW power splitter.

Moreover, measurements show that an AR<3 dB (Figure **3.27**a) was realized over the frequency band of 27.8-30.7 GHz (~10% bandwidth). The measured AR matches the simulated AR very well, and the reduction in the frequency band is attributed mainly to the phase and amplitude variation of the SIW power splitter. The amplitude variation imposes a nonuniform excitation on the modular 16×16 antenna array; as a consequence, the measured directivity reduces compared to the simulated result as shown in Figure **3.27**b. The directivity reduction is a valid justification to conclude that the antenna modules were not excited uniformly; the highest directivity is realized with uniform excitation of the antenna element of the array. The maximum measured directivity is 28.7 dB, achieved at 30.6 GHz.

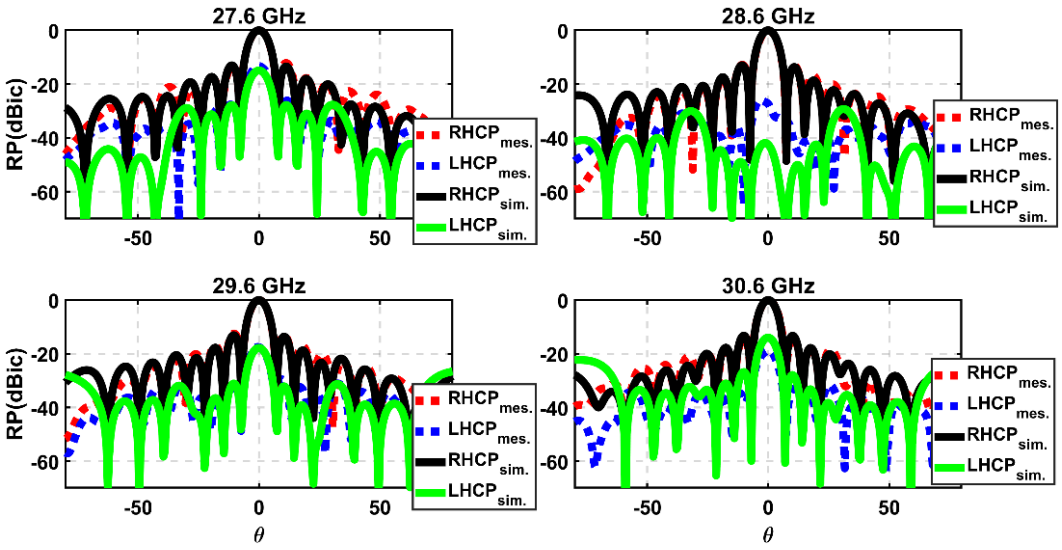

Figure 3.26: Measured and simulated radiation patterns (dBic).

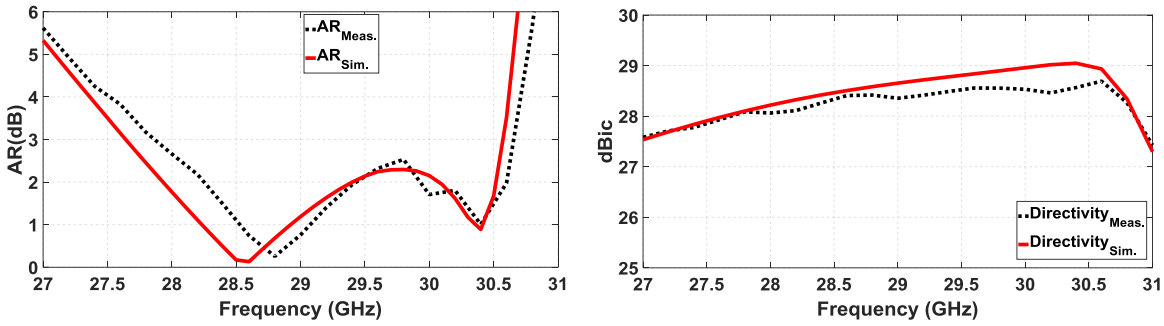

(a) (b)

Figure 3.27: Measured and simulated (a) AR (dB), (b) directivity (dBic).

3.4 Ka-band single-fed CP APAA

3.4.1 Antenna array structure and measurement setup

In Ka-band mobile SATCOM applications, the radiation pattern of the Tx APAA must meet very stringent radiation mask requirements [56-59] in terms of SLL, polarization purity, and pointing accuracy when the main beam is steered to a certain scan angle. As a result, full control of the magnitude and phase over the entire antenna array aperture is required. The antenna designed in this research was used in CIARS 4×16 active phased-array platform, as shown in **Figure 3.28**, where the phase and amplitude of each channel can be controlled.

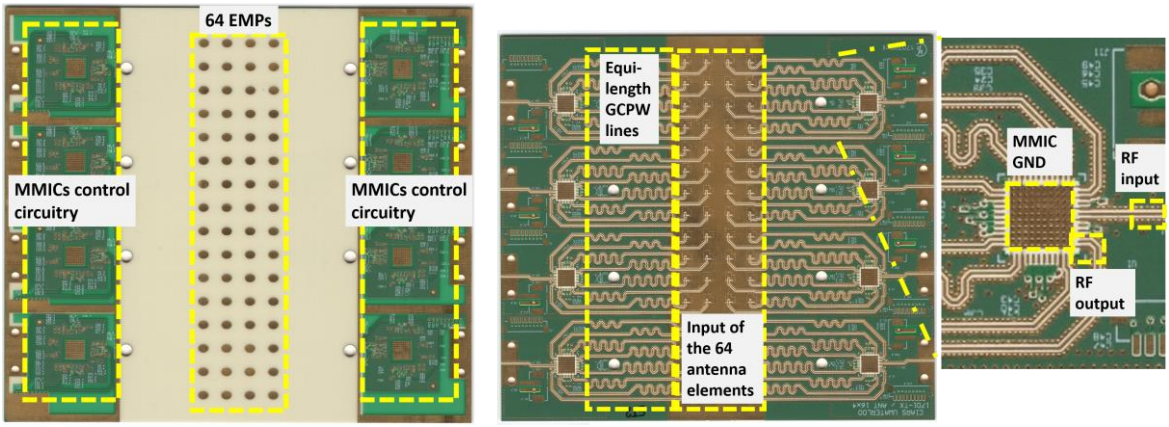

(a) (b)

Figure 3.28: Fabricated 4×16 Ka-band CP-APPA: (a) top view (antenna side) and (b) bottom view (MMIC chip side).

The PNF measurement system from NSI was used to test the radiation characteristics of the APAA for different steering angles (0^o-$\pm40^o$) at two different frequencies 29.5 GHz and 30 GHz. The steering angle was limited to $\pm40^o$ due to the appearance of grating lobe beyond these angles. **Figure 3.29** depicts the PNF measurement setup for this test. Measurement results were compared with the simulation results for validation. AF tool from ANYSYS was used to calculate the radiation pattern and the AR of the proposed 4×16 APAA. In all simulations, the elements were assumed to be excited by the same input power.

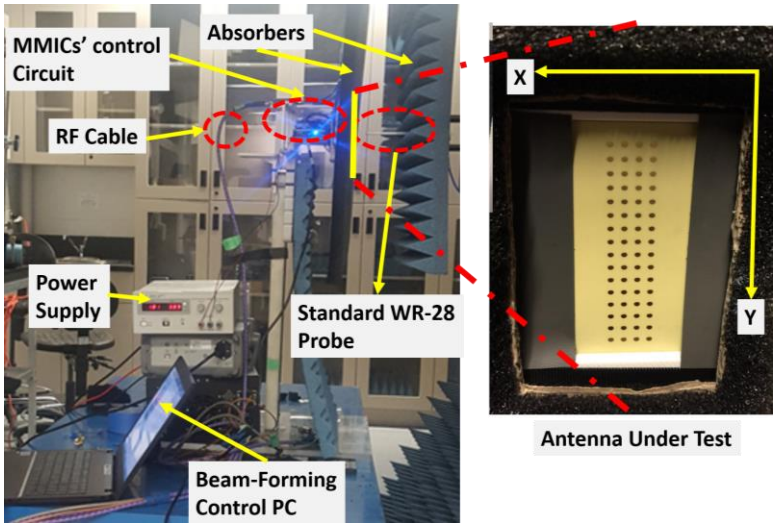

Figure 3.29: PNF measurement setup.

3.4.2 Antenna array measurement and simulations

The measured and simulated radiation patterns at 29.5 GHz and 30GHz for three different elevation angles are plotted in **Figure 3.30**a-**Figure 3.30**c. Measurements show that the APPA is capable of radiating RHCP power and its radiation pattern (main beam) can be steered over the elevation range from -40^{o} to +40 ^{o} in Y-Z plane. The measured radiation patterns match well with the simulated patters in all cases with minimal discrepancies. The antenna shows a low pointing error of less than 1.5^{o} at all steering angles, a characteristic that is highly desired for SATCOM applications. The discrepancies between the measured and simulated results could be attributed to three main factors. First, measurements are bounded the finite ground size as compared to the infinite ground imposed in the AF simulation. Second, the presence of the absorber close to the antenna under test (AUT), used to reduce the scattering/radiation effects of the RF cables. Third, fabrication errors and the dielectric constant uncertainties.

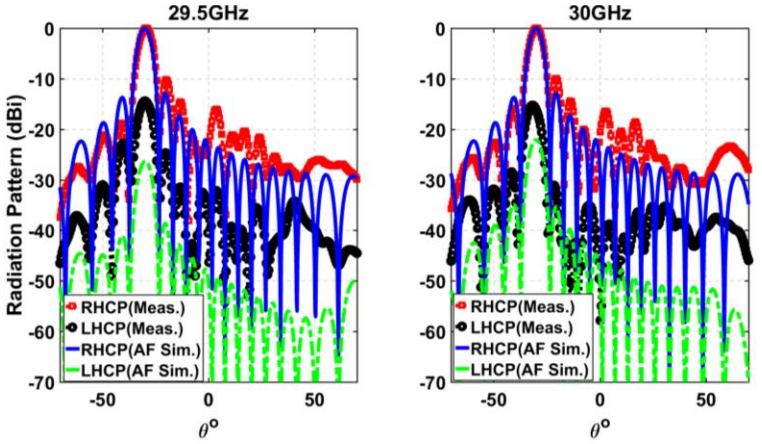

(a)

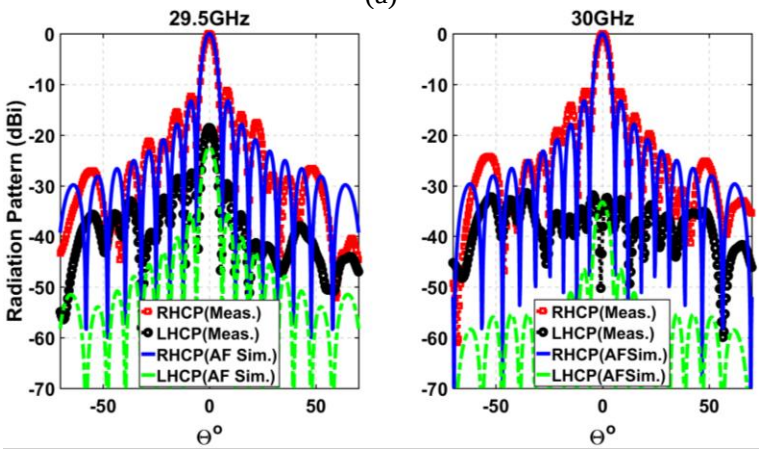

(b)

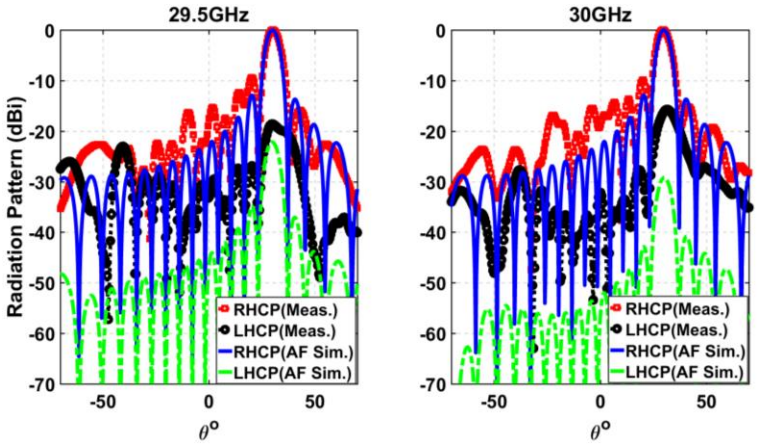

(c)

Figure 3.30: Measured and simulated radiation pattern in Y-Z plan at: (a) θs=-30°, (b) θs=0°, and (c) θs=30°.

The normalized RHCP radiation pattern at 30 GHz is shown in **Figure 3.31**a. It can be seen that the antenna shows a high pointing accuracy at different steering angles with an SLL of less than -10 dB in all steering angles. Furthermore, the APPA shows a good X-pol (LHCP) discrimination of better than 20 dB over the elevation range of θ_s=±20°, as shown in **Figure 3.31**b.

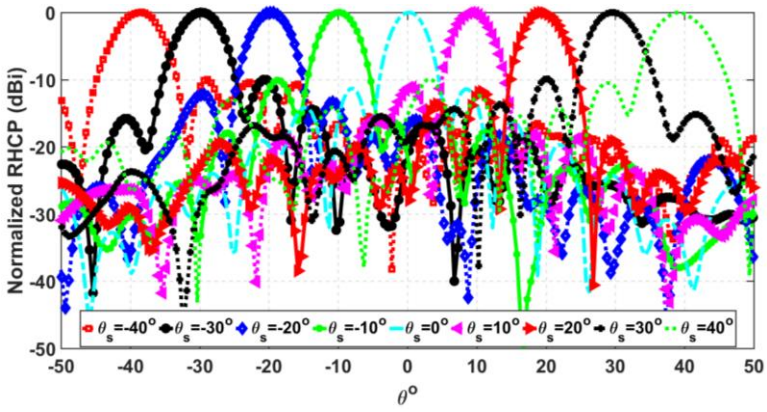

(a)

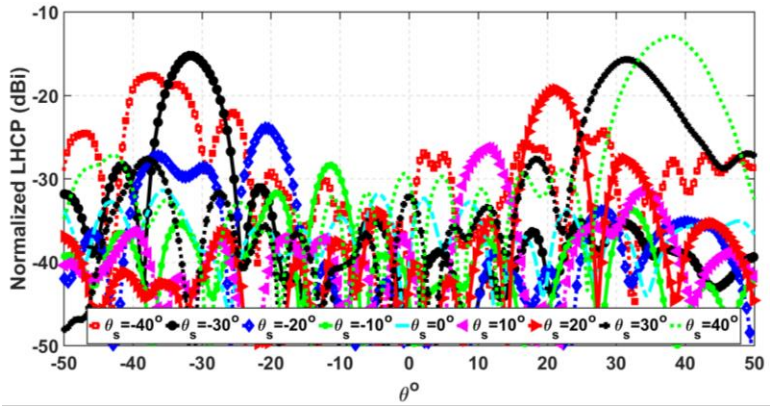

(b)

Figure 3.31: Measured normalized radiation pattern in Y-Z plan at 30 GHz: (a) RHCP (Co-pol) and (b) LHCP (X-pol).

The AR was measured over the scanning angle range and compared to simulated results. The APPA shows a measured AR < 4 dB in all steering angles at both frequencies 29.5 GHz and 30 GHz. The best AR level (0.17dB) was achieved at 30 GHz in the boresight direction. The measured AR follows the trend of the simulated AR at most of the steering angles, despite some mismatch at 40°, as shown in **Figure 3.32**.

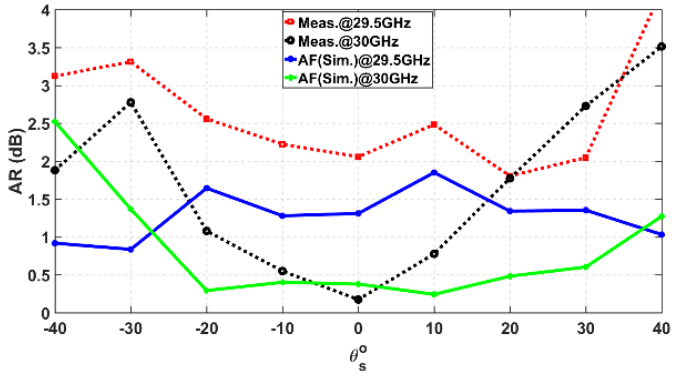

Figure 3.32: Measured and simulated AR at 29.5 GHz and 30 GHz.

Table 3.2 summarizes the measured and simulated results of the CP-APAA at 30 GHz for different steering angles. As can be seen from the figure, the main beam was steered very accurately towards the required angles with small pointing errors of less than 1.5°. Also, the 1st SLL remains at 10 dB over the same scanning range. Furthermore, the proposed CP-APAA shows an RHCP with good AR level, especially in the elevation range ±20°. The measured results correlate with those form AF simulation very well in most cases.

Table 3.2: Summary of Results at 30 GHz.

Pointing angle(θ_s^o)		1st SLL (dB)		X-Pol discrimination (dB)		AR (dB)	
AF	Meas.	AF	Meas.	AF	Meas.	AF	Meas.
-40	-38.5	12.78	10.04	16.83	19.35	2.52	1.88
-30	-29.9	12.91	10.02	22.1	16.1	1.37	2.74
-20	-19.6	13.06	12.25	35.47	24.15	0.3	1.08
-10	-9.77	13.17	10.1	32.72	30	0.4	0.55
0	0	13.28	11.33	33.25	40	0.38	0.17
10	9.5	13.17	11.11	37.11	27.2	0.24	0.76
20	19.4	13.06	11.75	31.14	19.85	0.48	1.77
30	29.83	12.91	9.9	29.19	16.15	0.6	2.73
40	39.5	12.8	10.51	22.73	14	1.27	3.51

To steer the beam of an array in a certain direction θ_s, and ϕ_s with appropriate aperture tapering is required for SLL control. the excitation phase and amplitude of each antenna element can be adjusted based on equation (3.9).

$$I_n = e^{-jk_o(sin\theta_s cos\varphi_s x_n + sin\theta_s sin\varphi_s y_n + cos\theta_s z_n)} e^{-\alpha(x_n^2 + y_n^2)} \quad (3.9)$$

Where I_n is the complex excitation of each element located at the location of (x_n, y_n, z_n). For a periodic planar array, one can simply write the antenna's location as ($x_{nm}=np_x$, $y_{nm}=mp_y$, $z_{nm}=0$) where (p_x,p_y) is the lattice vector of the periodic array and it is assumed that the array is located on the Z=0 plane.

Figure 33.33a shows the measured boresight RHCP radiation pattern of the 4×16 array when the tapering amplitude was reduced exponentially from the center to the edge of the array by 0 dB, 5 dB, and 11 dB, respectively. As the tapering increases from 0-dB to 11-dB, the SLL level drops from 13-dB to 25-dB. This capability is a highly desirable feature for SATCOM applications where the SLL must be kept below the standard mask. Moreover, as can be seen in Figure 33.33b, the X-pol component (LHCP) remained below -30 dB in all cases.

The CP-APPA can form a two-beam CP radiation pattern by splitting the RF-power between two radiation directions. Recently emerging LEO SATCOM applications [123] would require such a capacity. The CIARS multi-beam algorithm applied to the active beam-formers generated two beams.

Figure 3.34 demonstrates the measured radiation pattern of the 4×16 APAA when a complex excitation was applied to each antenna element to generate two different CP beams at -30° and +20° instantaneously, for two different power levels radiated at each beam. A similar approach can be extended to simultaneously radiate more than two beams that have similar or different radiated power levels.

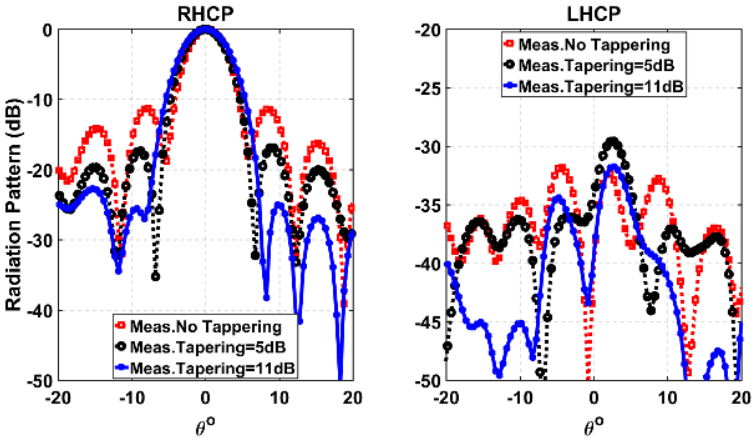

(a) (b)

Figure 33.33: Measured radiation pattern at 30 GHz for three different tapering cases (a) RHCP pattern, (b) LHCP pattern.

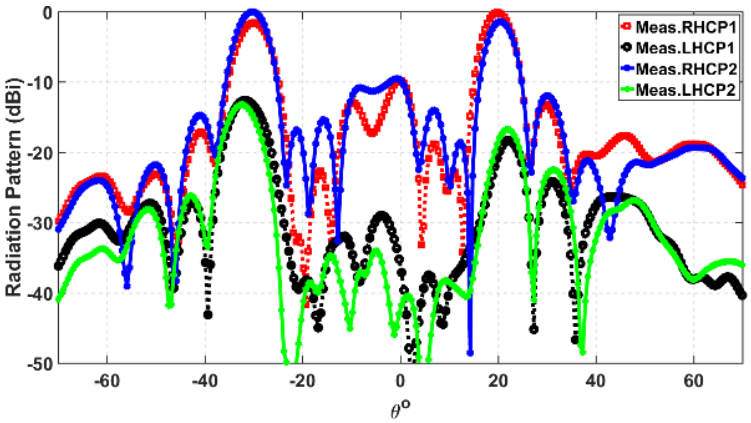

Figure 3.34: Measured multi-beam radiation pattern at 30 GHz.

3.5 Conclusion

A novel single-fed CP antenna concept was presented in this chapter. A wideband CP was realized by loading a multimode ring resonator with an elliptical microstrip patch antenna. Full-wave simulations show that the proposed antenna attained a wide scanning S_{11} < -10 dB and AR< 3dB. The antenna

element was used to develop a modular fixed-beam CP antenna array that was measured over a wide frequency band with excellent CP radiation pattern despite limitations imposed by the feed network and mechanical misalignment. The proposed antenna concept is an excellent candidate to develop a wide band and low-cost CP PAA with single sense of polarization for limited elevation scanning of $\pm 40^{o}$ off-boresight over entire azimuthal range. The developed antenna was used in CIARS 4×16 active phased-array platform and was successfully characterized. The measured results verified the design concepts proposed in this Chapter. The proposed antenna structure was designed in low-cost PCB technology and appears to be an excellent low-profile candidate to fulfill the rapidly growing demands for emerging Ka-band land, and close to land, SOTM applications. The active phased-array generated a high quality steerable RHCP beam over the frequency band of 29.5-30 GHz. The beam was steered over the elevation range of 0^{o}-$\pm 40^{o}$ with high X-pol discrimination and very low pointing errors in most of the measured cases. The CIARS active phased-array using the proposed antenna elements is a promising candidate for SATCOM applications, with an excellent control over the SLL, one of the most critical requirements for a ground terminal transmitted beam. Furthermore, multiple beam-forming was also demonstrated. Such functionality is highly desirable for emerging LEO SATCOM applications. To the best of the author's knowledge, no simple single-fed CP-APAA has been presented in the literature showing similar performance comparable with that of the proposed CP antenna concept.

Chapter 4

An Integrated Dual-Polarized Modular Active Phased-Array Antenna for Emerging Ka-Band SATCOMs

4.1 Introduction

The objective of this chapter is to develop a Ka-band dual-polarized highly integrated antenna element that will be used as a building block to construct a modular APAA system as an ultimate solution for SOTM applications. The proposed antenna is a dual-fed ACMPA developed with several metal layers (< 1.8 mm thickness). The top metal layers were used to build a wideband dual-fed ACMPA that can be used for wide beam-steering ≥ 70^{o} over the entire azimuthal plane. The bottom layers are employed to integrate the corporate feed network, the DC biasing lines, and the control lines of the beam-forming MMIC. The proposed antenna element and sub-array meet all the stringent requirements of SOTM (Section 2.2) as it can be used to radiate any polarization [LP, vertical or horizontal (VLP; HLP) or CP, (left or right handed (LHCP; RHCP)]. It was designed on a 5×5 mm^2 area to avoid the grating lobe at the highest operating frequency (30 GHz) when the beam is steered to (> 70^{o}). The antenna element has a wide operating frequency band ≥ 2 GHz, low mutual coupling, and achieved a RL < -10 dB over a wide steering angle of up to 60^{o} by employing an electrical via wall. Finally, high isolation between the two feeds allows the proposed element to generate very high CP purity with low X-pol.

Subsequently, the proposed 4×4 antenna sub-array was used in CIARS APAA module with 20×20 mm^2 area. The module including passive and active beam-forming devices was fabricated and successfully tested. This module was employed in modular Ka-band 16×16-antenna array, as a working prototype for Ka-band large-scale wideband polarization-agile APAA with wide beam-steering.

4.2 Dual-fed dual-polarized Ka-band antenna element

4.2.1 Antenna concept

The proposed antenna element was designed based on a dual-fed ACMPA concept [124]. The main radiator is a circular shaped microstrip patch with a radius of *R*, and it is fed with two orthogonal strip lines through two U-shaped aperture slots to realize a wideband operating frequency. This

configuration allows for the generation of symmetrical radiation characteristics with minimal spurious radiation. A metallic square ring with vertical electrical via walls was used to reduce mutual coupling and to suppress undesired surface waves; hence, the proposed antenna operates over a wide beam-steering angular range. Ground islands with optimized shapes were employed to enhance the isolation between the two strip feed lines to achieve a flat isolation response over the operating frequency band. Consequently, high polarization purity can be achieved. A GCPW line was utilized to directly connect the antenna's feed to two of the RF channels of the beam-forming MMIC, and a vertical coaxial substrate integrated line was used as the transition between the GCPW line and the strip line, so the effects of the corporate feed network, control line, and DC biasing lines on the antenna feeds are minimal. The proposed antenna structure is shown in **Figure 4.1**. High performance dielectric material with ε_r=3 and dielectric loss of tanδ=0.0017 was used to develop the proposed antenna element, and state-of-the-art PCB fabrication technology with every layer via lamination was used to fabricate a working prototype.

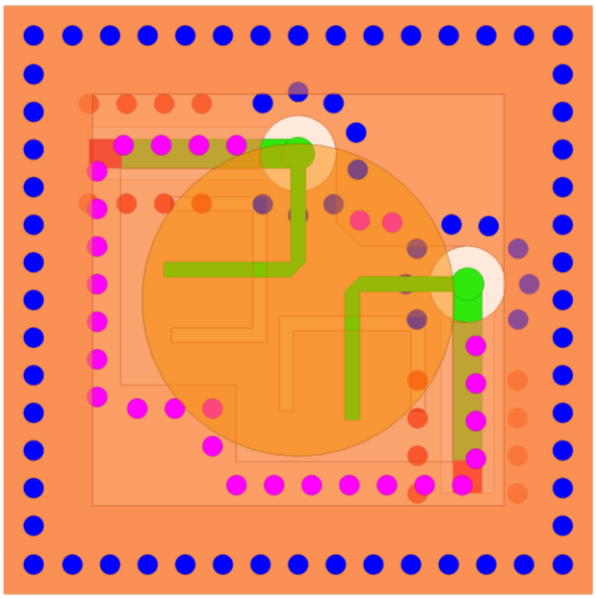

Figure 4.1: Proposed dual-polarized ACMPA element.

4.2.2 Design and simulation results

The antenna design started with the required performance characteristics and the available PCB technology. The radius of the circular microstrip patch was initially calculated by simple analytical formulations (4.1) -(4.4) [61].

$$R = \frac{F}{\left\{1+\frac{2h}{\pi\varepsilon_r F}\left[ln\left(\frac{\pi F}{2h}\right)+1.7726\right]\right\}^{\frac{1}{2}}} \quad (4.1)$$

$$F = \frac{8.791\times10^9}{f_r\sqrt{\varepsilon_r}} \quad (4.2)$$

Equation (2.1) does not take into consideration the fringing effect. Since fringing makes the patch electrically larger, the effective radius of patch is used and is given by

$$R_e = R\left\{1+\frac{2h}{\pi\varepsilon_r R}\left[ln\left(\frac{\pi R}{2h}\right)+1.7726\right]\right\}^{\frac{1}{2}} \quad (4.3)$$

Hence, the resonant frequency for the dominant mode TM^z_{110} is given by

$$(f_r)_{110} = \frac{1.8412v_o}{2\pi R_e\sqrt{\varepsilon_r}} \quad (4.4)$$

Where R is the radius of the circular patch, R_e is the effective patch radius due to fringing field, h is thickness of the patch substrate, ε_r is the permittivity of the patch substrate, and f_r is the dominant resonance frequency of the circular patch.

The length of the aperture slots was initially set to a half-guided wavelength ($\lambda_g/2$), and strip TLs with quarter-guided wavelength ($\lambda_g/4$) open-ended stubs were used to excite the two orthogonal modes. Full-wave simulation was used to optimize the dimensions of the proposed antenna and took into consideration the thicknesses of the metallic layers and the dielectric substrates after fabrication. The square metallic ring and the vertical electrical via walls were mounted in the design, and design tuning was performed on the antenna parameters to maintain the antenna performance. After extracting the final design parameters, the GCPW-strip transition was designed for 50Ω characteristic impedance to include the footprint of the MMIC output channels. The optimized transition was integrated with the antenna structure; the feed network circuit, control lines, and DC biasing lines were mounted in the design to ensure they imposed minimal impacts on the feed transition. The proposed antenna was designed with a 5x5mm^2 ground size ($0.5\lambda_o$x$0.5\lambda_o$) at 30 GHz.

The optimized antenna element was simulated with periodic boundary conditions over the frequency range of 29-31 GHz for different scanning angles in θ and φ. At the boresight, the antenna shows a RL $|S_{11}|$ and $|S_{22}|$ of < -10 dB over 2 GHz (6.7% bandwidth) frequency band and the best simulated results appeared at 29.75 GHz with $|S_{11}|$=-37 dB and $|S_{22}|$=-33 dB. The difference between the two values is attributed to a small asymmetry in the locations of the U-shaped slots. This difference can be reduced by tuning the length of the open stub of the second port. Furthermore, the

simulated isolation factor $|S_{12}|$ between the two feed ports was <-21.5 dB over the operating frequency. This is attributed to the via walls and the ground shape on the strip line layer and, interestingly, it stays almost flat. The simulated S-parameters are shown in **Figure 4.2**.

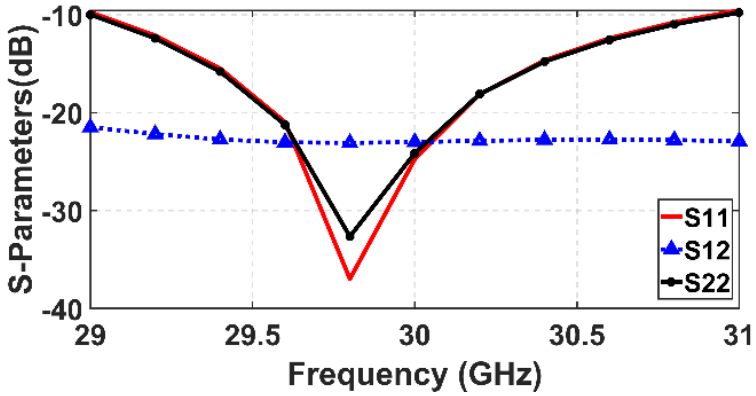

Figure 4.2: Simulated S-parameters (dB).

The proposed antenna element can be used to generate any sense of polarization; by controlling the excitation phase and the amplitude applied to the feeding ports VLP, HLP, LHCP, and RHCP can be easily realized with high polarization purity. When the two ports were excited with the same amplitude and a ±90° phase difference, a high purity CP (RH/LH) pattern was radiated from the proposed antenna element over the operating frequency band, and the realized AR was < 0.6 dB. The best achieved AR (0.1 dB) was achieved at 30 GHz, as shown in **Figure 4.3**a. The simulated radiation pattern at 30 GHz is shown in **Figure 4.3**b. The proposed antenna element radiates an RHCP pattern with an excellent X-pol discrimination of 44.5 dB and gain of 4.65 dBic at the boresight.

To evaluate the performance and the symmetry of the proposed antenna element, given its role as a critical building block in SOTM beam-steering applications. The element was simulated over the operating frequency band for an elevation angular range of θ_s=0°-70° and over the azimuthal angular values of φ=0°, 45°, and 90°. High symmetry was observed between the two ports for all simulated cases. This symmetry is an advantage for the proposed antenna element as it can help to reduce the calibration time, very critical and time-consuming process in SOTM antenna systems.

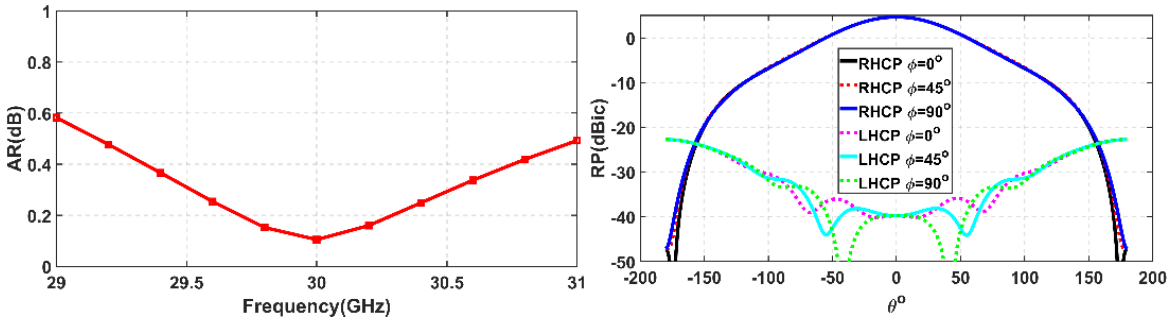

(a) (b)

Figure 4.3: Simulated (a) AR (dB), and (b) radiation pattern (dBic).

The antenna showed an $|S_{11}|$ of < -10 dB over the frequency range of 29.2-30 GHz for the scanning range of θ_s=0°-50° in φ=0° and 45°, and an $|S_{11}|$ of <-10 dB for the scanning range of θ_s=0°-40° in φ=90°. Similarly, the simulated $|S_{22}|$ was < -10 dB over the frequency range of 29.2-30 GHz for the scanning range of θ_s=0°-50° in φ=90° and 45°, and $|S_{22}|$ was <-10 dB over the scanning range of θ_s=0°-40° in φ=0°. The results are shown in **Figure 4.4**a and **Figure 4.4**b. The attained port isolation was $|S_{21}|$ < -20 dB over the frequency band of 29.-30.4 GHz for the scanning ranges of θ_s=0°-70° in φ=0° and 90°; however, it reduced to < -10 dB for θ_s=0°-50° in φ=45°, as shown in **Figure 4.4**c.

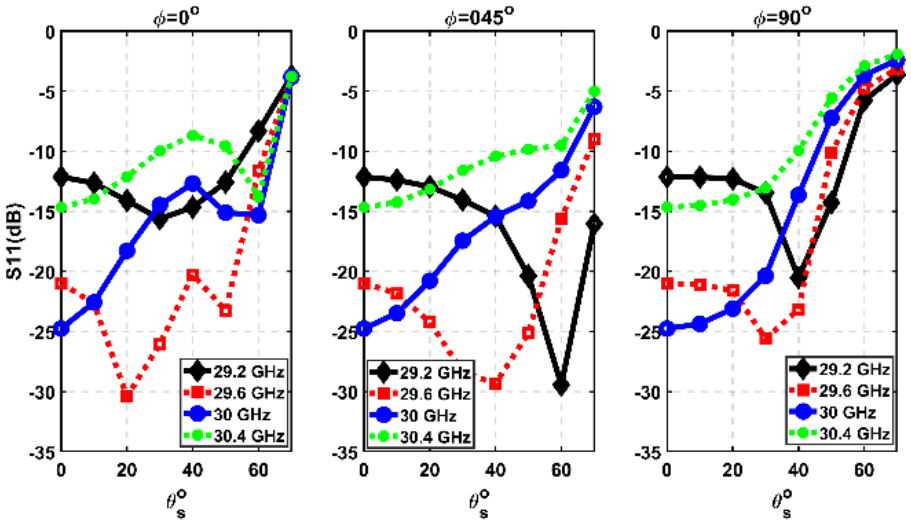

(a)

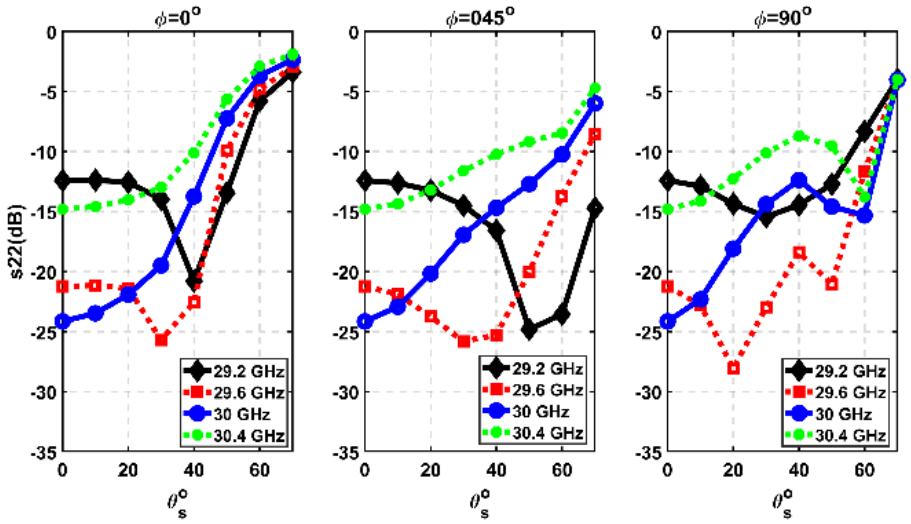

(b)

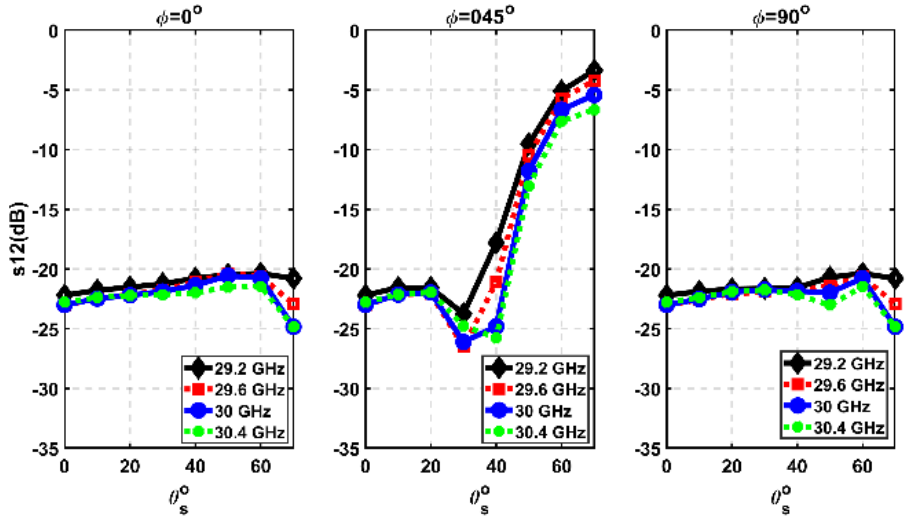

(c)

Figure 4.4: Simulated S-parameters (dB) versus scanning angle ($\boldsymbol{\theta_s^o}$) at (a) S_{11}, (b) S22, and (c) S12.

4.3 Modular dual-polarized Ka-band APAA

4.3.1 4×4 antenna module

The antenna array developed in Section 4.2 was used in CIARS active 4×4 antenna sub-array module (16 dual-fed elements) for a Ka-band SOTM PAA. A one-to-four strip line-based power splitter is used to distribute the RF signal uniformly to excite four beam-forming MMIC, where each MMIC

will feed four antenna elements with controllable amplitude and phase. A mini RF connector with a 2 mm diameter was used to feed the one-to-four power splitter at the center of the 4×4 antenna module through a vertical transition. The 4×4 antenna module has an area of 20x20 mm^2. The top and bottom views of the 4×4 active phased-array modules are shown in **Figure 4.5**. This antenna module is compact, has wide beam-steering capabilities, and polarization-agile. It can be used for mass production of any size of customized large-scale APAA for emerging mm-W applications.

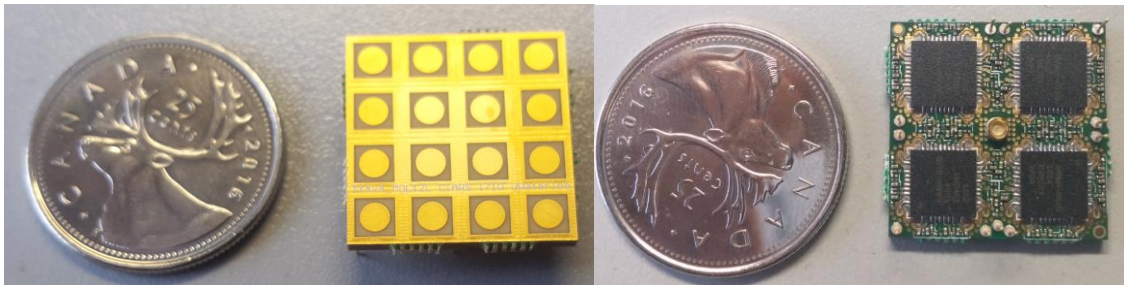

(a) (b)

Figure 4.5: 4×4 active phased array module uses the antenna array developed in this research(a) top view, (b) bottom view.

4.3.2 Modular 16×16 wideband APAA

As a proof-of-concept, the 4×4 active phased-array antenna module was utilized to build a 16×16 APAA. A 1×16 SIW based power splitter was used as a backbone in the proposed antenna array, where the 16 antenna modules were connected in a square grid and a metallic fixture was used in the assembly as shown in **Figure 4.6**. The assembled structure was tested under varying scenarios in an anechoic chamber using a planar near-field (PNF) measurement system; however, for brevity only RHCP cases are reported here to illustrate the antenna array polarization performance. For the purposes of comparison and validation of the measurement results, the 4×4 antenna module was simulated with a full-wave simulator for the boresight case and the results were multiplied by AF to calculate the expected performance of the 16×16 APAA as if the 16×16 antennas were excited uniformly with the same amplitude and phase. This comparison will help to validate the advantages of the modularity concept as the best solution for large-scale antenna arrays. It is worth mentioning that for simplicity the antenna under test (AUT) was calibrated in the boresight at 30 GHz only, and the antenna elements were assumed to be matched over the entire scan range.

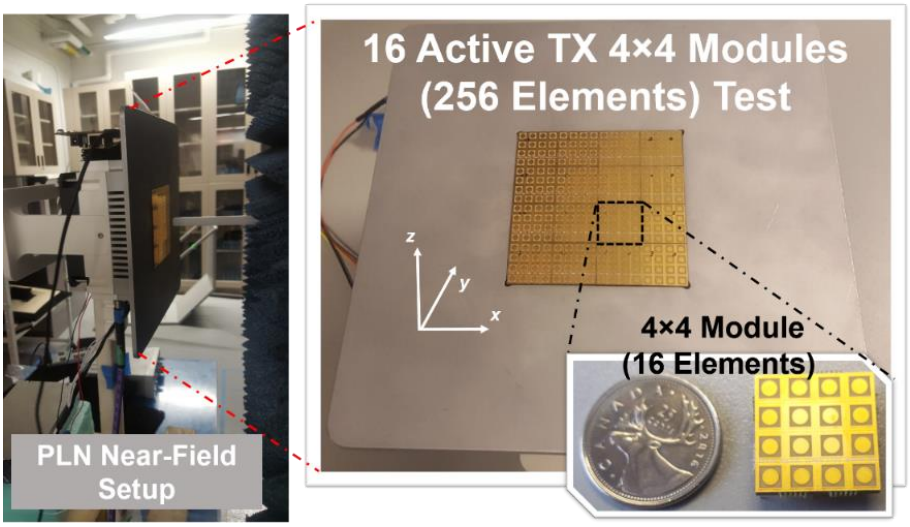

Figure 4.6: 16×16 modular APAA and its measurement setup.

4.3.3 Measurement and simulation results

The dual-polarized 16×16 APAA, which uses the antenna elements and 4×4 sub-arrays developed in this research, was tested over the frequency range of 28-31 GHz for four scanning angles in the X-Z plane (See **Figure 4.6**), and it was calibrated at the boresight at 30 GHz to radiate a RHCP pattern. The first measurement was carried out for the boresight, where all ports were excited with the same amplitude and a 90^{o} phase difference between the vertical port and the horizontal ports based on the measured data of the MMIC chip. Measurements show that the AUT radiates a symmetrical and very high purity RHCP pattern over the measurement frequency band in both X-Z and Y-Z planes. The best realized X-pol discrimination of 41 dB was achieved at 30 GHz; to be expected as the AUT was calibrated at this frequency. Furthermore, the antenna element shows the best AR at 30 GHz. This level of polarization purity is an exceptional result when compared to others reported to date at this frequency range and array size, and from modular based structures. The realized cross-polarization values at 28 GHz, 29 GHz, and 31 GHz were 29.3 dB, 32.3 dB, and 34 dB, respectively. The measured 1st SLL were -10.84 dB, -11.1 dB, -11.5 dB, and -9.9 dB sequentially over the measurement frequency band as shown in **Figure 4.7**. The measured results match those generated by simulation very well over the operating frequency band. The measured RHCP and LHCP components mimic almost all the simulated nulls and have an almost identical shape for both X-Z and Y-Z planes, as illustrated in **Figure 4.7**, and **Figure 4.8**, despite the impurities resulting from the feed circuit, MMIC channels, and mechanical misalignments.

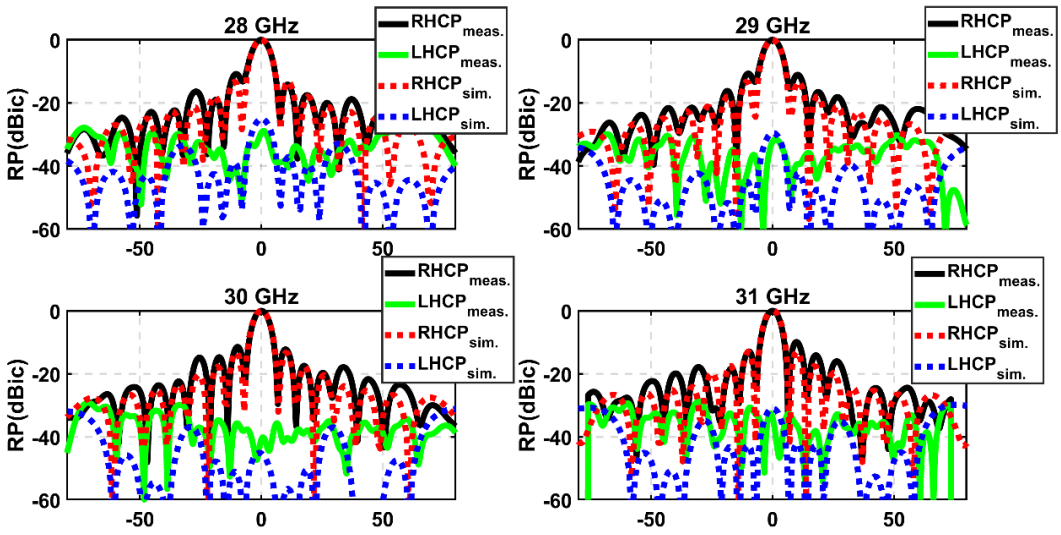

Figure 4.7: Measured and simulated radiation pattern of modular 16×16 active phased array in X-Z plane (boresight).

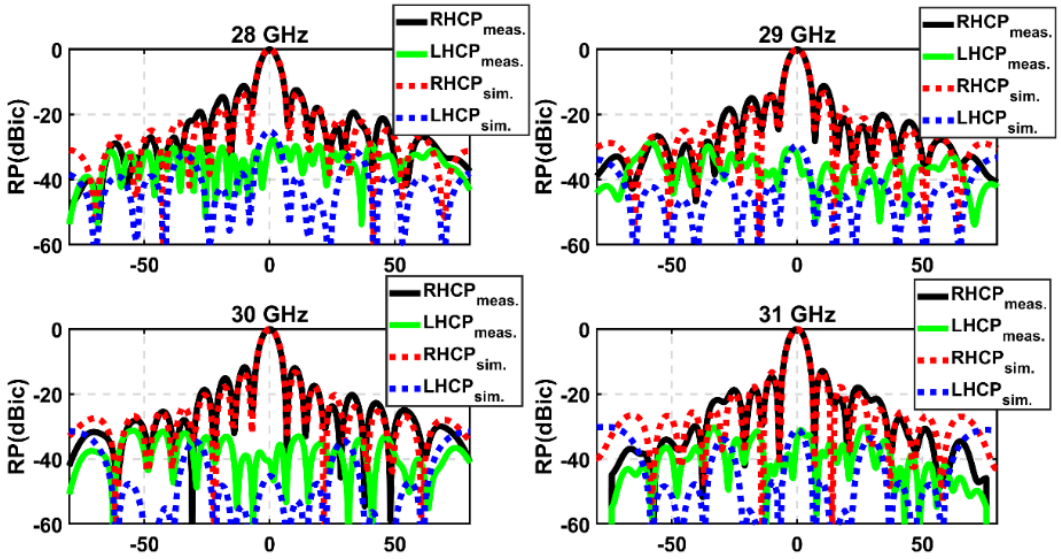

Figure 4.8: Measured and simulated radiation pattern of the modular 16×16 active phased array in Y-Z plane (boresight).

Similarly, the measured AR (depicted in **Figure 4.9**) resembles the simulated AR with very good agreement over the frequency band of 28-31 GHz. At 30 GHz, the AUT showed a very low measured AR of 0.15 dB only. For further validation, the directivity of the AUT was measured and compared with the AF simulation results. The measured and simulated directivities are shown in **Figure 4.10**, A measured directivity at 30 GHz of 28.72 dB was realized compared to the 29.1 dB simulated

directivity. Therefore, less than a 0.4 dB difference between the measured and simulated directivity was observed; a minimal difference if we take into consideration all of the measurement, assembly, and feed circuit impurities.

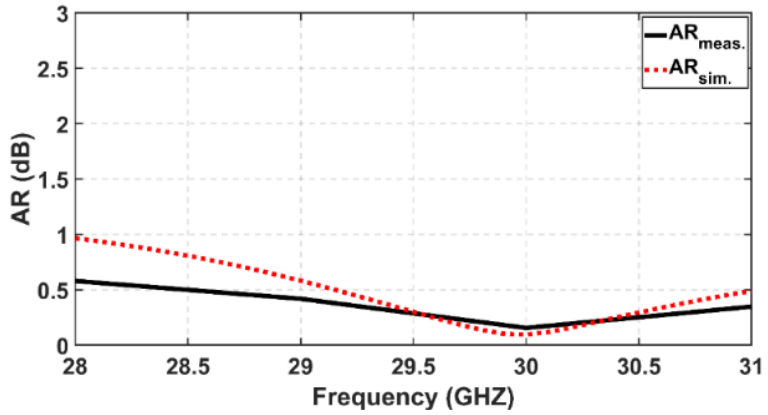

Figure 4.9: Measured and simulated AR (dB).

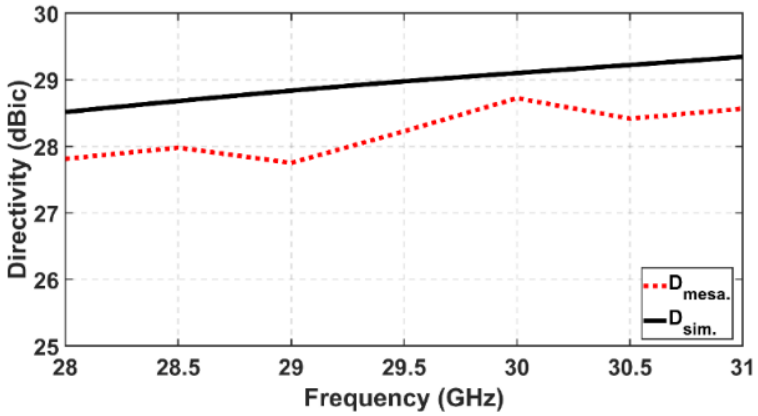

Figure 4.10: Measured and simulated directivity (dBic.)

The second measurement was performed at a scanning angle of 30^{o} in the X-Z plane, based on the calibration data that was obtained at the boresight. As can be seen from **Figure 4.11**, the AUT sustained a good AR level and 1st SLL across the entire operating frequency band. The achieved X-pol discrimination and 1st SLL at 28 GHz, 29 GHz, 30 GHz, and 31 GHz were 19.04 dB and -11.02 dB; 20.17 dB and -11.14 dB; 21.8 dB and -11.6 dB; and 23.6 dB and -11.5 dB respectively.

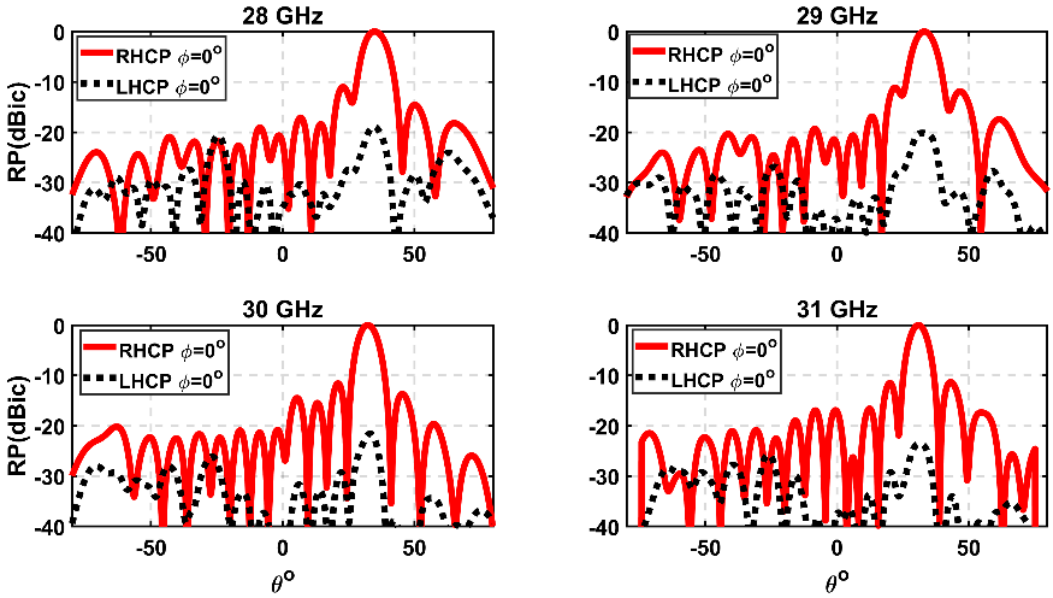

Figure 4.11: Measured and simulated radiation pattern of the modular 16×16 active phased array in X-Z plane (θ_s=30°).

In addition, the AUT was steered to wide scanning angles (θ_s=50° and 60°) over the operating frequency 28-31 GHz without calibration. It shows an excellent and well-shaped Co-pol component (RHCP) in both cases, especially at 30 GHz. However, the X-pol component deteriorates as the scanning angle increases—expected behavior given the impedance variation of the second feed component (Y polarized) as shown in **Figure 4.12** and **Figure 4.13**. Nevertheless, this performance degradation can be easily eliminated if a higher power is injected to the second feed of the antenna elements that is 3 dB higher than the amplitude of the first port (X polarized). To validate this explanation, a full-wave simulation was performed on the antenna element in PBC's. As the power level of the second port increased by 3 dB compared to the first port, the antenna array retained its polarization purity with an X-pol discrimination of > 40 dB at 30 GHz when steered to θ_s=60°, as shown in **Figure 4.14**.

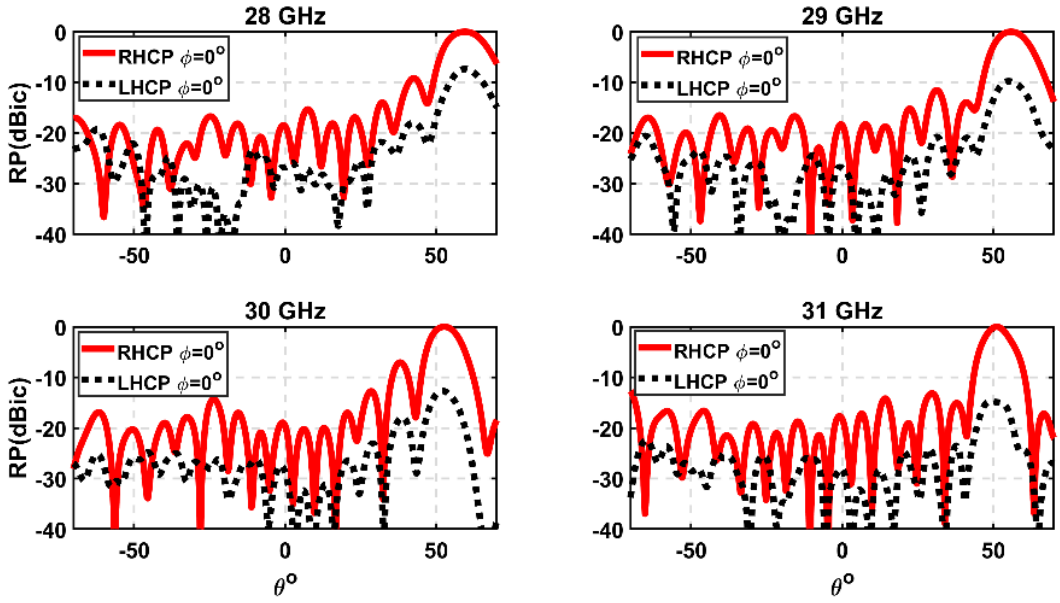

Figure 4.12: Measured and simulated radiation pattern of the modular 16×16 APAA in X-Z plane (θs=50º).

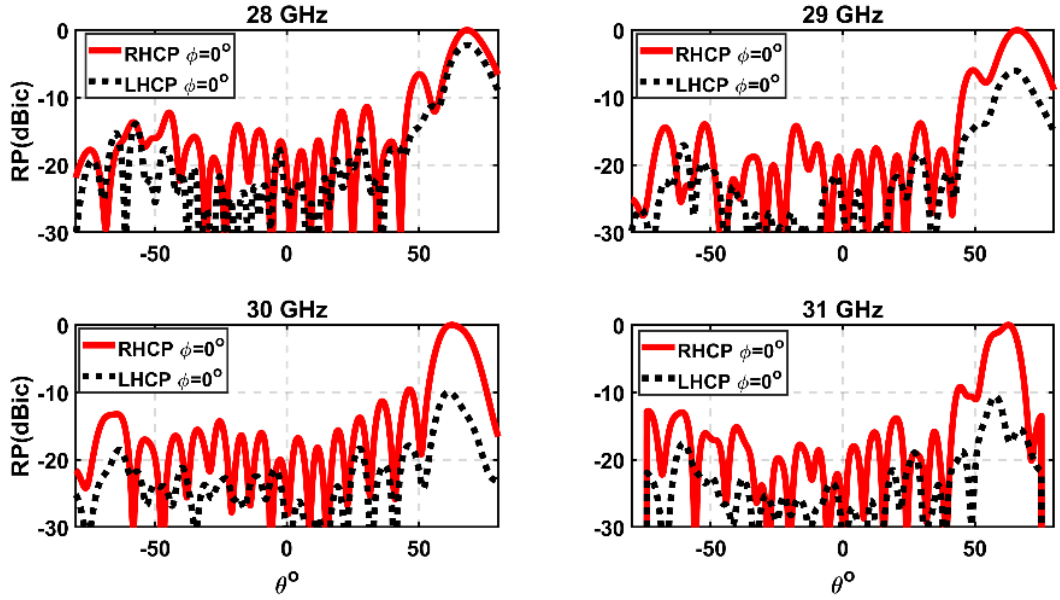

Figure 4.13: Measured and simulated radiation pattern of the modular 16×16 APAA in X-Z plane (θs=60º).

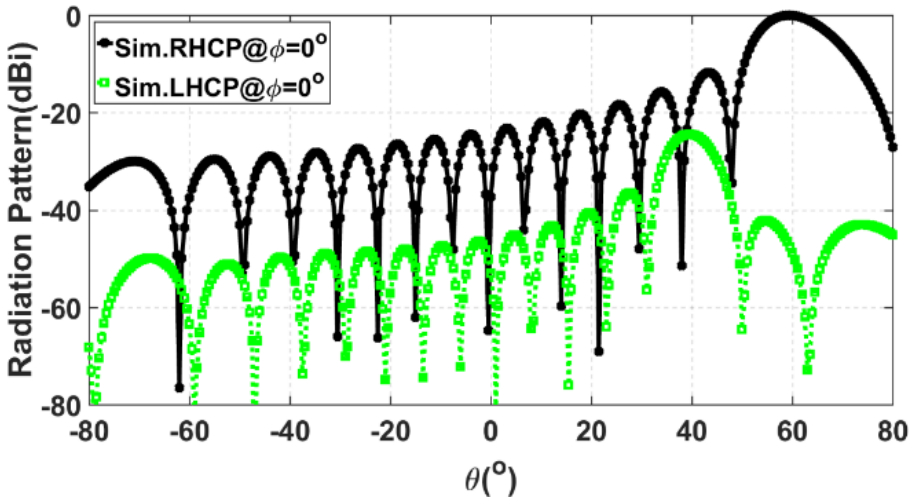

Figure 4.14: Simulated radiation pattern of the modular 16×16 APAA in X-Z plane (θs=60°) after excitation correction.

4.4 Conclusion

Successful test results of CIARS modular 4×4 and 16×16 active modular phased-array architectures, using the dual polarized antenna elements and sub-arrays developed in this research verified the validity of the proposed antenna element/sub-array concepts for wideband and wide beam-steering CP Ka-band applications. The proposed antenna design ideas were validated both in measurement and simulation. Despite the impurities of the feeding network, MMIC channels, and mechanical misalignment, the proposed antenna was steered over a wide scanning angular range of θ_s=0°-60° with well-shaped RHCP components over a 3 GHz frequency band centered at 29.5 GHz. The achieved results were obtained with a single calibration test at a single frequency; however, the superiority of the proposed concept over state-of-the-art calibrated complex APAAs [21] has been demonstrated.

Chapter 5

A Low-cost and low loss Ka-band phase shifter

5.1 Introduction

This chapter reports analysis, simulation, optimization, and design refinement of the new CIARS BLT phase-shifter to be integrated with a large-scale mm-W PAAs. I also investigated new packaging technology for this new phase-shifter and explored downsizing and broad-banding techniques, which significantly facilitate its integration into the array beam-forming network. For demonstration, the phase-shifter was designed for Ka-band. The proposed phase shifter is an extension of the initial phase shifting concept proposed in [116-117]. It is comprised of a grounded CPW (GCPW) TL loaded with a high dielectric constant slab, and a mechanical actuator that precisely controls the height of the air gap between the slab and the line. In this way, a tunable phase shifter is realized with low IL and high FOM. In order to develop a low-cost, low power consumption, high phase shifting range, and low IL phase shifter, different dielectric constant slabs (ranging between ε_r=42-100) were investigated as part of this research. The goal was to determine an effective method to increase the realized phase shifting range within a small footprint and low IL. In an attempt to reduce the profile of the phase shifter as well as its power consumption, two different mechanical actuators were employed, piezoelectric transducer (PET) and a magnetic actuator. Moreover, three different GCPW line configurations were utilized throughout this research as a means to miniaturize the phase shifter.

5.2 Proposed phase shifting concept

The BLT phase shifter consists of a high dielectric constant slab placed on top of a GCPW line with a mechanical actuator controlling the height of the airgap (h_{gap}), as shown in Figure 5.1. Because of its extremely high dielectric constant (42-250), the dielectric slab plays the role of a perfect magnetic conductor (PMC) medium and is almost impenetrable for the propagating mode. The propagation mode is mainly guided in the airgap between the GCPW line [effectively a perfect electrical conductor (PEC)], and the extremely high dielectric constant slab [effectively a PMC medium]. The propagation constant of this PEC-PMC waveguide is essentially changed as a function of the airgap height [116-117 and 125]. The propagation mechanism of this new wave-guiding structure was fully analyzed in [116]. The interesting aspect of the proposed phase shifter is that its operation is based on travelling wave delay—essentially the length of the phase shifter divided by the speed of electromagnetic wave in the wave guiding region. The choice of the GCPW configuration for high

performance antenna arrays was made because the phase shifter and active devices (if needed) can be integrated on one side, and the other side (bottom ground) can be used as a ground plane to reduce the interference between the feed circuit and the radiating antennas. As the airgap height varies, there is an increase in the input and the output RL mismatch (particularly at smaller airgap heights) due to the change of the characteristic impedance of the phase shifting component. In this research, a simple, wideband, and effective matching method based on optimization of the width of the gap and/or the line width of the GCPW segment under the dielectric slab is presented. The intention is to significantly reduce the RL mismatch of the phase shifter over the operating frequency band. A highly desirable feature of this new phase shifter is that the same device can be used for both receiver and transmitter without significant deterioration of the performance since the phase shifter is a reciprocal device with almost linear phase-frequency response. This feature is necessary for interleaved arrays, where the cost and complexity of the feed circuit and the phase shifter integration are important issues. Moreover, this phase shifter is directly integrated within the feeding network with no extra wire bonding or ball grid array interconnections. The main advantages of this new phase shifter include:

1. Small IL due to the fact that the wave is propagating mainly in the air gap.
2. For the same reason, the IL has minimal variation over the phase shifting range.
3. Relatively small footprint in terms of wavelength since a high dielectric slab is used.
4. Small actuation range (≤50 μm) required to attain the required phase shift range, making the proposed phase shifting concept low-profile.

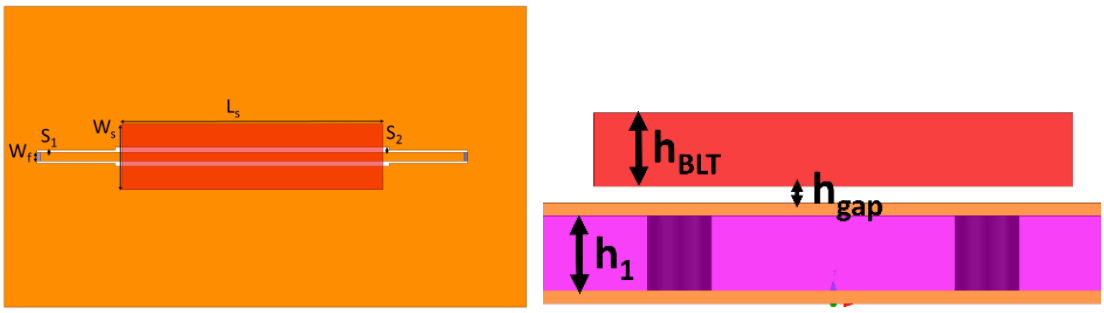

Figure 5.1: Phase shifter structure labelled with design parameters: W_f=0.14 mm, S_1=0.03 mm, S_2=0.1 mm, and W_s=1 mm.

5.2.1 Phase shifter analysis

Since the phase shifter will be integrated under the antenna element that has a 5×5 mm^2 area at 30 GHz, this area should house both the new phase shifter and parts of the feed circuit. The antenna element area size is the upper bound for the phase shifter; however, efforts are made to make the phase shifter smaller than this limit to facilitate circuit assembly and packaging. On the other hand, the lower bound on the size of the phase shifter is limited by the required phase variation (i.e., $\geq 360^o$). The characteristics of the optimized phase shifter can be obtained based on the area assigned for the phase shifter, maximum phase variation, and dielectric permittivity of the dielectric slab. The design steps can be summarized as follows:

1. Trace width and gap of the 50 Ω GCPW line are calculated at the operating frequency.
2. Length of the dielectric slab calculated to achieve $\geq 360^o$ phase shift variation based on equations (3.1)- (3.4).
3. Full-wave simulation conducted to evaluate the performance of the phase shifter.
4. GCPW line routed under the dielectric slab within the assigned physical area to facilitate maximum physical length of the GCPW line within assigned area to maximize the achievable phase shift range (e.g., meander line or slow-wave line).
5. GCPW is modified under the dielectric slab to improve the impedance matching of the proposed phase shifter due to the effect of the dielectric slab's proximity to the GCPW line.
6. Prototype fabricated and measured to validate simulated results.

In order to provide a simple and fast design procedure to predict the phase response of the proposed phase shifter based on its physical dimensions and the actuation range, a simple empirical design formula was developed as part of this research. This formula can be used to calculate the required dielectric constant, the actuation range, and the length of the phase shifter that provides the required phase shifting range. Using the proposed design formula, designers can estimate the performance of the phase shifter with an error < 3% without using intensive full-wave simulations. The proposed formula has been developed based on perturbation theory following the work presented in [113]. By employing a curve fitting based on power series, the design formula in [113] is modified to predict the phase response as a function of the dielectric length, dielectric constant, operating frequency, and the airgap size. The phase shifter response $\Delta\varphi$ (L_s, ε_r, f, and h_{gap}) can be calculate based on equation (5.1).

$$\Delta\emptyset(Ls, \varepsilon r, f, hgap) = \frac{2\pi}{\lambda_g} L_s k \quad (5.1)$$

where

$$\lambda_g = \frac{\lambda_o}{\sqrt{\varepsilon_r}} \quad (5.2)$$

$$\lambda_o = \frac{c}{f} \quad (5.3)$$

$$k = \mathrm{d} + a h_{gap}^{b} \quad (5.4)$$

where $\Delta\phi$ in degrees is the phase response of the phase shifter, λ_g is the guided wave length inside the dielectric slab in mm, L_s is the length of the dielectric slab in mm, and k is the proportionality constant relating the gap size of the phase shifter with the realized phase shift. The guided wave length is calculated based on equations (5.2) and (5.3), where λ_o is the free space wave length (the ratio of the speed of light in mm/s to the operating frequency in GHz), and ε_r is the dielectric constant of the dielectric slab. The proportionality constant k can be calculated based on equation (3.4), using curve fitting to extract the constants (a, b, and d) by one full-wave simulation over four gap values. It was found that the exact values of these constants are a=-41.32, b=-0.1381, and d=43.1. The width and thickness of the dielectric slab were found to have minimal effects, as compared to those of its length (L_s) and dielectric constant (ε_r). Intensive full-wave simulations were conducted to evaluate the accuracy of the developed design formula for different design parameters. In these simulations the dielectric slab thickness was chosen to maximize the phase shift variation with minimum IL over the operating frequency (h_s =0.13λ_g), and the dielectric slab width was chosen to be 1 mm.

The dielectric slab's permittivity (ε_r) was varied between 40-100, and the length (L_s) was varied between 2-6 mm. The air gap between the dielectric slab and the GCPW line was varied between 1-10 μm, and the operating frequency was varied between 20-40 GHz. The simulated and calculated phase responses for different cases are shown in Figure 5.2. The empirical formula predicted the phase response of the proposed phase shifter versus gap for all abovementioned test cases accurately. The difference between the predicted phase responses from equation (5.1) and the full simulations are due to the small amount of the field leaked from the propagation channel.

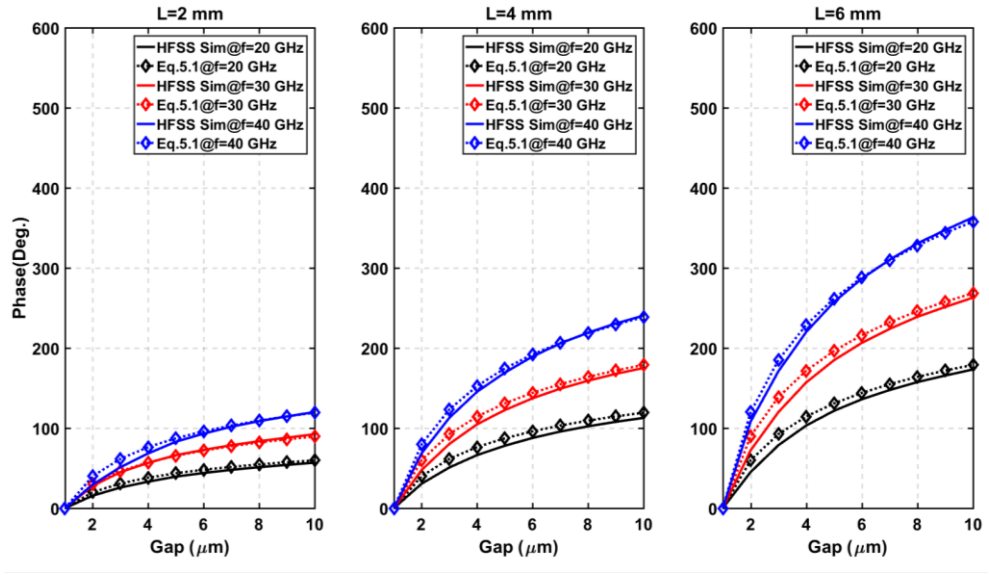
L=2 mm
L=4 mm
L=6 mm
HFSS Sim@f=20 GHz
Eq.5.1@f=20 GHz
HFSS Sim@f=30 GHz
Eq.5.1@f=30 GHz
HFSS Sim@f=40 GHz
Eq.5.1@f=40 GHz
Phase(Deg.)
Gap (μm)

(a)

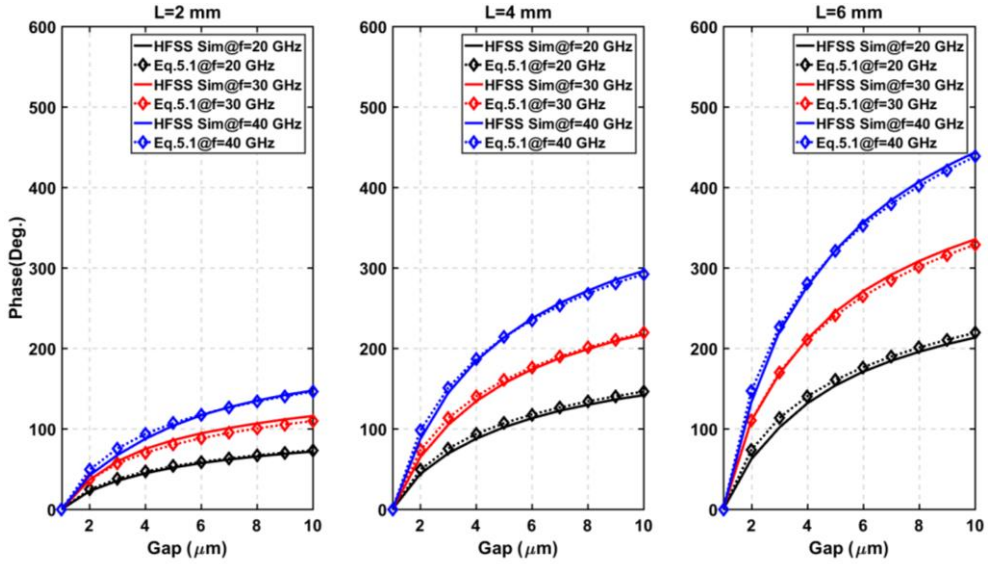
L=2 mm
L=4 mm
L=6 mm
HFSS Sim@f=20 GHz
Eq.5.1@f=20 GHz
HFSS Sim@f=30 GHz
Eq.5.1@f=30 GHz
HFSS Sim@f=40 GHz
Eq.5.1@f=40 GHz
Phase(Deg.)
Gap (μm)

(b)

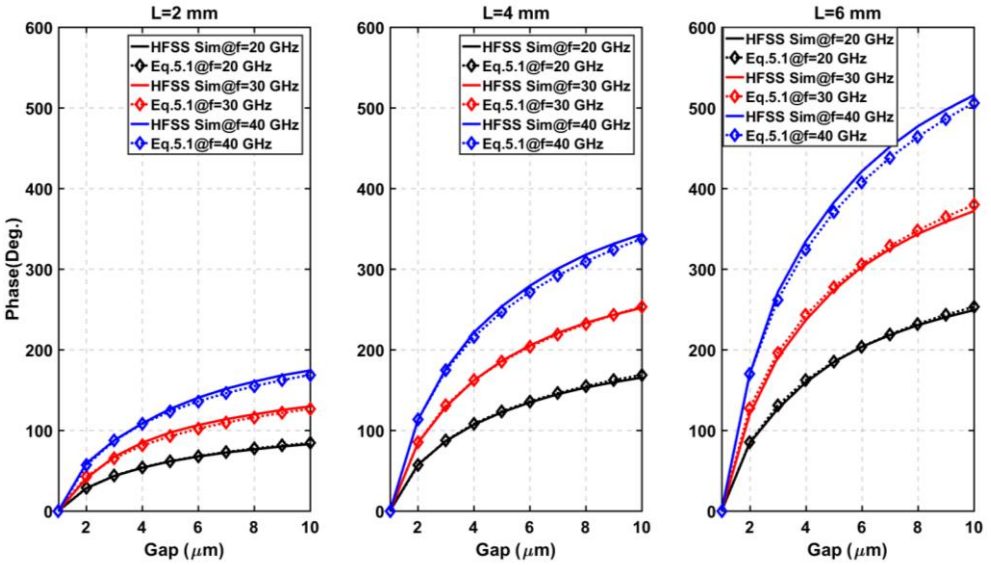

(c)

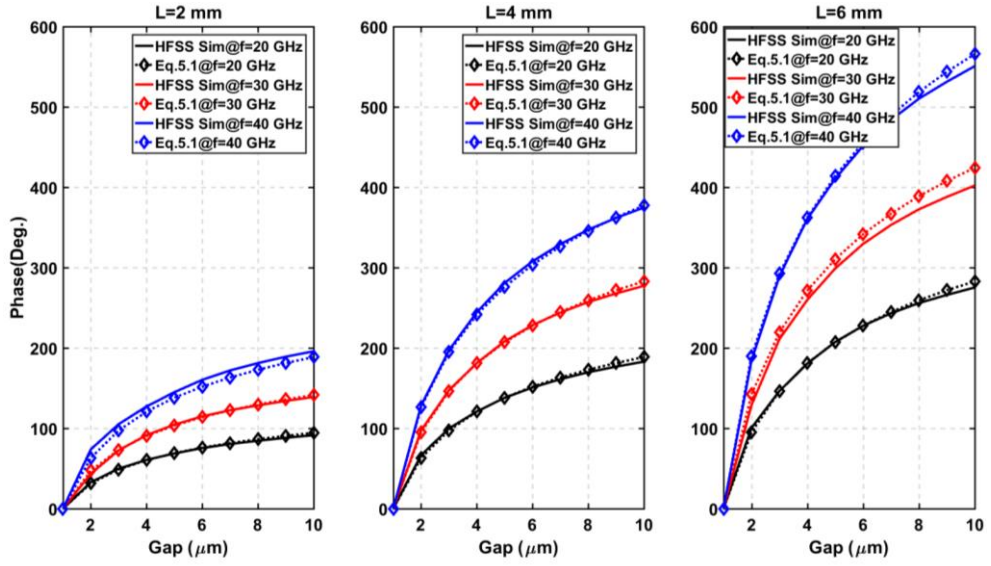

(d)

Figure 5.2: Simulated and calculated phase responses for different test cases: (a) ε_{rBLT}=40, (a) ε_{rBLT}=60, (a) ε_{rBLT}=80, and (a) ε_{rBLT}=100.

5.3 Meander line-based phase shifter I

A meander line-based GCPW line loaded with a high dielectric ceramic slab (ε_r=42) was developed as part of research to realize a wideband phase shifter. As a proof of concept, a PET was used to control the airgap height (h_{gap}). The GCPW line was designed on RT/duroid 6002, having a dielectric

permittivity ε_r=2.94, $\tan_\delta$=0.0012, and 35 μm copper thickness. The sidewalls of the substrate were plated to ensure an electrical connection between the top and bottom grounds of the GCPW line. The other advantage of using a low dielectric constant substrate in the proposed design is that it creates a high contrast between the GCPW substrate and the dielectric slab. This contrast makes the phase shift more sensitive to the air gap variation, thereby increasing the dynamic range of the phase shifter. The GCPW line was designed and optimized to operate over the required frequency band (19-31 GHz). The GCPW line can be divided into two parts, a 50 Ω GCPW line with a width of W_f and a spacing of S_1 at the input and output ports, and a middle phase shifting segment with a width of W_f and a gap of S_2. The space size (S_2) was optimized to achieve a low reflection coefficient over the operating frequency bands, overcoming the impedance mismatch in [116]. For the purpose of demonstration, the phase shifter was designed for two-way Ka-band satellite-communication (down link from19 GHz to 21 GHz and uplink from 28.5 to 30.50 GHz). No geometry scaling or matching/transition techniques are required over the entire tuning range in both operating frequency bands.

To house a full range phase shifter within a compact area (in the range of 2.1 mm × 3 mm), as is required for a Ka-band phased array with antenna footprint of about 5×5 mm^2, the GCPW line was designed in meander line configuration. This configuration achieves a longer physical length and; therefore, a larger phase shift within a smaller area ($W_p \times L_p$), and it can be easily fabricated with a low-cost fabrication process. The dielectric constant and the dimensions of the ceramic slab were chosen to optimize the size, dynamic range, and input and output RLes. For the sample design, a low-cost ceramic material was chosen with a dielectric constant of (ε_r=42), a low loss-tangent (0.005), high thermal stability, and low surface roughness. This material is an appropriate choice for high performance miniaturized phase shifters. The ceramic dielectric slab has a length of L_s, a width of W_s, and a thickness of h_s. The optimized design parameters of the proposed phase shifter are shown in Figure 5.3.

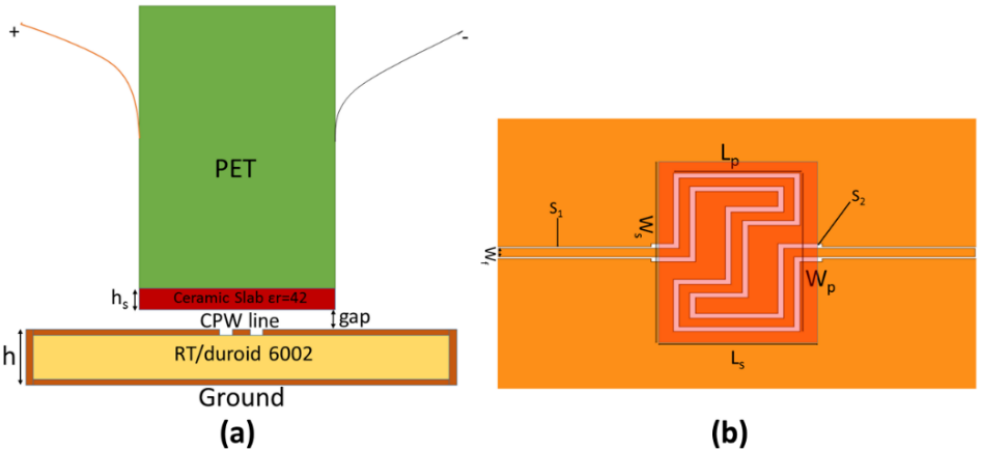

Figure 5.3: Proposed phase shifter structure labelled with design parameters: h= 0.5 mm, W_f=0.14 mm, S_1=0.03 mm, S_2=0.1 mm, L_p=1.7 mm, W_p=2.6 mm, L_s=2.1, W_s=3 mm, and h_s=0.2 mm.

5.3.1 Sensitivity analysis

Full-wave simulations were conducted to study the sensitivity of the proposed phase shifter, shown in **Figure 5.4**-**Figure 5.6**. A ±5% variation in the dielectric permittivity of the ceramic slab at 30 GHz, resulted in a ±3.2% variation of the maximum achievable phase variation. The proposed phase shifter shows a ±1.8% IL (S_{21}) variation and a ±1.5% frequency shift of RL (S_{11}). **Figure 5.4** illustrates the effect of the ceramic slab's dielectric permittivity variation on the phase and S-parameters.

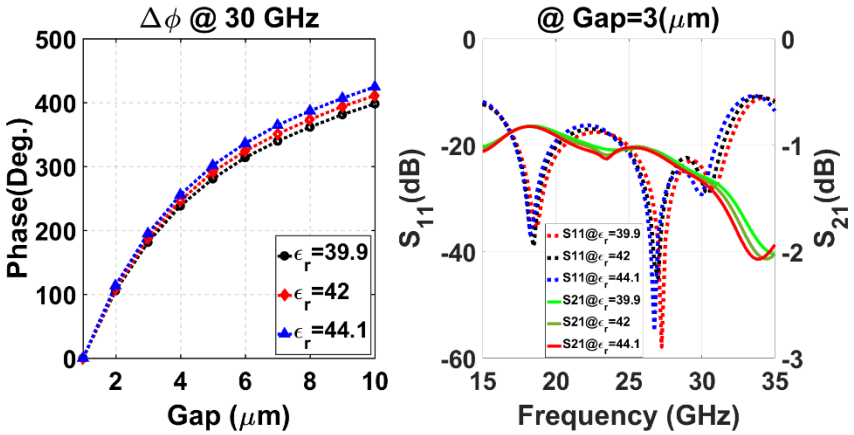

Figure 5.4: Effect of dielectric permittivity variation on phase and S-parameters.

Similarly, at 30 GHz a ±10% variation of the dielectric slab's thickness resulted in a ±1.6% variation of the maximum achievable phase variation and a ±2.7% S_{21} variation. Figure 5.5 depicts the effects of slab thickness variation on the phase and S-parameters.

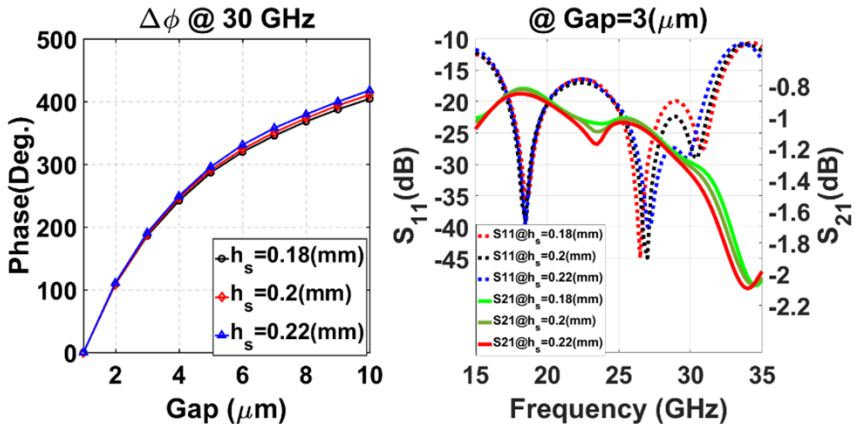

Figure 5.5: Effect of slab thickness variation on phase and S-parameters.

Furthermore, misalignment between the ceramic slab and the GCPW line appears to be the most critical case among other variations. A ± 100 µm (~±5%) misalignment between the BLT slab and the centre of the GCPW line (X and Y) leads to a 13% increase in the IL of the proposed phase shifter at 30 GHz with a small deterioration of the S_{11}. However, the maximum achievable phase shift is reduced by only 2°. Figure 5.6 shows the phase shifter performance with misalignment effect on both phase and S-parameters.

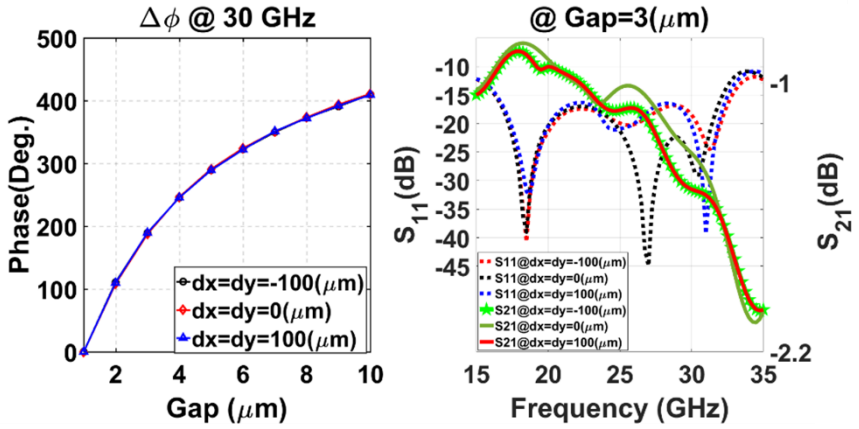

Figure 5.6: Phase shifter performance with misalignment effect on both phase and S-parameters.

PET tolerance variation directly affects the airgap range, in turn impact the accuracy of the phase shifter state. Surface roughness [116] is another important factor that limits the operation of the proposed phase shifter. However, an accurate surface model of the GCPW line and ceramic slab were not available for sensitivity analysis with respect to the surface roughness. Based on the sensitivity analyses, the proposed phase shifter demonstrated low sensitivity to the fabrication and material

tolerances. The IL was highly affected by the misalignment of the dielectric slab. On the other hand, the phase accuracy under room temperature conditions is limited mainly by the accuracy and repeatability of the actuator.

5.3.2 Fabrication process

The GCPW line was fabricated by using an LPKF laser machine and the sides were coated with copper to avoid parallel plate modes. Laser machining is a fast, low cost, chemical-free, and mask-free process that offers a very precise fabrication capability (accuracy better than 2 μm). Since laser fabrication is a non-contact process, the surface of the GCPW line is not damaged or scratched. The fabricated sample is shown in Figure 5.7a. A smooth surface is crucial for the proposed phase shifting mechanism. The power and the movement speeds of the laser beam were adjusted to etch the cladding copper completely while providing vertical walls for the traces. In addition to the GCPW line, the laser machine was also used to make high precision cuts on the ceramic dielectric slab. Since the amount of phase shift depends on the gap between the ceramic slab and the GCPW line, the surface roughness of both pieces has to be minimized. In particular, the first few microns of spacing exhibit the largest phase variation with respect to airgap height as shown in equation (5.1).

A potentially low cost and compact PET (AE0203D08F form NEC Cooperation) [126] was used to precisely change the airgap height between the GCPW line and the dielectric slab. This transducer generates a 0-9.1 μm continuous displacement by applying 0-150 V DC voltage to its poles. This amount of displacement is sufficient for the proposed phase shifter to achieve more than a 360° phase shift variation at 30 GHz. The PET is capable of moving lighter loads at frequencies of more than 10 kHz. In the proposed phase shifter, the PET can reach its nominal displacement within 30 μs. An aluminum fixture was designed and fabricated to hold the phase shifter substrate and to support the PET. The proposed phase shifter prototype structure including the aluminum fixture is demonstrated in **Figure 5.7**b.

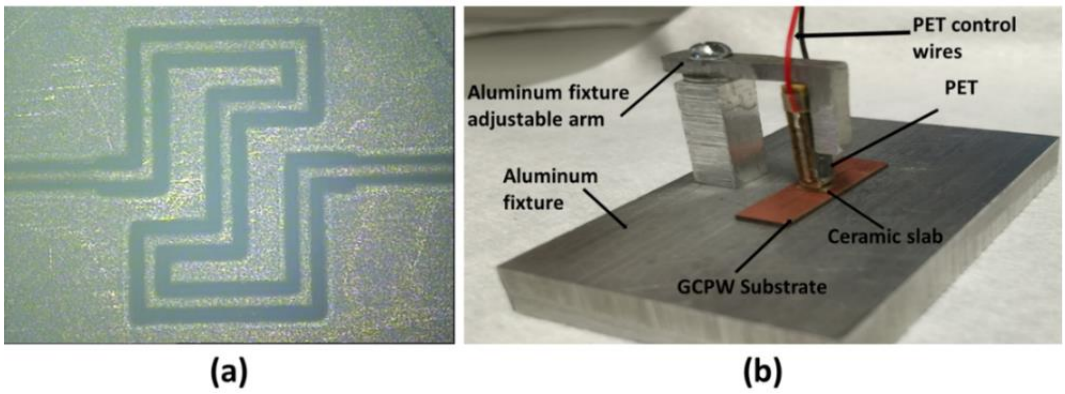

Figure 5.7: Fabricated GCPW line and system fixture.

5.3.3 Measurement and simulation results

The measurement setup is shown in Figure 5.8. it consists of a 50 GHz programable network analyzer (PNA)-X from Keysight Technologies, an aluminum fixture to support the GCPW substrate and the PET, a DC power supply from Keysight, and probes with 500 μm pitch. The assembly procedure was as the follows. First, the transducer was attached to the fixture arm and the height of the arm was adjusted through the adjusting screw to achieve the minimum gap between the GCPW substrate and the ceramic slab. In the second step, the GCPW substrate was fixed to the base of the fixture and centered underneath the PET. Then, a 100 V DC was applied to the PET to expand the transducer to its recommended maximum length. Finally, the ceramic slab was inserted between the PET and the phase shifter substrate and an adhesive material was used to fix the slab to the PET.

Extensive full-wave simulations were performed in order to optimize the dimensions of the GCPW line and the dielectric slab. The optimal design was fabricated and tested at room temperature. The measured S-parameters of the phase shifter over the downlink band when 35 V was applied to the PET are presented in **Figure 5.9**a. Measurements show a RL (S_{11}) < -20 dB with IL (S_{21}) > -0.66 dB over the frequency band. A good agreement between the experimental results and simulation results was observed. Similarly, Figure 5.9b shows a comparison between measurement and simulation results over the uplink band. The phase shifter exhibits an S_{11} < -13 dB with an average S_{21} > -2.38 dB over the uplink frequency band. There are some discrepancies between the measurement and simulation results. This is mainly due to slab misalignment with the GCPW line. However, the measurement results still match the simulation trends and are sufficiently accurate.

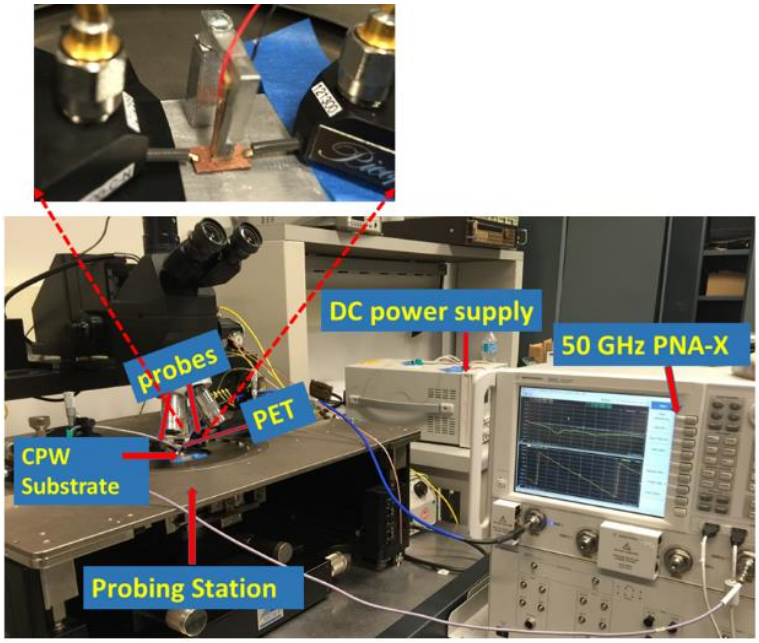

Figure 5.8: Phase shifter measurement setup.

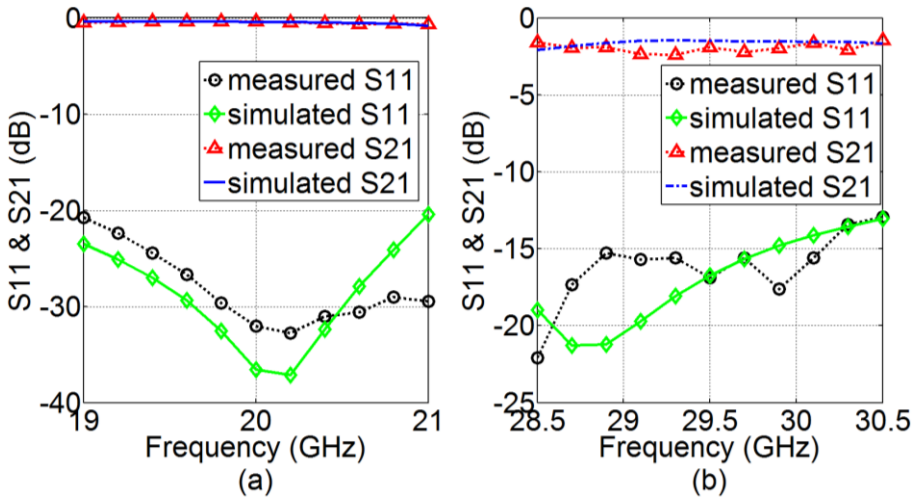

Figure 5.9: Comparison of measured and simulated S-parameters for phase shifter with control voltage 35 V.

Figure 5.10a and Figure 5.10b show the phase shift range (with respect to zero applied voltage) versus control voltage at 20 GHz and 30 GHz respectively. Good agreement between measurement and simulation results was observed over the whole range of the control voltage variation except for small discrepancies at a few points. These discrepancies are mainly due to the fact that in the simulations the control voltage was represented by its equivalent actuation displacement based on the

datasheet of the PET as well as to the misalignment between the ceramic slab and the GCPW line. The proposed phase shifter showed a 170° phase variation at 20 GHz and 270.5° at 30GHz. The realized phase variation was limited in this experiment due to the surface roughness of the ceramic slab and the PCB substrate, and by the limited actuation displacement ~ (0-7) μm when the applied voltage varied between 0-100 V.

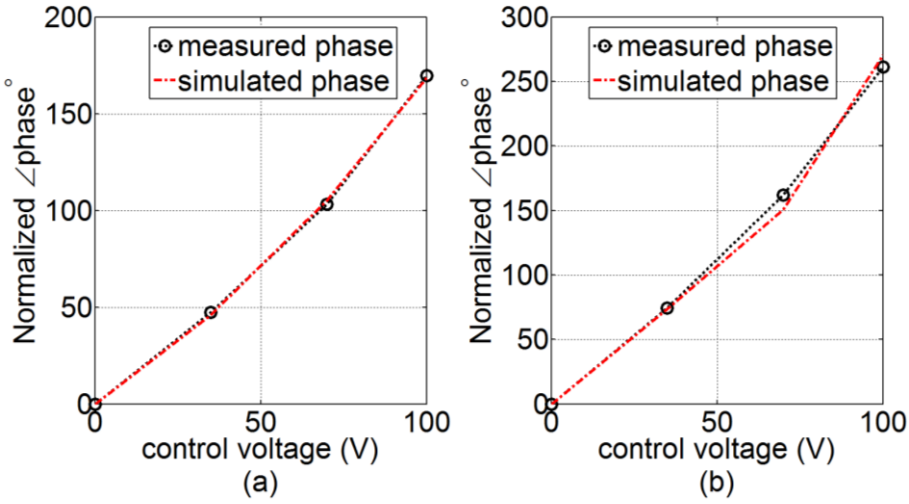

Figure 5.10: Comparison of phase delay versus control voltage measurement and simulation: (a) 20 GHz, (b) 30 GHz.

Figure 5.11a shows the measured S-parameters of the phase shifter over the downlink (20 GHz) band for different actuation voltages. An S_{11} < -17 dB with low average IL (S_{21}) ~ -0.53 dB and low average IL variation (ΔS_{21}) ± 0.22 dB was observed over the entire phase shift range, as shown in Fig. 11a. Furthermore, the measured average phase shift variation of 170° is achieved when the control voltage varies between 0-100 V at the downlink band, as shown in Figure 5.11b (phase state at 0 V considered as reference point).

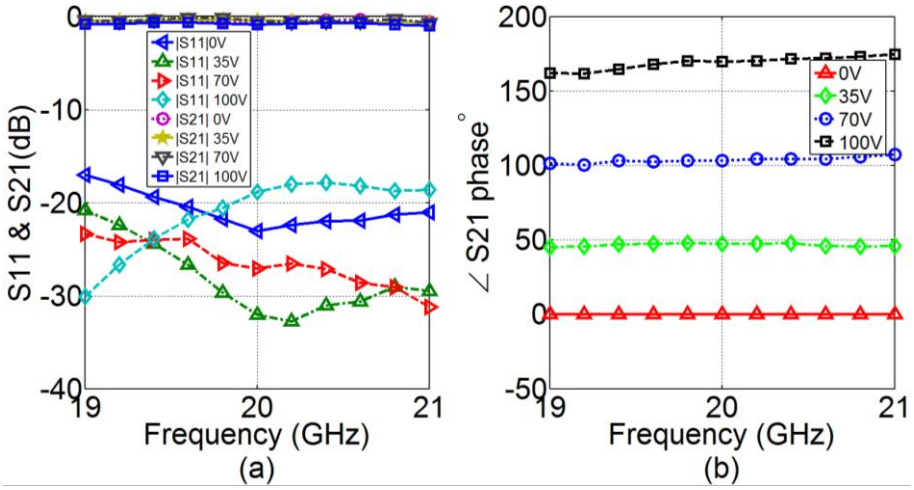

Figure 5.11: Downlink measurement results with different control voltages.

Similarly, the phase shifter was tested over the uplink frequency band (30 GHz) where it exhibited a good S_{11} of < -10 dB over the entire phase shift range, with an average S_{21}= -2.35 dB and average ΔS_{21} of < ± 0.35 dB over the frequency band, as shown in Figure 5.12a. Additionally, a measured average phase shift variation of 260̊ was achieved, when the control voltage varied between 0-100 V, as shown in. Figure 5.12b (phase state at 0 V considered as reference point).

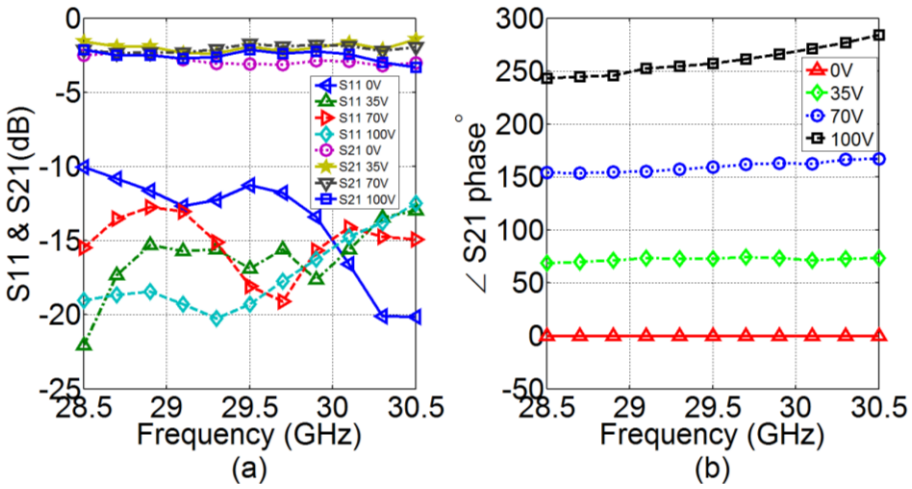

Figure 5.12: Uplink measurement results with different control voltages.

5.4 Phase shifter based on meander line and high dielectric constant slab

A larger phase shift can be achieved by increasing the length of the GCPW line ceramic slab, the height of the PET (to increase the dynamic range of the airgap height), and/or by using a higher

dielectric permittivity slab. The first two methods are not preferred for this particular application due to the size limitations. Accordingly, a high dielectric constant slab made of BLT (BaLn2Ti4O12) with a dielectric constant of ε_r=60 was used to improve the phase shifting range of the proposed phase shifter with the same GCPW line structure and the PET as in Section 3.3. This phase shifter prototype was designed and tested at the Ka-band frequency range 28-31 GHz. The operating frequency bandwidth of the following phase shifter prototypes are limited to Ka-band (28-31 GHz) since these phase shifters will be integrated with proposed CP antenna element that was introduced in Section 3.2. The GCPW line, was designed and fabricated on a low-cost substrate (RO4360G2); it has a dielectric constant of ε_r=6.15, and a dielectric loss $\tan_\delta$=0.0038, as shown in Figure 5.13. The GCPW line has a substrate thickness of h_1=0.203mm, width of W=16mm, and length of L=25.4mm. The 50 Ω GCPW line has a line width of W_f=0.28mm and a gap width of g_f=0.1mm. Step impedance matching was implemented by reducing the width of the GCPW line (W_f) under the dielectric slab from 2.8 mm to 0.11 mm in order to improve the input and output impedance matching. A tapered GCPW line transition was used at both the input and output of the phase shifter circuit to match the phase shifter line to the 2.9 mm RF coaxial connector to test the circuit easily with a PNA. Plated vias were utilized here to confine the propagated electromagnetic wave close to the slots; therefore, more perturbation can be achieved. A BLT dielectric slab with a dielectric constant of ε_r=60 and $\tan_\delta$=0.005 at 30 GHz was used in this prototype to increase the maximum phase shift. It has a width of W_{BLT}=3mm, a length of L_{BLT}=3mm, and a thickness of h_{BLT}=0.25mm. Furthermore, a PET of a size ($w \times l \times h$) =3×3×11mm^3, was used to vary the airgap h_{gap} from 2 μm to 11μm.

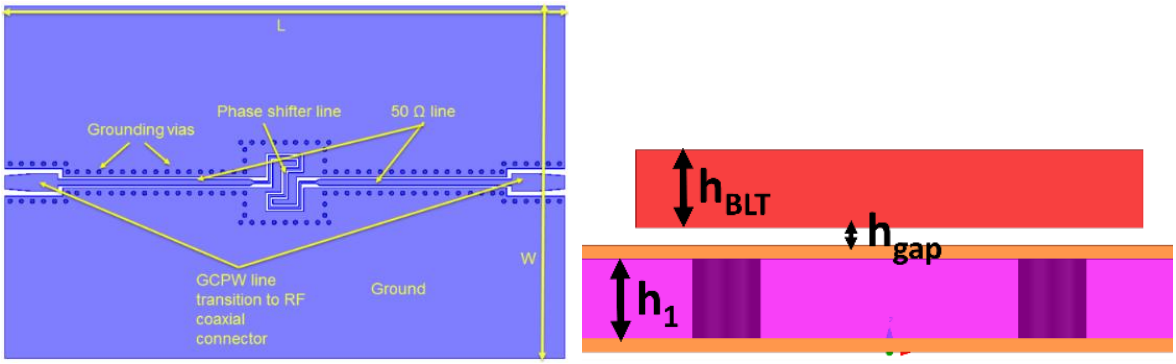

Figure 5.13: Phase shifter circuit.

5.4.1 Simulation results

A full-wave simulator was utilized when designing and optimizing the phase shifter circuit. Simulation results illustrate an $|S_{11}|$<-10 dB over the operating frequency band 28-31 GHz when the h_{gap} varies between 2µm to 11µm. Moreover, $|S_{21}|$ has an average of -1.25dB with ±0.75 dB variation. Simulated S-parameters are demonstrated in Figure 5.14. The maximum realized phase shift range was 400° with ±2° variation over the operating frequency band as depicted in Figure 5.15. As a result, the proposed phase shifter shows a very high FOM= 200°/dB. The FOM (Δ°/dB) is the ratio of the maximum phase shift achieved to the maximum IL of the phase shifter [111].

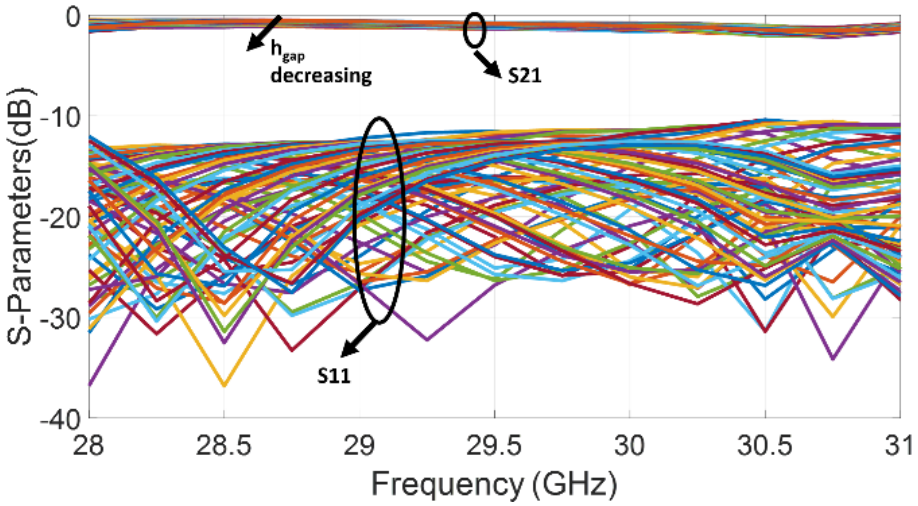

Figure 5.14: Simulated S-parameters (dB).

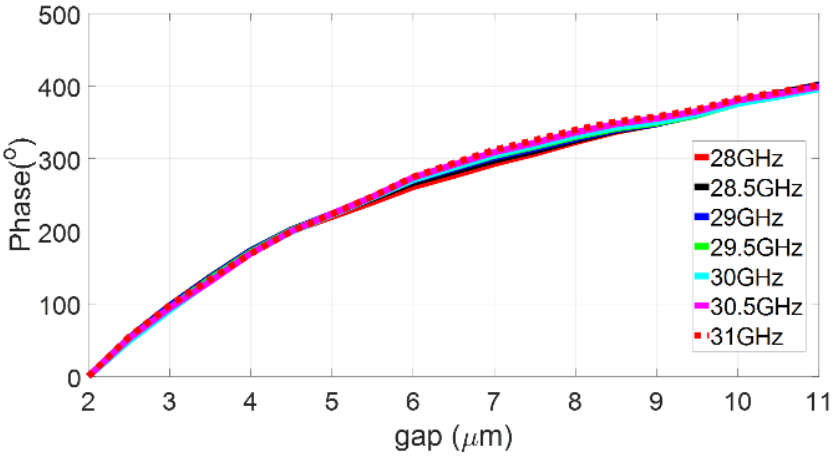

Figure 5.15: Simulated phase (Deg.).

5.4.2 Fabrication and experimental results

The fabricated GCPW line is shown in Figure 5.16. The proposed phase shifter was assembled and tested with a 50 GHz PNA from Keysight Technologies. The test setup is shown in Figure 5.17. An aluminum-based fixture is used to hold the PET over the GCPW line, and an adhesive material was used to attach the BLT slab to the PET.

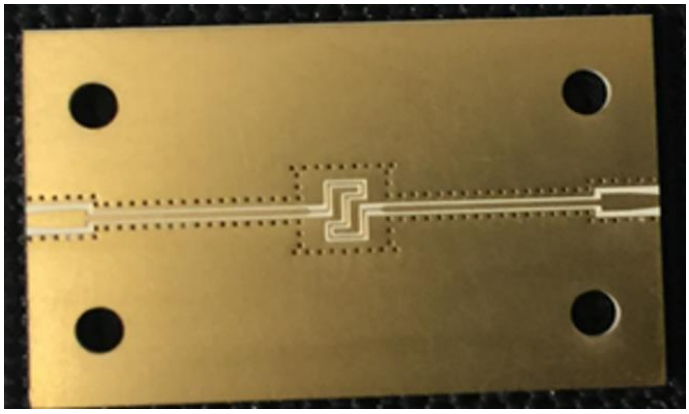

Figure 5.16: Fabricated GCPW line.

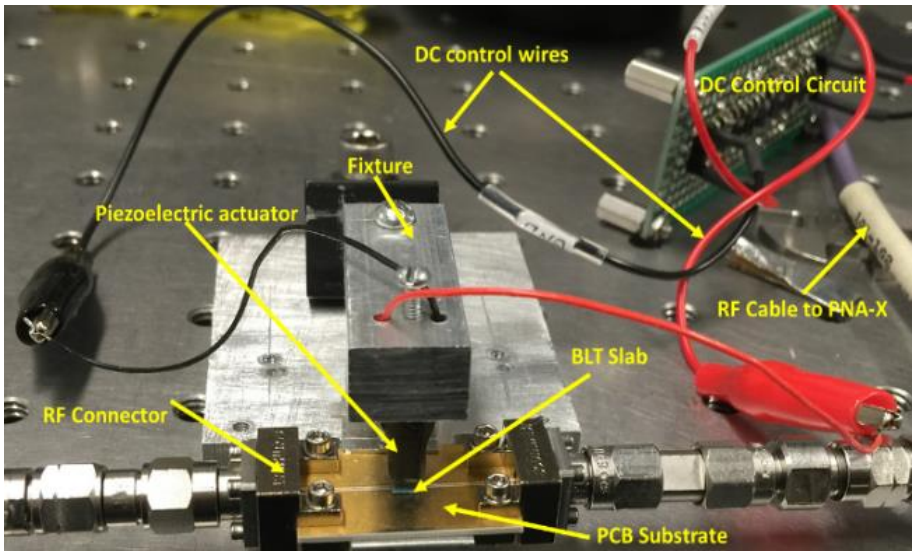

Figure 5.17: Phase shifter measurement setup.

The proposed phase shifter was tested over the frequency range 28-31 GHz. Measured S-parameters show good agreement with simulation results, as shown in Figure 5.18, except for some discrepancies (mainly due to misalignment between the BLT slab and GCPW line). However, the phase shifter demonstrated an $|S_{11}|$<-10 dB over the entire operating frequency band and an average

$|S_{21}|$=-1.5 dB with less than ±1 dB variation. Figure 5.19 illustrates the measured phase variation versus frequency as the applied voltage to the PET varies between 0V-150V (< 5° phase steps) to show that the proposed phase shifter capable to realize a fine phase resolution, which is a desired feature in high performance phased-array antenna applications. The maximum phase shift realized with this prototype was 306° and 365° at 28 GHz and 31 GHz, respectively, as shown in Figure 5.20. Accordingly, the realized FOM at 28 GHz and 31 GHz was 180°/dB and 146°/dB respectively. Such a high FOM proves the exceptional performance of the proposed phase shifting concept when compared to existing phase shifters operating at Ka-band frequencies.

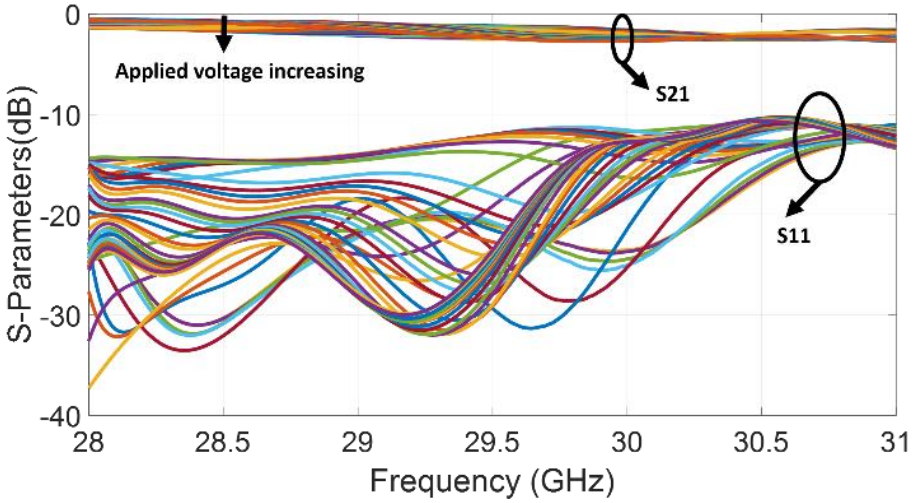

Figure 5.18: Measured S-parameters (dB).

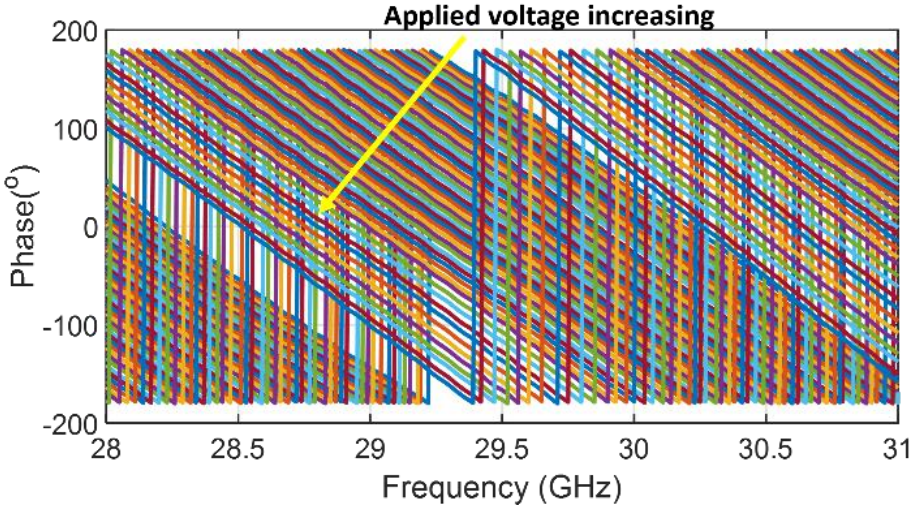

Figure 5.19: Measured phase response versus frequency with fine phase resolution.

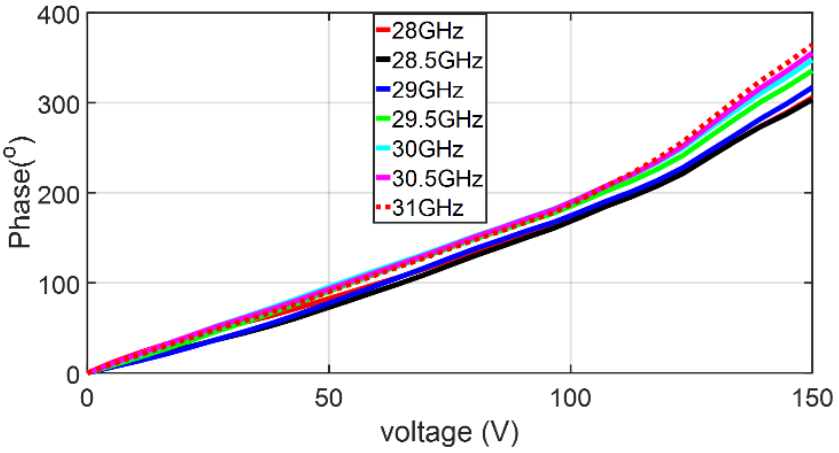

Figure 5.20: Measured phase response versus control voltage.

The phase shifter test was repeated several times with at least a one-hour interval between each consecutive measurement for different applied voltages under the room temperature condition. It was found that the phase shifter's S_{21} has a highly stable magnitude and phase over the operating frequency band. The S_{21} repeatability test shows a maximum absolute uncertainty of less than 0.045 dB in all cases, and the phase repeatability test shows a maximum absolute error of less than 0.3° in all cases as shown in Figure 5.21.

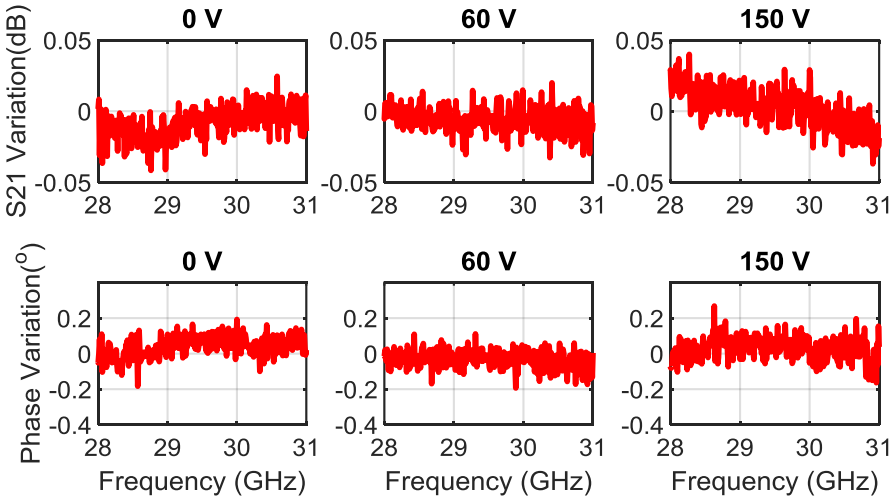

Figure 5.21: Repeatability test results.

5.5 Low-profile millimeter-wave phase shifter

5.5.1 Low-profile magnetic actuator

One of the most challenging aspects of loading a TL with a dielectric slab phase shifting concept, is the height of the actuator and the high driving voltage. Conventional actuation methods like PET are not the best options due to two drawbacks. First, the height of the PET usually increases linearly with the required displacement (e.g., a 10 μm displacement requires a PET with a height of 1 cm), making the phase shifter a bulky structure. Second, a typical PET requires a high DC control voltage (in the order of 100 V), which leads to a complex and costly implementation of the proposed phase shifter. To overcome these limitations, a high-performance, low-cost, and low-profile actuation mechanism was developed in CIARS. The proposed actuation mechanism consists of an integrated miniaturized permanent magnet made from materials with high magnetization such as samarium-cobalt (SmCo) and a planar magnetic coil. A magnetic actuation mechanism is seen as one of the best solutions to develop a low profile, low power consumption, and cost-effective solution to overcome the limitations of conventional actuation methods [127]. The proposed magnetic actuator utilizes the repulsion and attraction forces occurring between the permanent magnet and the planar magnetic coil to move the BLT slab with high precision and in the most repeatable manner. The BLT slab was attached to a flexible polyimide membrane supported by two beams to keep the BLT slab in its proper position during actuation. The polyimide membrane has a 50μm thickness, a beam width of W_b=200μm, a gap of G_b=200μm, a 2×4mm^2 base on which the BLT slab will be attached, and a 1.1mm opening to hold the SmCo magnet, as shown in Figure 5.22a. A very thin SmCo magnet (typically considered to have thicknesses and diameters <1 mm), was placed on top of the polyimide membrane. A tunable current source was employed to control the current of the magnetic coil thus generating an adjustable and reversible magnetic force. The magnetic coil was implemented on an FR4 PCB substrate with a spiral shape. A typical design has a line width of W_l=100μm, a gap between turns of G_l=50μm, and 14 turns, as shown in Figure 5.22b. According to Biot-Savart law, the magnetic field strength H(z) generated by the magnetic coil is given by [127]:

$$H(z) = \sum_{i=1}^{n} \frac{I[R+(i-1)G_l]}{\{[R+(i-1)G_l]^2+z^2\}^{3/2}} \quad (5.5)$$

Where z is the normal distance between the magnetic coil and the SmCo magnet, I is the supplied DC current passing through the planar coil, and R is the radius of the inner ring of the planar coil. The normal magnetic force generated can be obtained from basic Lorenz force equation [127]:

$$F_z = B_r A_{SmCo} \int_z^{z+h_{SmCo}} \frac{\partial H(z)}{\partial z} dz \qquad (5.6)$$

Where F_z is the normal magnetic force, B_r, A_{SmCo}, h_{SmCo} are the remanence, the area, and the height of the SmCo magnet respectively, and $\frac{\partial H(z)}{\partial z}$ is the gradient of the magnetic field generated by the magnetic coil. The normal displacement of the polyimide membrane is linearly dependent on the generated magnetic force, which can be calculated using the expression [127]:

$$d_z = c \frac{l_m^2 F_z}{h_m^2} \left(\frac{12\,(1-v^2)}{E h_m^2} \right) \qquad (5.7)$$

Where c is a constant depends on the boundary conditions of the outer edges and the membrane shape, l_m and h_m are the length and thickness of the polyimide membrane respectively, E is the Young's modulus of the polyimide material, and v is the Poisson's ratio.

A 3-D printed polymer-based structure was used as a low-cost package to support the components of the proposed phase shifter and provide protection against environmental effects. The total height of the new actuator and its 3-D packaging was less than 2mm, compared to a height of 12mm for the PET actuator used in Section (5.3 and 5.4). The proposed actuator required only ±40mA to elevate the BLT slab 50μm from the GCPW line surface; this is five times the displacement of a typical PET.

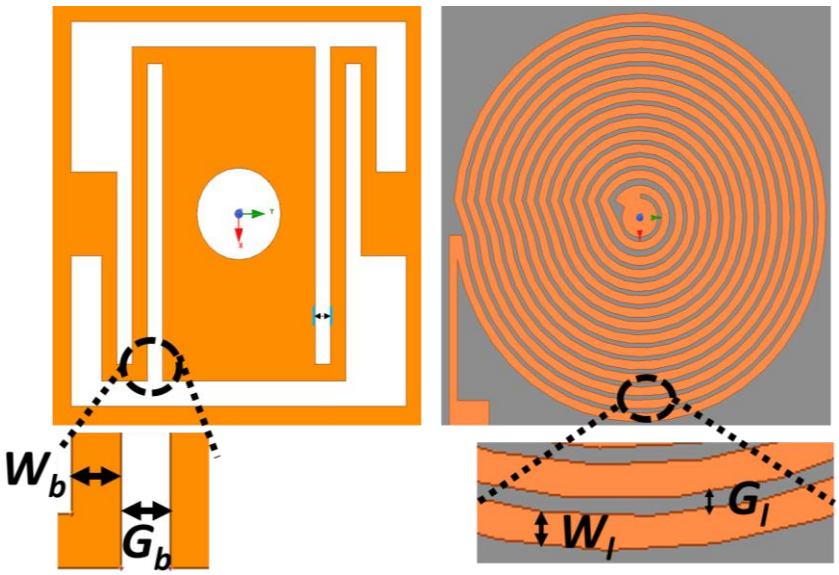

(a) (b)

Figure 5.22: Proposed polyimide membrane and planar electromagnetic coil: (a) top view of polyimide membrane, (b) top view of planar magnetic coil.

5.5.2 Phased shifter with magnetic actuator and 3-D printed packaging

Based on the new BLT phase-shifter concept, a new low-profile and high-performance phase shifter was designed and optimized in this research to overcome the height and power consumption drawbacks of the phase shifters presented in Sections (5.3 and 5.4). It consists of a straight GCPW line, a high dielectric slab, a magnetic actuator, and a 3-D printed packaging structure. The straight GCPW line was designed on a RO4360G2 dielectric substrate with an ε_r=6.15, a dielectric loss of $\tan_\delta$=0.0038, and a thickness of h_1=0.2032mm with a 50 Ω impedance at the input/output. The dielectric slab was BLT with a length of L_{BLT}=4 mm, a width of W_{BLT}=1.5 mm, a height of h_{BLT}=0.2 mm, an ε_r=100, and a dielectric loss of $\tan_\delta$=0.01 [116]. The BLT slab was placed on top of the GCPW line, and the magnetic actuator was utilized to control its position. This allows a tunable and continuous phase to be realized. An exploded view of this phase shifter is shown in **Figure 5.23**.

5.5.3 Simulation results

The GCPW line, shown in **Figure 5.24**, has a line width of W_{f1}= 0.28mm and a gap size of S_f =0.11mm at the input and output of the phase shifter. The existence of the BLT slab reduces the GCPW line impedance, so impedance matching is introduced on the GCPW part below the BLT slab. Impedance matching was realized by decreasing the width of the GCPW line from 0.28mm to W_{f2} =0.11mm; therefore, the proposed phase shifter shows a RL of <-10 dB for all phase states over the operating frequency band.

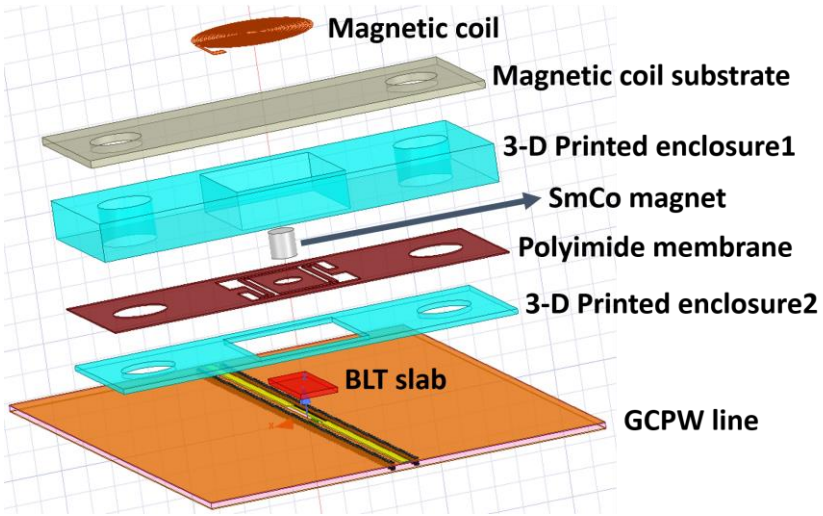

Figure 5.23: Exploded 3-D view of phase shifter with magnetic actuator and 3-D printed enclosure.

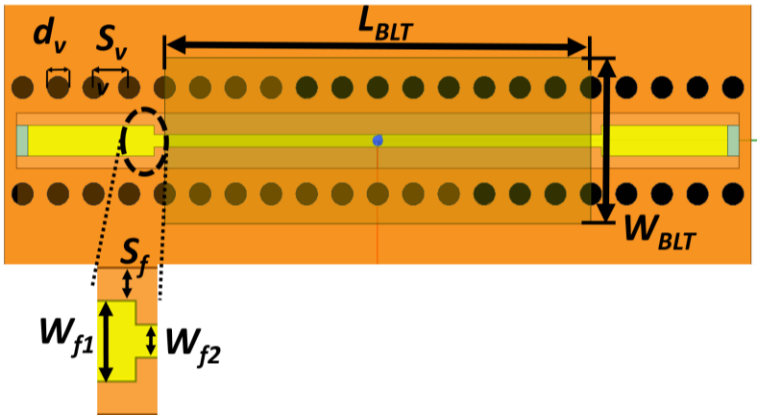

Figure 5.24: Proposed phase shifter circuit top view.

The proposed phase shifter architecture has a wide operating bandwidth as was demonstrated in [116-117]; however, this prototype was designed and tested over the operating frequency band (i.e., 29-31 GHz centered at 30 GHz), and its optimized dimensions are listed in **Table 5.1**.

Table 5.1: Optimized parameters of phase shifter (mm)

Parameter	W_{f1}	S_f	L_{BLT}	W_{BLT}	h_{BLT}
Dimension	0.28	0.11	4	1.5	0.2
Parameter	W_{f2}	d_v	S_v	h_1	
Dimension	0.11	0.203	0.5	0.203	

Simulations were performed to optimize the phase shifter and to calculate the actuation height required to realize a >360° phase shift. Simulations showed that to realize such a phase shift, the airgap h_{gap} should vary between 1μm and 45μm as shown in **Figure 5.25**a. A small h_{gap} contributes more significantly to the phase shift than a larger gap. Moreover, the proposed phase shifter demonstrated a $|S_{11}|$ <-10 dB over the operating frequency band (29-31 GHz) for all h_{gap} values. Similarly, it achieved a very low $|S_{21}|$ for the same frequency bandwidth. The simulation results showed an average $|S_{21}|$ of -0.95 dB at 30 GHz with an exceptionally low $|S_{21}|$ variation of less than ±0.5 dB over the entire range of phase shift. The simulated S-parameters are shown in **Figure 5.25**b.

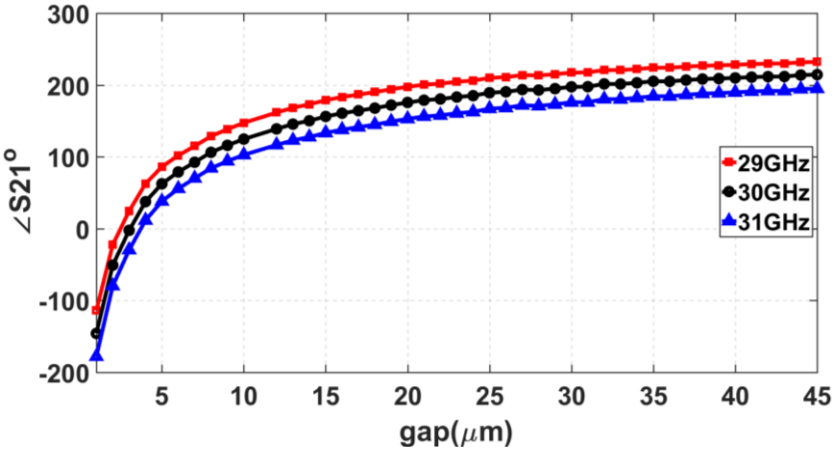

(a)

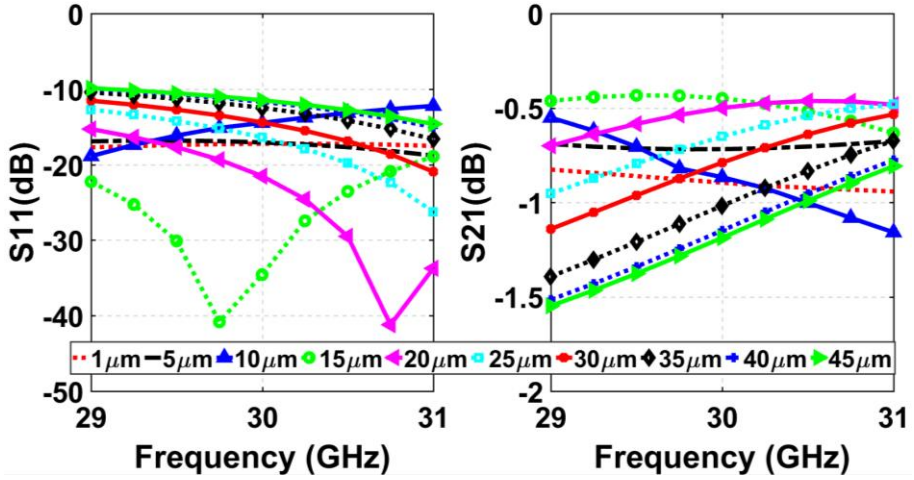

(b)

Figure 5.25: Simulated results for proposed phase shifter for different h_{gap}: (a) phase versus h_{gap}; (b) S-parameters versus frequency.

5.5.4 Measurement results

The proposed phase shifter was fabricated and tested using a PNA from Keysight Technologies. Measurements were taken over the frequency band 29-31 GHz. **Figure 5.26** shows the fabricated phase shifter. S-parameter measurements of the proposed phase shifter demonstrated linear phase-frequency behavior with a maximum phase shift of 285° at 30 GHz when a 100-mA was applied to the magnetic actuator. The fact that the power consumption during the experiment was higher than the theoretical value is mainly due to the extra losses introduced by the interconnecting DC power lines between the magnetic coil and the current source. However, this extra power consumption can be easily eliminated by integrating the current source on top of the magnetic coil. Moreover, the

proposed phase shifter was designed to achieve a 360° phase shift at 30 GHz, but measurements showed a maximum phase shift of 285°, as illustrated in **Figure 5.27**a. This discrepancy occurred because during simulation it was assumed that the airgap height h_{gap} could be reduced to 1μm in order to realize the required 360° phase shift. This was not possible to achieve with the fabricated prototype mainly due to the surface roughness of the fabricated GCPW line.

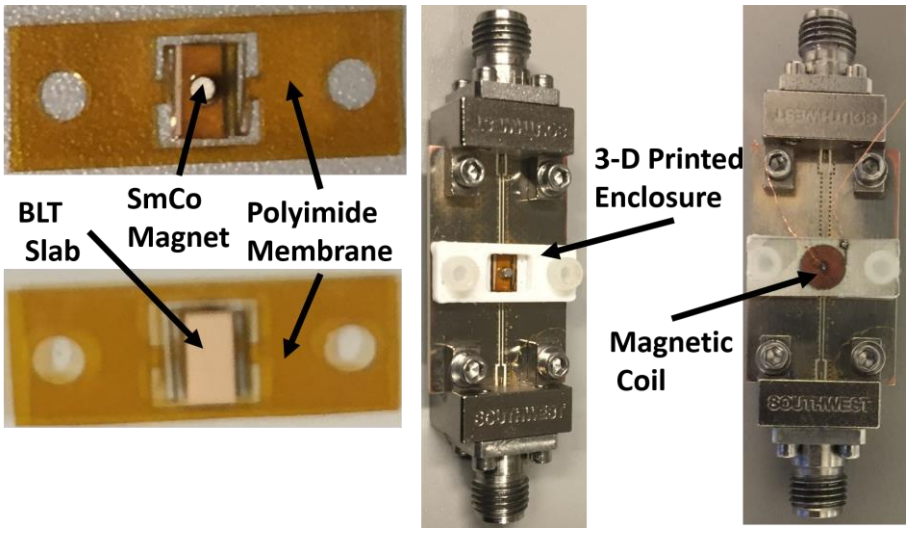

Figure 5.26: Fabricated phase shifter circuit and actuator components.

Measurement results indicate an $|S_{11}|$ <-10 dB over the operating frequency bandwidth for different h_{gap} states, meaning the measured $|S_{11}|$ is quite similar to the simulated result. In addition, the measurements demonstrate very low $|S_{21}|$ especially at 30 GHz. They show an average $|S_{21}|$ of -1 dB with an extremely low measured $|S_{21}|$ variation of ±0.2 dB around the center frequency (30 GHz). The measured $|S_{21}|$ is one of the best reported to date in the literature [See **Table 5.3**]. **Figure 5.27**b presents the measured S-parameters versus frequency for the proposed phase shifter at different applied current states. **Table 5.3** compares the performance of the phase shifter presented here with state-of-the-art phase shifters that use similar phase shifting mechanisms.

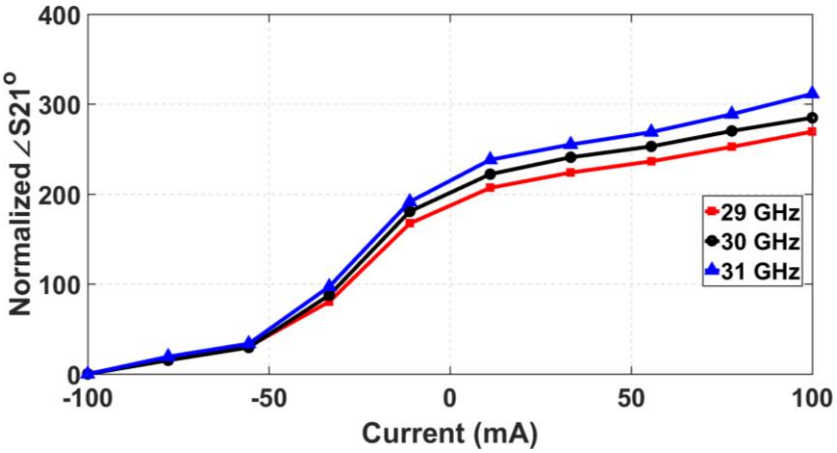

(a)

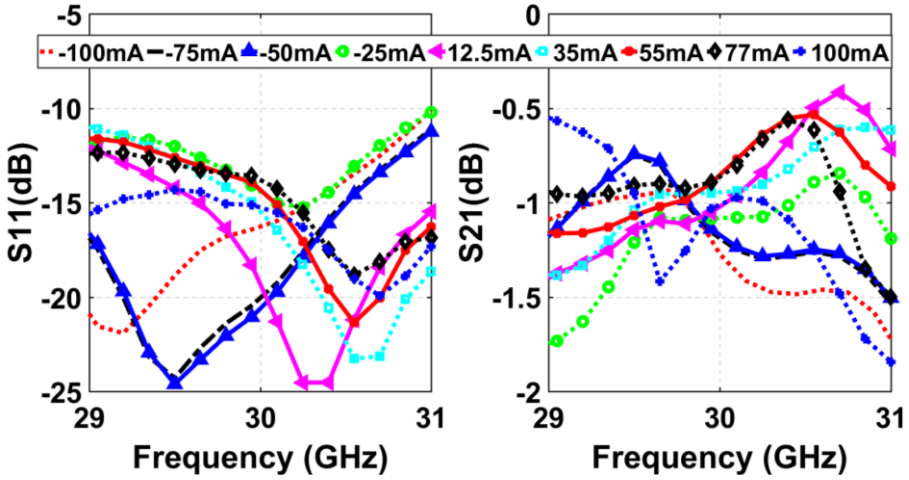

(b)

Figure 5.27: Measured results for proposed phase shifter with different applied currents: (a) normalized phase versus applied current; (b) S-parameters versus frequency.

5.6 A Slow-wave based GCPW line phase shifter

To increase the phase shifting range of the proposed low-profile phase shifter (Section 5.5), a slow-wave (SW-GCPW) line was incorporated into the phase shifter design to realize a longer electrical length within a relatively small physical length. A BLT slab (ε_r =100) was placed on top of the proposed SW-GCPW line to tune the phase. The proposed structure employs the same actuation and packaging structures as those presented in Section (5.5).

5.6.1 SW-GCPW line

A periodic structure is used to generate a slow electromagnetic wave in a guiding medium; thereby, it can be used to increase the electrical length of a TL within the same physical length [128]. In this research a periodic capacitive loading of a GCPW line was used to create an SW structure as a method to reduce the length of the proposed phase shifter. The top view of the proposed SW-GCPW is shown in **Figure 5.28**. RO4360G2 (ε_r*=6.15*, tan_δ*=0.0038*, and thickness *h=0.203 mm*) was used as a dielectric substrate to design the proposed SW-GCPW line. The signal and ground of the CPW line was modified to create a comb shape to realize a capacitive loading, leading to a change in the phase velocity of the propagating guided mode. The periodicity (*P*) of loading was chosen to be 0.4 mm and the width of the comb fingers was chosen to be W_1*=1 mm*. The SW-GCPW was tapered at the input and output with two-step impedances that have widths of W_2*=0.8 mm* and W_3*=0.6 mm* respectively, to improve the impedance matching of the proposed GCPW line over the operating frequency band (20-30 GHz). The input and output of the SW-GCPW line were connected to a 50 Ω GCPW line (line width of W_{f1}*=0.28mm* and gap width of *S=0.11 mm)*. Fencing vias with a diameter of d_v*=0.203 mm* and a spacing between vias of S_v*=0.403 mm*, were utilized to connect the top and bottom grounds. **Table 5.2** shows the parameters of the proposed SW-GCPW line that was optimized by employing a full-wave simulator from ANSYS. Simulations showed that the proposed SW-GCPW line exhibits an IL $|S_{21}|$ comparable to the conventional GCPW line. The conventional line had the same physical length and a RL $|S_{11}|$ better than -20 dB over the operating frequency band as shown in **Figure 5.29** (top). Furthermore, in the modified SW-GCPW, a 1.7 times delay enhancement was achieved as compared to the conventional GCPW as illustrated in **Figure 5.29** (bottom).

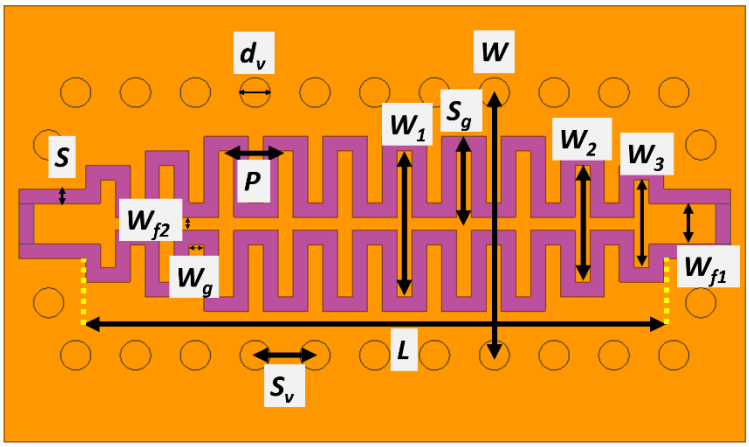

Figure 5.28: Top view of proposed SW-GCPW line.

Table 5.2: Dimensions of proposed SW-GCPW line (mm).

parameter	L	P	W_1	W_2	W_3	W_{f1}	S
dimension	*3.6*	*0.4*	*1*	*0.8*	*0.6*	*0.28*	*0.11*
parameter	W	L_{s2}	W_{f1}	W_{f2}	d_v	S_v	h_1
dimension	*1.5*	*2.42*	*0.28*	*0.1*	0.203	*0.403*	0.203

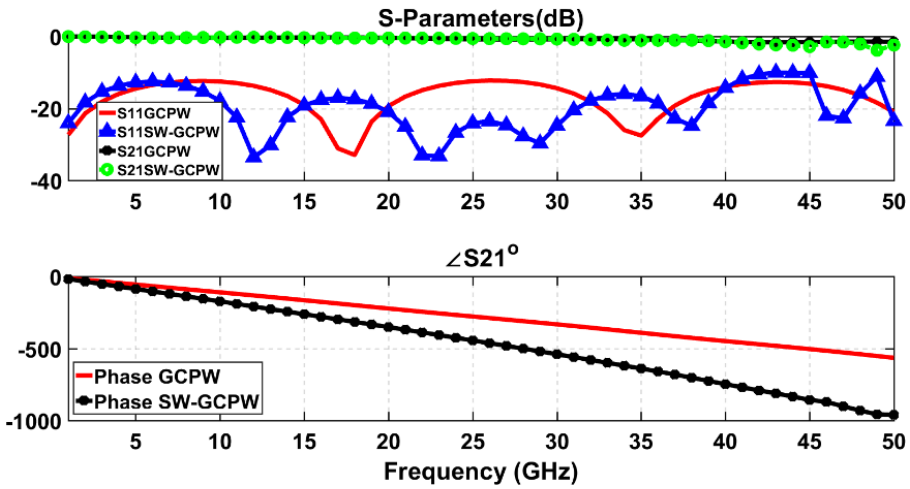

Figure 5.29: Simulation results for GCPW line and proposed SW-GCPW line: (top) S-parameters (dB); (bottom) phase of the S_{21} (Deg.).

5.6.2 Phase shifter circuit and simulation results

The BLT slab had a dielectric constant of ε_r =100 and loss tangent of $\tan_\delta$=0.01. The BLT dimensions were (length) L_{BLT}=3.6 mm, (width) W_{BLT}=2 mm, and (thickness) h_{BLT}=0.2 mm. With these dimensions, a variable airgap h_{gap} (spacing between the BLT and the GCPW line) of between 1 μm to 50 μm is needed to obtain more than 360° phase shift at 30 GHz. The top and side views of the proposed phase shifter are shown in **(a)** (b)

Figure 5.30. The proposed phase shifter was simulated over the frequency range 28.5-30.5 GHz. For practical considerations, the airgap height (h_{gap}) was varied over the range of 4-54 μm. To demonstrate the advantage of the proposed SW-GCPW over the conventional GCPW line, a similar phase shifter structure with the SW was replaced by a conventional GCPW line was designed and simulated. As can be seen in Figure **5.31**, the SW-GCPW based phase shifter exhibits a phase shifting range of 0°-313° at 29.5 GHz—almost twice of that is realized by the GCPW based phase shifter (0°-

162°) at the same operating frequency. The simulated S-parameters of the proposed phase shifter are plotted in **(a)** (b)

Figure 5.32. The simulated RL $|S_{11}|$ was better than -10 dB over the operating frequency for all h_{gap} values except in one case at 28.5 GHz. The maximum IL $|S_{21}|$ of -1.7 dB appeared at 28.5 GHz when h_{gap} was set to 4 µm; the best $|S_{21}|$ (-0.9 dB) was achieved at the same frequency when h_{gap} was set to 54 µm. The proposed phase shifter shows a very high FOM with the worst case of 173.4°/dB at 28.5 GHz due to impedance mismatch; the best simulated FOM of 240.6°/dB was realized at 30 GHz.

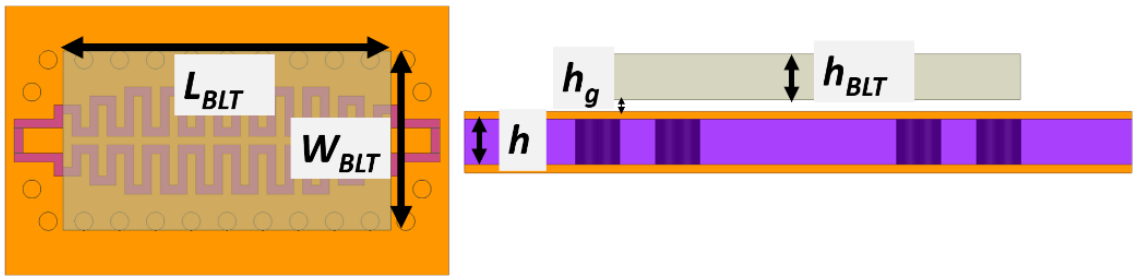

(a) (b)

Figure 5.30: Proposed phase shifter circuit (a) top view, (b) side view.

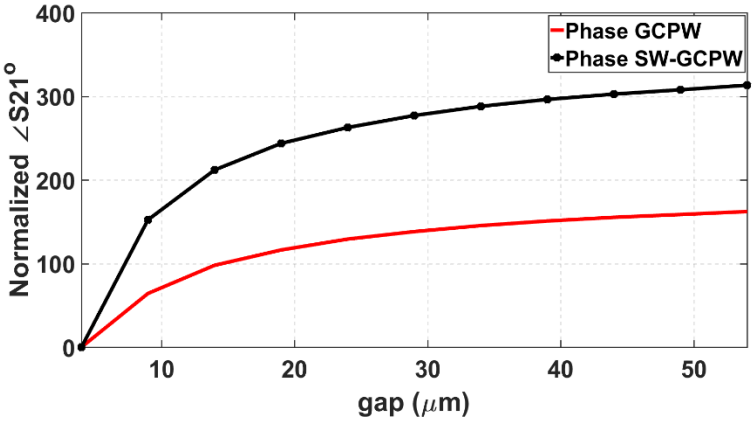

Figure 5.31: Simulated phase responses for GCPW and proposed SW-GCPW-based phase shifters at 29.5 GHz.

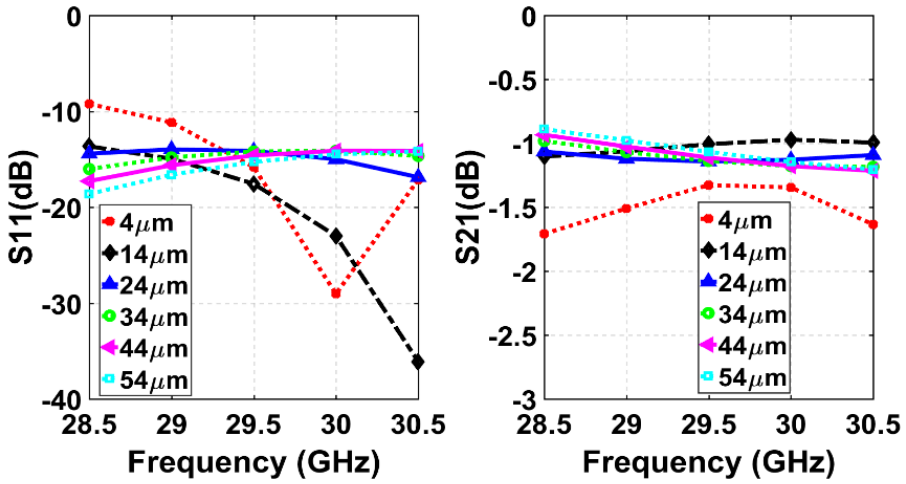

(a) (b)

Figure 5.32: Simulation results for proposed phase shifter with different h_{gap} heights (a) S_{11} (dB), (b) S_{21} (dB).

The proposed actuator in packaged form exhibits < 2 mm height, making it an excellent candidate to be utilized in such a phase shifting mechanism. The cross section of the new phase shifter is illustrated in **Figure 5.33**.

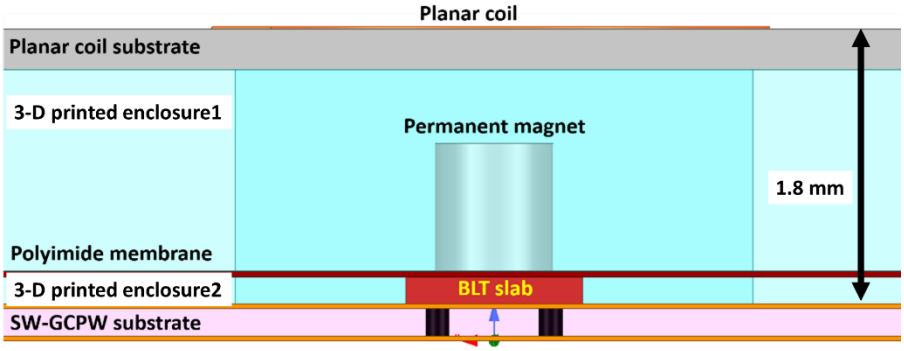

Figure 5.33: Cross-section of the new low-profile magnetically actuated BLT phase shifter.

5.6.3 Fabricated phase shifter prototype and measurement results

The components of the proposed phase shifter were fabricated and assembled. A Keysight PNA-X was employed to measure its characteristics. The fabricated phase shifter and its characterization setup are shown in **Figure 5.34**. Measurements were performed over the operating frequency band (28.5-30.5 GHz). The current of the planar magnetic coil was varied from 0-260 mA, to ensure an

attractive magnetic force between the planar magnetic coil and the permanent magnet was generated. As a result, a tunable phase shift was realized.

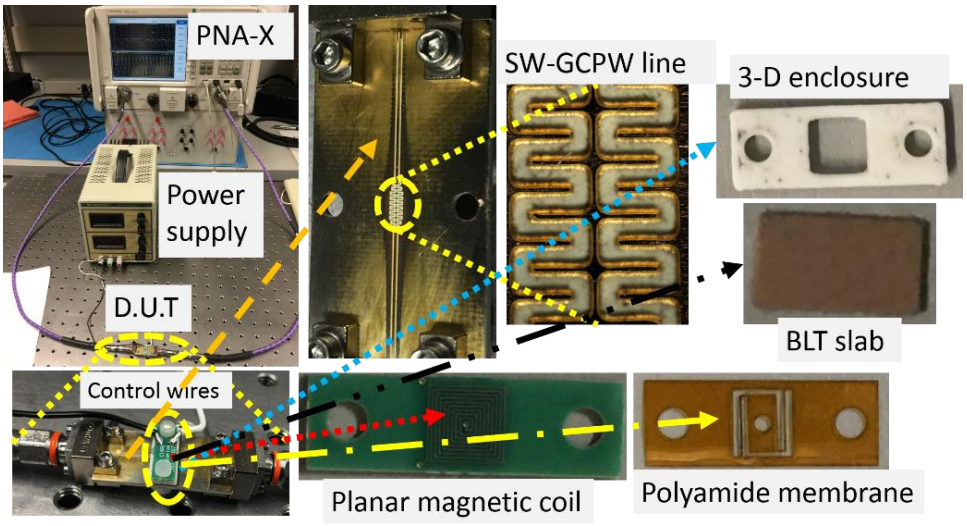

Figure 5.34: Fabricated phase shifter circuit and its measurement setup.

The measured normalized phase response of the proposed phase shifter is shown in **Figure 5.35**. As can be seen, the SW-GCPW based phase shifter exhibits a measured phase shifting range of 0°-311° at 29.5 GHz, which matches the simulated results. The measured $|S_{11}|$ and $|S_{21}|$ of the proposed phase shifter are depicted in **Figure 5.36**. The measured $|S_{11}|$ was better than -10 dB over the operating frequency for all phase shift states. The maximum $|S_{21}|$ of -1.65 dB was observed at 29.5 GHz when the current was set to 0 mA; the best $|S_{21}|$ (-1.05 dB) was achieved at the same frequency when the current was set to 260 mA, corresponding to a large h_{gap}. As a result, the proposed phase shifter shows a very high FOM of 188.5°/dB at 29.5 GHz.

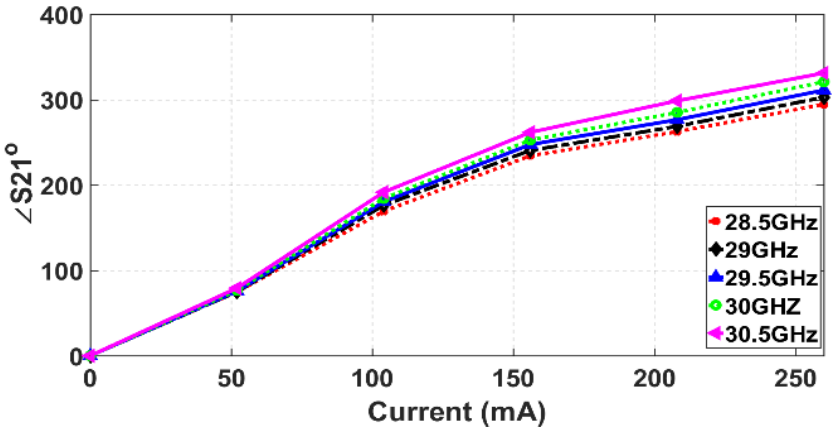

Figure 5.35: Measured normalized phase response of new phase shifter.

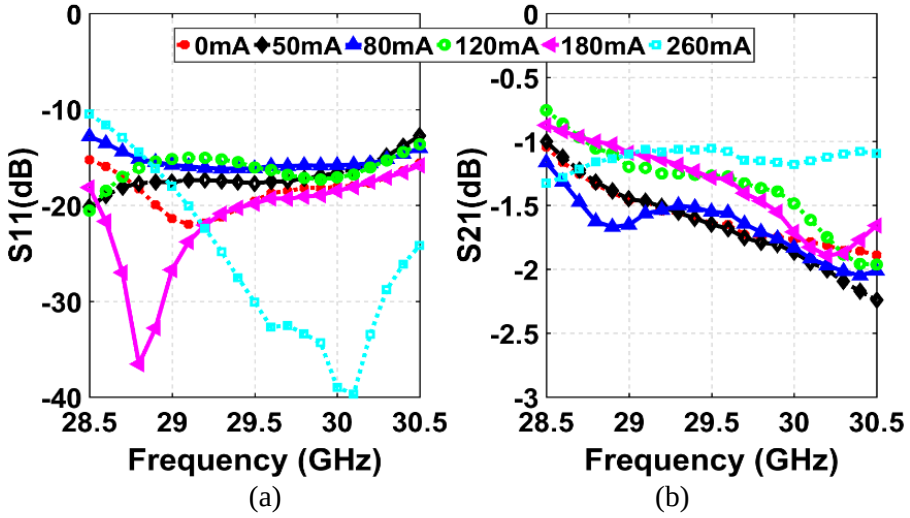

Figure 5.36: Measured results for new phase shifter with different current values: (a) S_{11} (dB), (b) S_{21} (dB) for different current values.

5.7 Summary of the results and conclusions

In this chapter, design, and optimization of a high-performance phase shifter structure based on new BLT phase-shifting technology was reported. The new phase-shifter was implemented in a low-cost standard two-layer PCB technology and extensively tested and characterized. The new phase shifter enables the realization of a low-cost mm-W passive phased array as will be presented in chapter 6—a structure in high demand for numerous emerging mm-W applications.

The new phase shifter demonstrated a continuous monotonic linear phase-gap response. It operates over a wide frequency range with high FOM and excellent RL $|S_{11}|$ and IL $|S_{21}|$ performance over the entire range of the phase shift. The phase-shifter uses a new low-profile, low cost, and low power consumption actuating mechanism. The new actuation mechanism, based on magnetic force, has overcome the limitations of other actuation mechanisms for such high-performance phase shifting [95 and 113-117]. A comparison of the proposed phase shifter with state-of-the-art phase shifters developed by other technologies is shown in **Table 5.3**. The proposed phase shifter shows a better performance compared to state-of-the-art devices as it realized a higher FOM with lower power consumption.

Table 5.3: Comparison of state-of-the-art continuous-type phase shifters.

Ref.	[99]	[109]	[108]	[113]	[115]	This work	This work
Material	MEMS	LC	Ferroelectric	Low dielectric perturber	Magneto dielectric perturber	GCPW Section 5.5	SWGCPW Section 5.6
f (GHz)	75	30	32	9.7	20	30	29.5
$\Delta\emptyset_{max}$ (°)	32	60	372.3	132	384	285	311
$\lvert IL_{max}\rvert$ (dB)	5	6	7.3	2.31	4.5	**1.20**	**1.65**
FOM $\Delta\emptyset_{max}/\lvert IL_{max}\rvert$	6.4	10	51	57	85.3	**237.5**	**188.5**
Area (mm2)	6x30	14.6x5	1x1.2	73x32	12x4	2x4	2x3.6
Voltage (dc)	0-40	0-100	0-30	0-100	0-50	**0.1Vx(±0.1A)**	**0.1Vx0.26A**

Chapter 6

A Low-cost Ka-band Passive and Steerable Antenna Array

6.1 Introduction

This chapter investigates enabling technologies, and develop a proof-of-concept prototype, for a low-cost and low-profile compact steerable passive antenna array concept for mm-W applications (Ka-band systems specifically). First, the phase shifter presented in Section 5.2 is integrated with the novel CP antenna element introduced in Section 3.2 to develop a proof-of-concept 1×4 Ka-band CP passive PAA. First, the CP antenna elements are loaded with a right triangle-shaped BLT slab, and a mechanical actuator is used to control the air gap height as a simple conventional passive PAA. Its beam was steered over the scanning range of 0^o- 25^o at 30 GHz, when the air gap between the slab and the TLs was varied from 60μm to 8μm. A more sophisticated passive PAA with low-profile is then developed by employing the magnetic actuation mechanism presented in Section 5.5. The realized passive PAA radiates a CP pattern and is steered up to ±38^o off-boresight with high radiation efficiency (~ 60% at 30 GHz). Finally, the phase shifting mechanism was utilized to develop a novel wideband mm-W reconfigurable RAA element with 360^o reflection phase as an excellent building block for a large-scale steerable mm-W RAAs.

6.2 CP passive PAA with micro-positioner

As a proof-of-concept, a 1×4 CP sub-array was developed to operate at 30 GHz in order to steer the beam to different angles. As shown in Figure **6.1**, the systems consists of four CP antenna elements with 5 mm inter element spacing; a BLT right triangle slab with ε_r=100 and dimensions of L=6mm (length), W= 11mm (width), h=0.25mm (thickness); and a GCPW corporate feeding network. The BLT slab was used to impose a linear progressive phase on three antenna elements and the fourth element was used as a reference. Such structure allows to steer the beam from the boresight up to 90^o off-boresight only. Figure **6.2** shows the fabricated sample. A full-wave analysis was performed to optimize the BLT slab size and shape in order to guarantee a linear progressive phase realization. The simulation results show good beam-steering capabilities at the operating frequency band 29-31 GHz.

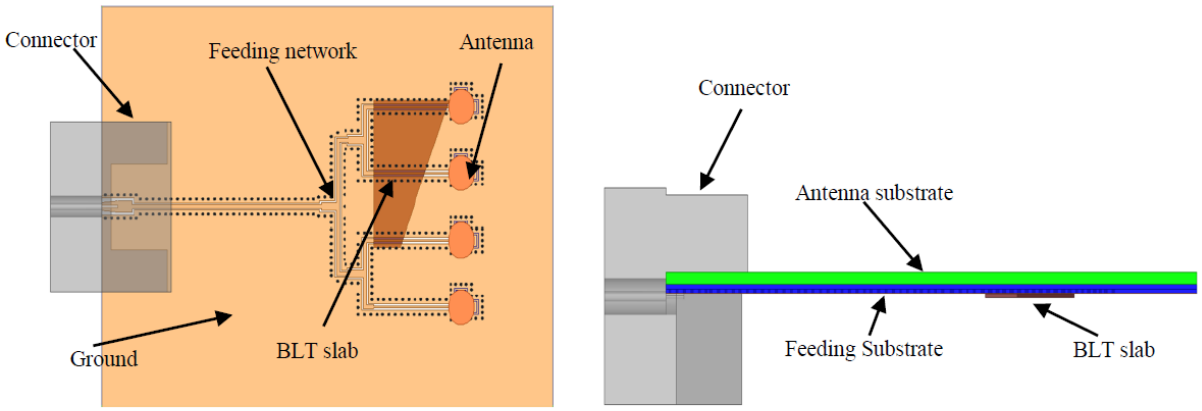

(a) Top view of the antenna structure (b) Side view of the antenna structure

Figure 6.1: Proposed 1×4 CP passive PAA.

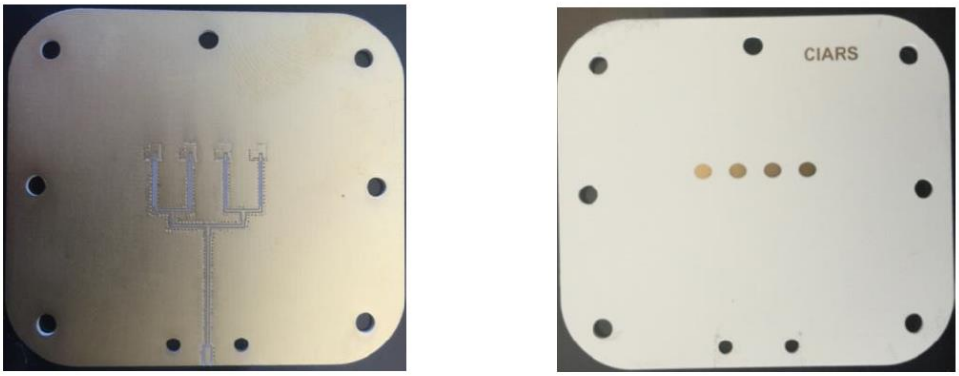

(a) Antenna sub array backside (b) Antenna sub array front side

Figure 6.2: Fabricated 1×4 CP passive PAA.

To test this particular type of array, a micrometer positioner was used to control the height of the air gap between the BLT slab and GCPW TLs, as shown in Figure **6.3**. The proposed CP passive PAA was tested with a PNA-X to evaluate its RL for three different gap cases and the results were compared with simulation results. The following three air gap heights were tested case1 (far from the TLs; ~60μm), case2 (moderate distance; ~24μm), and case3 (very close to the TLs; ~8μm).

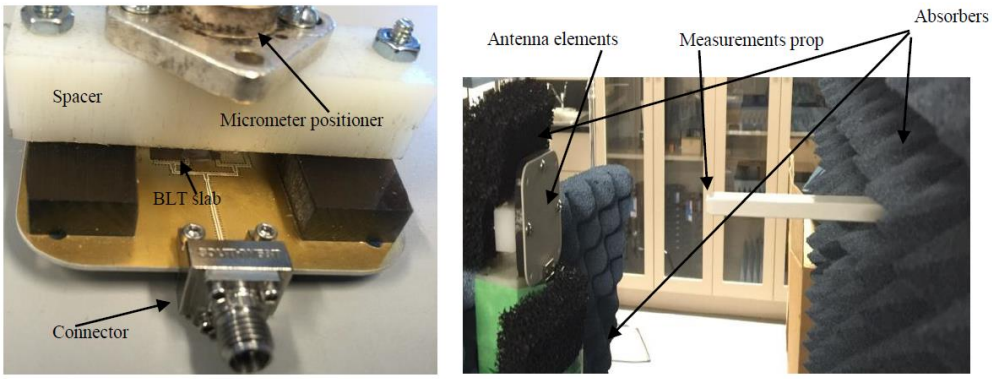

(a) Antenna measurements assembly backside (b) Antenna under test

Figure 6.3: Measurement setup for 1×4 CP passive PAA.

The measured and simulated RLs are shown in Figure 6.4. Good agreement between the results can be observed, despite the fact that the effects of connector loss and the presence of the micrometer positioner and fixing screws were not included in the simulation. Both measurement and simulation results show a 2 GHz RL $|S_{11}| \leq$-10 dB for all cases.

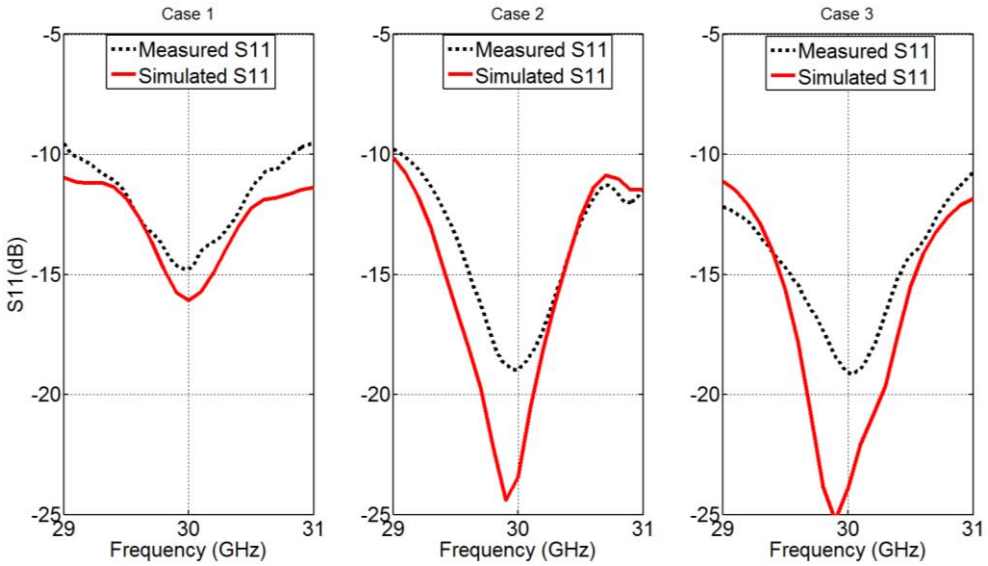

Figure 6.4: Measured and simulated S_{11} of 1×4 CP passive PAA.

Additionally, antenna radiation pattern measurement was performed on the proposed structure for the same aforementioned cases. Measured antenna patterns (Figure **6.5**) agree with simulated patterns for all cases. There are small discrepancies between the results over the SLL because the simulation did not include the effects of connector loss, micrometer positioner, and fixing screws. The antenna beam was steered up to 25º from the boresight with an excellent Co-pol beam and good AR levels (~1.5

dB) for all three cases. It should be noted that the limited beam-steering capabilities of this structure is mainly due to two factors. First, a straight GCPW TL was used for the phase shifter circuit instead of an electrically longer TL (e.g., meander or slow-wave). Second, a better surface finish on both the GCPW TLs and BLT slab (given the BLT slab is used as a single large block instead of a small slab for each antenna element), would have allowed for smaller air gap heights (<8μm; equivalent to higher phase shift). These were the main limiting factors of wide-angle beam-steering for this particular structure.

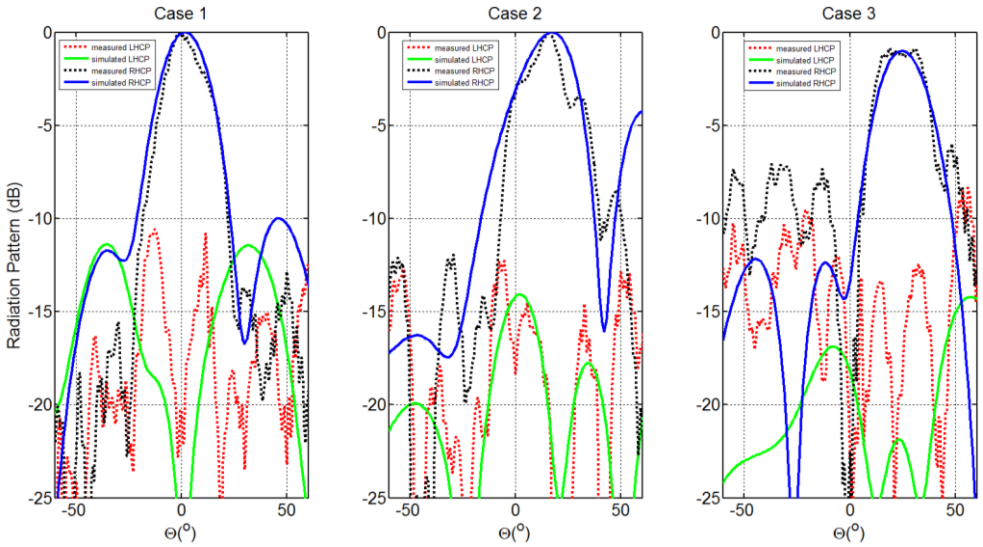

Figure 6.5: Measured and simulated radiation patterns of 1×4 CP passive PAA with micrometer positioner.

6.3 1×4 mm-W CP passive PAA

To enhance the array's beam-steering capabilities and to reduce the array's profile, the phase shifter described in Section 5.5 and the CP antenna from Section 3.2 were integrated to construct a proof-of-concept low-profile 1×4 CP passive PAA to operate at Ka-band frequency range 29-31 GHz. The design consisted of four CP antenna elements arranged in a linear grid, four phase shifters, and a corporate feeding network. In the proposed structure, since each antenna element has a phase shifter that can be controlled independently, the beam can be steered in two directions off-boresight. The proposed phase-shifting mechanism is not only able to compensate for substrate warpage but also for other inevitable mechanical and fabrication errors. Therefore, accurate and flexible beam-scanning can be achieved over the angles ranging from -90° to +90° in elevation—an advantageous feature of

the proposed passive PAA over existing solutions [24, and 84-90]. The proposed array was fabricated on a 4000 series three-layer PCB from Rogers Corp. A 5mm ($\lambda_o/2$) inter-element spacing was used. The proposed passive PAA was simulated for different scanning angles over the frequency band of interest.

6.3.1 Measurement and simulation results

A PNA was used to measure the RL (S_{11}) of the fabricated CP passive PAA. The antenna shows an $|S_{11}|$ <-10 dB over the operating frequency band for all steering angles with small variations as shown in Figure 6.6. The PNF measurement system from NSI was used to measure the radiation characteristics of the passive PAA. The measurement setup is illustrated in Figure 6.7b. A look-up table was extracted for each phase shifter by employing the PNF system probe. The probe was placed very close to each antenna element; by varying the current source the phase range could be obtained for each individual antenna element. The extracted data were saved as a look-up table. The theoretical basis of this calibration method is introduced in [129]. The look-up tables were loaded to a computer and the AF theory was used to calculate the required progressive phase to steer the beam of the AUT towards different elevation angles. The maximum realized phase shift was 320°, when a 100mA current was applied to the magnetic coils.

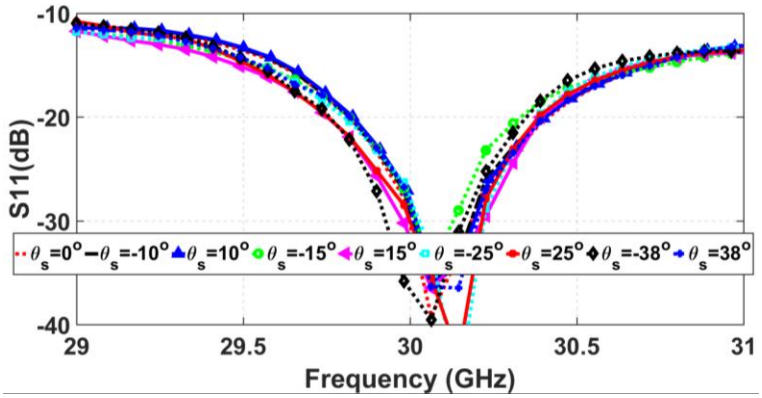

Figure 6.6: Measured RL at different steering angles.

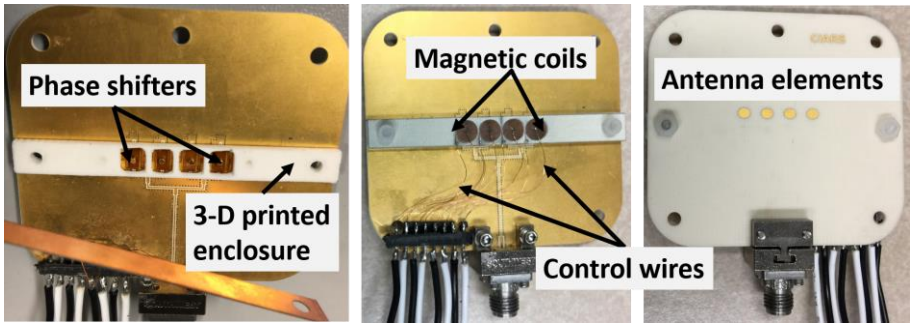

(a)

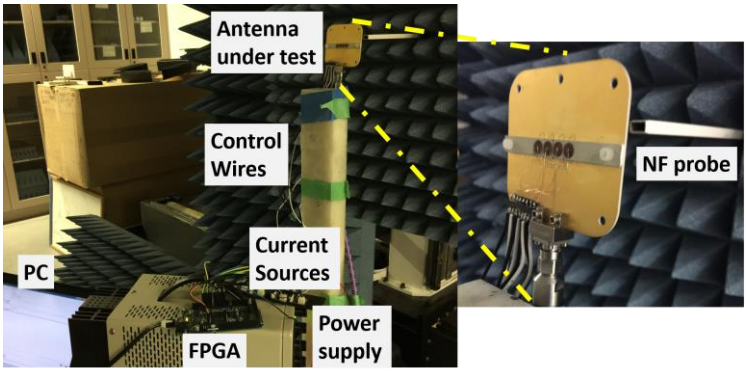

(b)

Figure 6.7: Measurement setup: (a) fabricated CP passive PAA, (b) PNF measurement setup.

The passive PAA was tested over the frequency band of 29-31 GHz. Measurement results were compared to simulation results for three different steering angles at 30 GHz. An RHCP beam was realized with high X-pol discrimination. Measurements showed a 20 dB X-pol discrimination at boresight; agreeing with simulation predictions. Furthermore, a SLL < 11 dB was found by both measurement and simulation. In addition, the measured results agree with those found through simulation for the ±25^{o} steering angles, as shown in Figure **6.8**. For completeness, the PNF system was used to measure the directivity and gain of the AUT. The standard method consists of two steps: a) measuring the directivity from the scanned data, and b) using a standard gain horn antenna to calibrate the PNF system. The antenna gain is then obtained from the measured directivity and the standard gain measurement.

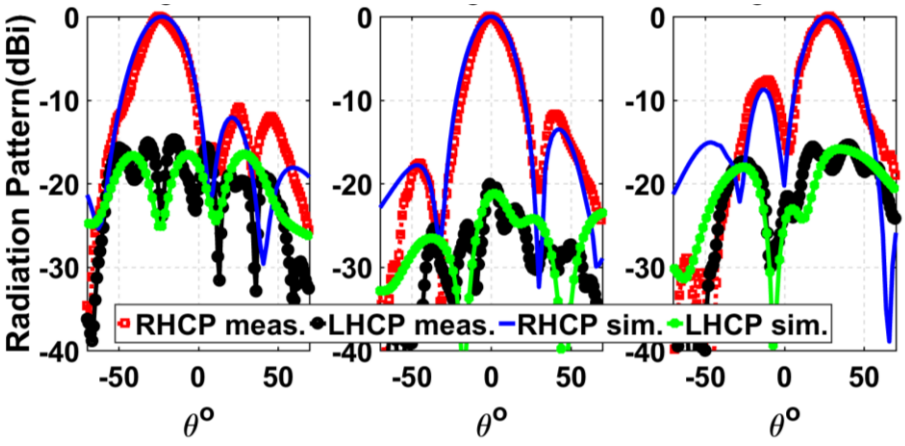

Figure 6.8:Measured and simulated radiation patterns at 30 GHz for different steering angles: (a) -25°, (b) 0°, and (c) +25°.

The maximum measured gain was 7.4 dBi with a 0.5 dB variation. The maximum measured directivity was 9.75 dBi with a 0.5 dB variation over the operating frequency band for the boresight case. A good correlation was observed between the measured and simulated gains, and between the measured and simulated directivities, as shown in Figure **6.9**a. The passive PAA shows a measured radiation efficiency of 60% at 30 GHz—exceptional performance for a passive PAA system. To the best of the author's knowledge, no similar performance has been reported in the literature. The measured and simulated radiation efficiencies are depicted in Figure **6.9**b.

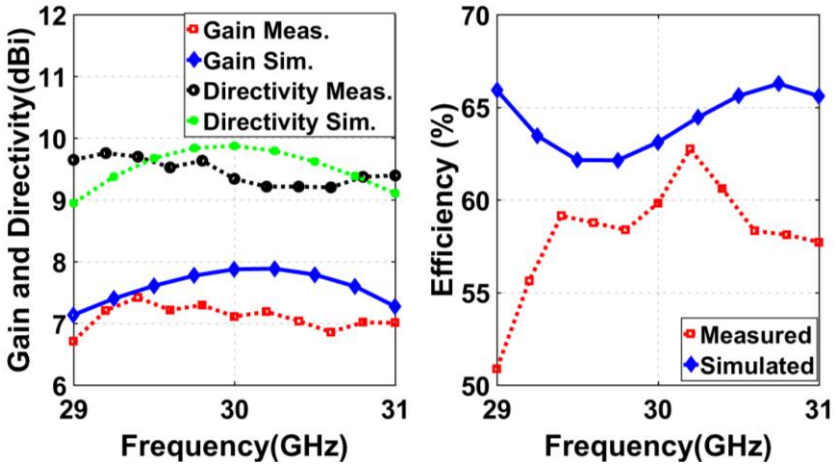

Figure 6.9: Measured and simulated: (a) gain and directivity, (b) radiation efficiency.

6.3.2 Measurement summary

The developed CP passive PAA was tested for different steering angles in elevation to validate its performance and capabilities. The main beam was steered towards the angles 0^o, $\pm10^o$, $\pm15^o$, $\pm25^o$, and $\pm38^o$, and it demonstrated an RHCP beam with a low pointing error ($<2^o$) in all cases over the frequency bandwidth 29.5-30.5 GHz with an AR < 3dB. Figure **6.10** (a-e) illustrates the measured RHCP and LHCP components of the proposed CP passive PAA. It can be observed that the main beam was properly formed at all steering angles. The proposed PAA maintains good CP and high X-pol discrimination over a 1 GHz frequency band centered at 30 GHz, with excellent beam pointing and acceptable SLLs. The proposed passive phased array demonstrates a gain variation of about ~ 1dB at 30 GHz, for different steering angles. This gain variation is due to the scanning loss. Theoretically, the SLLs for any $\pm\theta_s$ should be the same. However, due to the limited number of calibration points, the phase shifters' characterization in this initial stage of research was not very accurate and most of the calibration data (over the entire phase shift range) were obtained by interpolation over a limited number of measurements. This inaccuracy led to asymmetry in the measured gain and SLLs. Table **6.1** summarizes the radiation characteristics of the proposed passive PAA at 30 GHz for different scanning angles.

Finally, an extensive comparison between the presented CP passive PAA and state-of-the-art passive PAAs is shown in Table **6.2**. This comparison focuses on aspects that are the most critical factors in designing an efficient and low-cost passive PAA suitable for implementation in a large-scale system. As can be seen form the table, CP passive PAA exhibits the best performances compared to the-state-of-the-art passive PAAs in terms of size, beam-steering capabilities, and radiation efficiency.

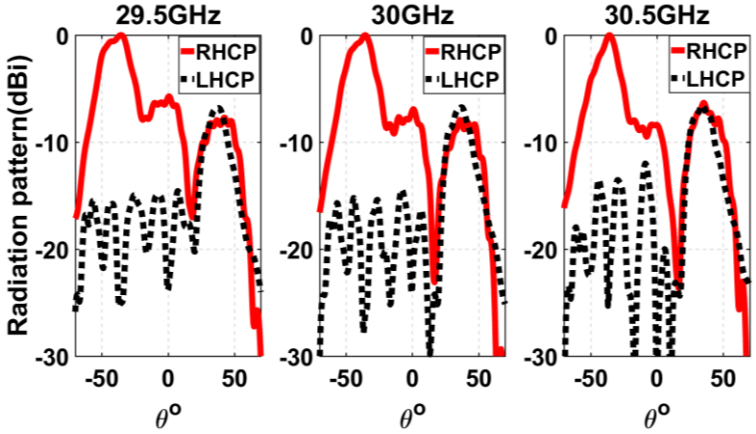

(a)

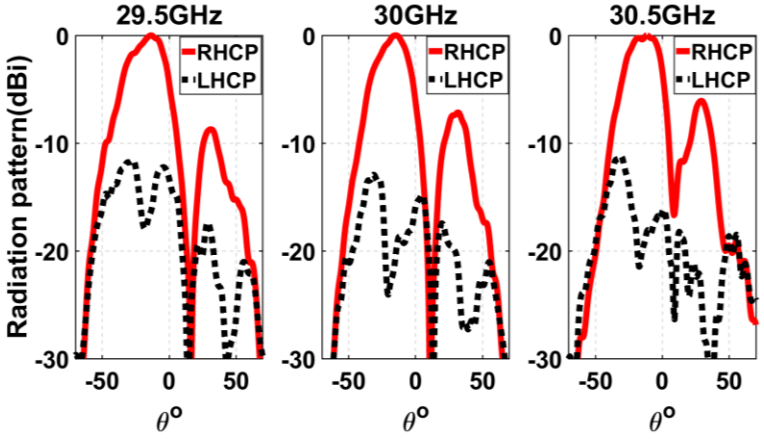
29.5GHz
30GHz
30.5GHz
RHCP
LHCP
Radiation pattern(dBi)
0
-10
-20
-30
-50
0
50
θ°

(b)

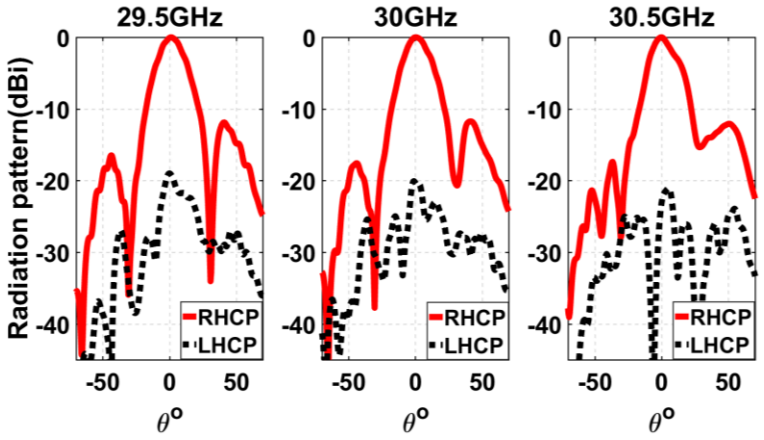
29.5GHz
30GHz
30.5GHz
RHCP
LHCP
Radiation pattern(dBi)
0
-10
-20
-30
-40
-50
0
50
θ°

(c)

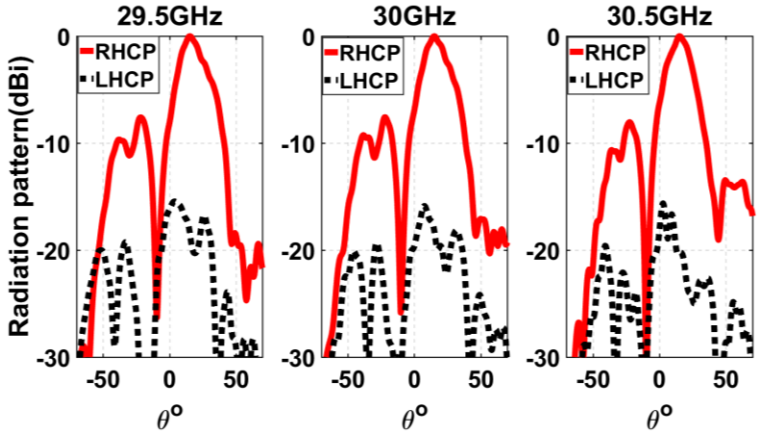
29.5GHz
30GHz
30.5GHz
RHCP
LHCP
Radiation pattern(dBi)
0
-10
-20
-30
-50
0
50
θ°

(d)

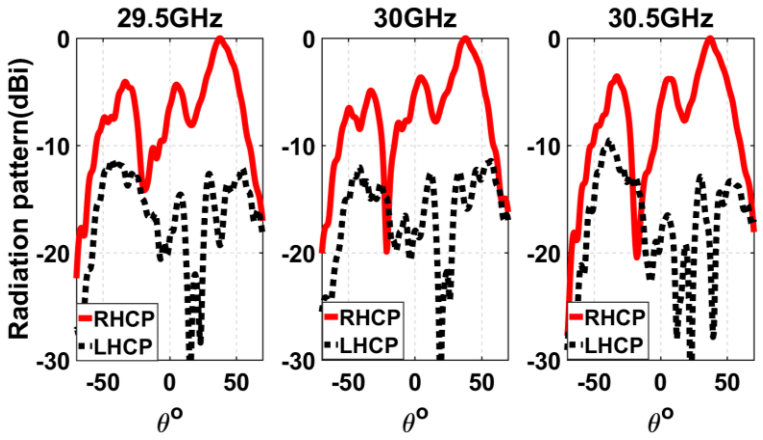

(e)

Figure 6.10: Measured RHCP (Co-Pol) and LHCP (X-Pol) patterns at 29.5, 30, 30.5 GHz: (a) -38º, (b) -15º, (c) 0º, (d) +15º, and (e) +38º.

Table 6.1: Summary of 1×4 CP Passive PAA measurement results.

29.5 GHz									
	-38º	-25º	-15º	-10º	0º	10º	15º	25º	38º
X-Pol discrimination (dB)	22	16	16.3	18.6	19	19	18.8	15.8	19.3
1st SLL (dB)	6	9.7	8.7	9.6	11.9	10.6	7.6	7	4.4
30 GHz									
X-Pol discrimination (dB)	23	22.5	20.4	18.4	20.33	22	18.4	17.9	15.85
1st SLL (dB)	7	10.9	7.2	9	11.75	11.9	7.6	7.6	3.7
30.5 GHz									
X-Pol discrimination (dB)	19.4	15	18.7	18.3	23	20.7	20.2	16	20.7
1st SLL (dB)	8.35	16.5	6	9.7	12.1	13.5	8	7.8	3.8

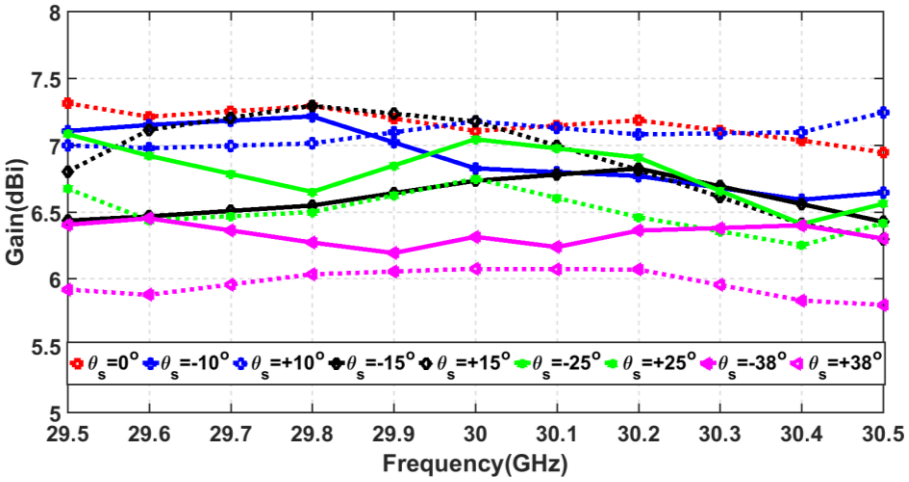

Figure 6.11: Measured gain at different steering angles.

Table 6.2: Comparison of state-of-the-art passive PAAs.

Criteria	[24]	[84]	[86]	[88]	[89]	This work
Frequency (GHz)	60	16	33	30	15	30
Scanning coverage	1-D	1-D	1-D	1-D	1-D	1-D
Measured scanning	-1.6°-+2.9°	0-30°	-21°-+24°	-17°-+19°	0-25°	-38°-+38°
Polarization	LP	LP	LP	LP	LP	CP
Measured Gain (dBi)	15	-	-	-	8	7.15
Efficiency %	39.9	-	-	-	-	60
Profile	High	High	High	High	High	Low
Array size	1×16	1×4	1×8	1×8	1×4	1×4
Voltage range (V)	0-100	0-60	0-50	0-40	0-60	0-0.1
Actuation	PET	PET	PET	PET	PET	Magnetic actuator
Packaged	No	No	No	No	No	Yes

6.4 Tunable Ka-band RAA element

6.4.1 Introduction

A new reconfigurable RAA with true-time-delay functionality was developed. Its reconfigurability was realized by loading a GCPW line with a high dielectric constant slab. A mechanical actuator was employed in the proof-of-concept prototype to precisely control the reflection phase of the unit cell (UC). An ACMPA was used to receive and re-radiate the electromagnetic energy efficiently. It was designed using a low-cost PCBs process so that a low-cost and high-performance large-scale steerable RAA could be developed for mm-W applications. The proposed UC was designed and tested over the frequency range of 27.5-30 GHz. Measurements show that a reflection phase of almost 360^{o} could be realized, over an 8.7% frequency band, with a maximum reflection loss of 4.5 dB.

6.4.2 Geometry and design concept

A conventional ACMPA was used as a reflecting element with tunable reflection phase capability. It consisted of a rectangular microstrip patch, an aperture slot, and a GCPW feed line. A series slot was connected to the GCPW line to provide strong coupling between the feed line and the aperture to excite the radiating patch. A high dielectric slab was placed on a portion of the GCPW. This slab was of a sufficient length to realize more than 360^{o} reflection phase over the entire operating frequency band. The reflection was generated by a short circuit at the end of the GCPW line. This type of GCPW reflective termination minimizes the spurious emission and reflection loss. The amount of phase shift that can be achieved in this configuration was found to be double that of the traveling-wave type of phase shifter presented in Chapter 5. This is because the electromagnetic wave will pass through the phase shifting region, beneath the dielectric slab, twice. A precise mechanical actuator can be used to adjust the gap between the dielectric slab and the GCPW line to vary the delay, and thereby properly adjust the reflection phase. MEMS, PET, micrometer positioner, and magnetic actuator are possible candidates for use as actuators to realize the desired phase tunability.

The design steps of the proposed UC proceed from the initial analysis of system requirements (e.g., operating frequency band, radiation pattern, and polarization) can be summarized as follows: (i) selection of optimal configuration for the UC and integrated phase-shifting element (including actuation mechanism), and selection of low-loss and low-cost substrates for both the antenna and phase shifter; (ii) design and optimization of the antenna element for efficient radiation and desired polarization; (iii) design of the phase-shifting element based on equation (3.1); (iv) integration of the

phase-shifting element with the antenna; and (v) co-optimization of the antenna and the phase-shifting elements using a full-wave simulator to obtain the maximum tunable reflection phase range and minimum reflection loss.

The geometry of the ACMPA used for this proof-of-concept UC is shown in Figure **6.12**. The antenna was designed to operate over the frequency band of 27.5 GHz to 30 GHz. RO4360G2 (ε_r = 6.15, thickness of h_1=0.203 mm) and RO4003 (ε_r = 3.55, thickness of h_3=0.508 mm) were used as low-cost PCB materials to realize the GCPW line and the rectangular microstrip patch, respectively, and RO4450F (ε_r = 3.52, thickness of h_2=0.203 mm) was used to laminate the two substrates.

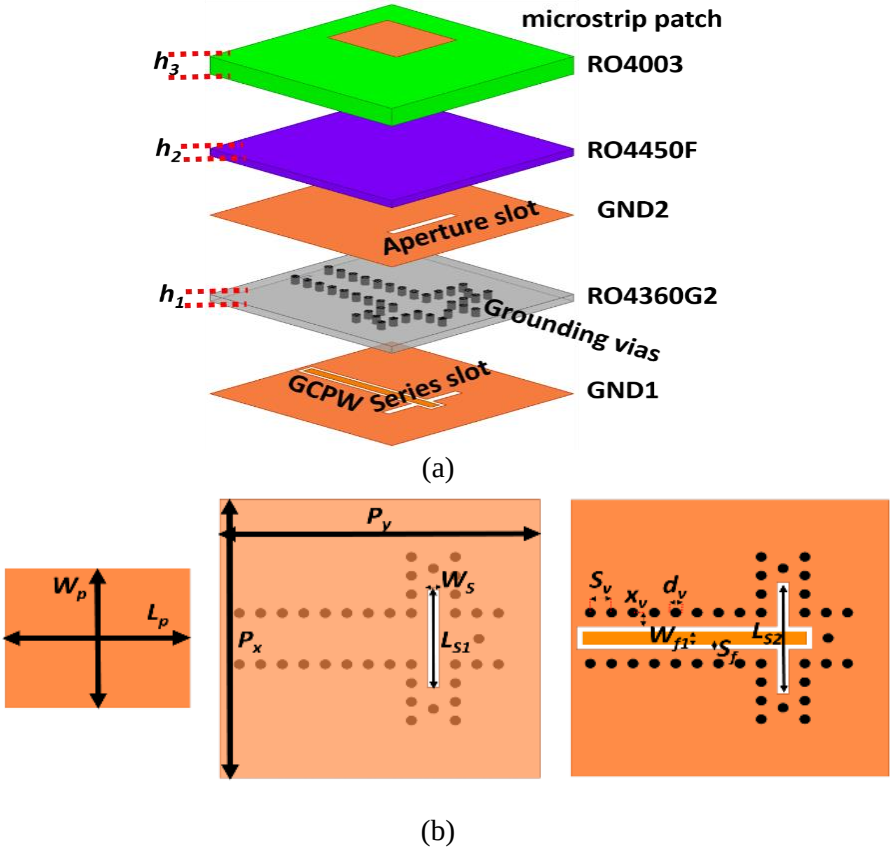

Figure 6.12: ACMPA: (a) 3-D schematic view (b) metal layers.

6.4.3 Analysis and simulation results

Extensive full-wave simulations were performed to design and optimize the antenna to realize sufficient operational bandwidth, proper polarization performance, and radiation characteristics. The optimized antenna parameters are shown in Table 6.3. A 17 μm copper was used for all three metal layers in this simulation, to incorporate both the metallic and dielectric loss. Simulations show that a

wideband RL ($|S_{11}|$<-10 dB) was achieved when the antenna operated over the frequency band of 26 GHz to 30.5 GHz (~16%). It realized an $|S_{11}| \leq$ -15 dB over the frequency range 26.5-29.75 GHz, as shown in Figure **6.13**a. Furthermore, the simulated antenna showed a linearly polarized radiation pattern with high X-pol discrimination, (> 40 dB), good symmetry over ϕ =0° and 90° at the center frequency, and a gain of 5.9 dB. Figure **6.13**b depicts the simulated radiation pattern of the aperture-coupled antenna at 28.5 GHz. Consequently, the antenna element can be used to develop a high performance reflectarray UC.

Table 6.3: Dimensions of ACMPA (mm).

parameter	P_y	P_x	L_p	W_p	W_s
dimension	*6*	*6*	*2.27*	*1.98*	*0.22*
parameter	L_{s1}	L_{s2}	W_{f1}	W_{f2}	S_v
dimension	*2.1*	*2.42*	*0.28*	*0.1*	*0.2*
parameter	d_v	X_v	h_1	h_2	h_3
dimension	0.2	0.2	0.203	0.203	0.508

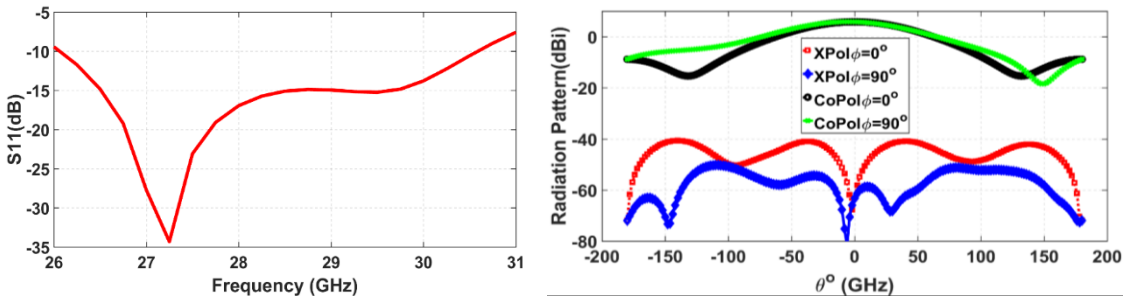

(a) (b)

Figure 6.13: Simulation results of ACMPA: (a) RL (dB), (b) radiation pattern (dBi) at 28.5 GHz.

After designing of the ACMPA is completed, the next step is to integrate the phase-shifting element with the antenna element and co-optimize the structure. With this approach, more than 360° reconfigurable phase shifting can be easily achieved over a wide operating frequency band with minimal gain variation. This is highly desirable characteristic for wideband large-scale steerable mm-W RAAs. A convenient choice for dielectric slab is to use BLT material with an ε_r =165 and $\tan_\delta$=0.01. For the proposed design reported, the optimal BLT dimensions were (length) L_{BLT}=3.3 mm, (width) W_{BLT}=2 mm, and (thickness) h_{BLT}=0.2 mm. With these dimensions, a variable airgap (spacing

between the BLT and GCPW line) with a maximum range of 11 μm is required to obtain a 360° phase shift. To match the impedance of the phase shifting section to the aperture-coupled antenna, the width of the GCPW line below the BLT slab is reduced from W_{f1}= 0.28 mm to W_{f2}= 0.11 mm, so that the propagating wave under the phase shifter would not experience any additional scattering or reflection. The antenna, integrated with the BLT phase shifter, is shown in Figure **6.14**. Variation in the airgap (h_{gap}) affects the reflection coefficient of the antenna element due to the perturbation generated by the BLT slab in the GCPW transmission mode. However, within the operating frequency band 27.5-30 GHz the $|S_{11}|$ was kept below -10 dB as the gap varied between 2-13 μm. Figure **6.15** shows the effect of the BLT slab on the input reflection coefficient of the antenna element for different gap sizes. Furthermore, the impact of the BLT slab on the radiation pattern of the antenna element was studied to ensure the antenna would be able to receive and re-radiate the electromagnetic wave efficiently. The simulated radiation pattern in the upper hemisphere of the antenna element integrated with the BLT slab is demonstrated in Figure **6.16**. As can be seen from the figure, the Co-Pol component shows minimal variation, but the X-pol component shows a noticeable change as the gap is varied.

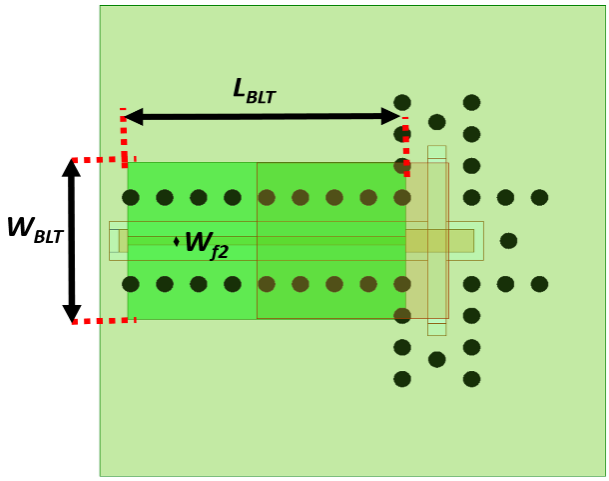

Figure 6.14: ACMPA integrated with BLT phase shifter.

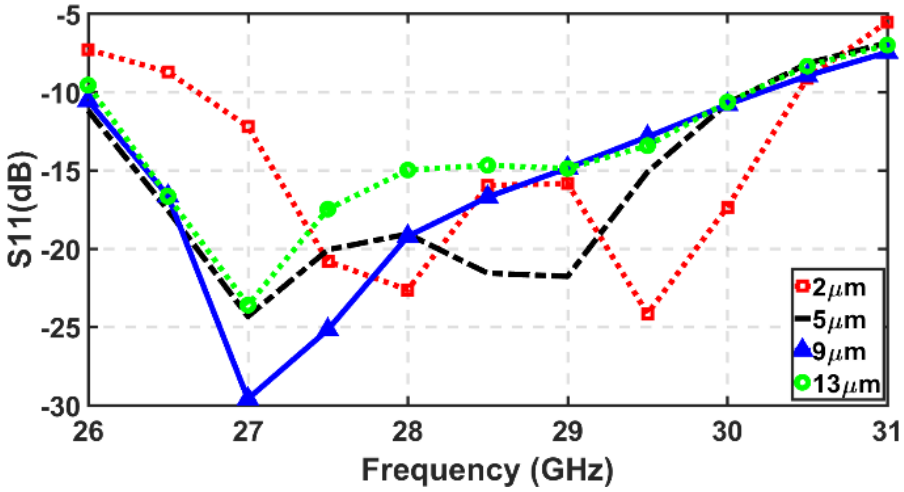

Figure 6.15: Simulated S_{11} (dB) of ACMPA.

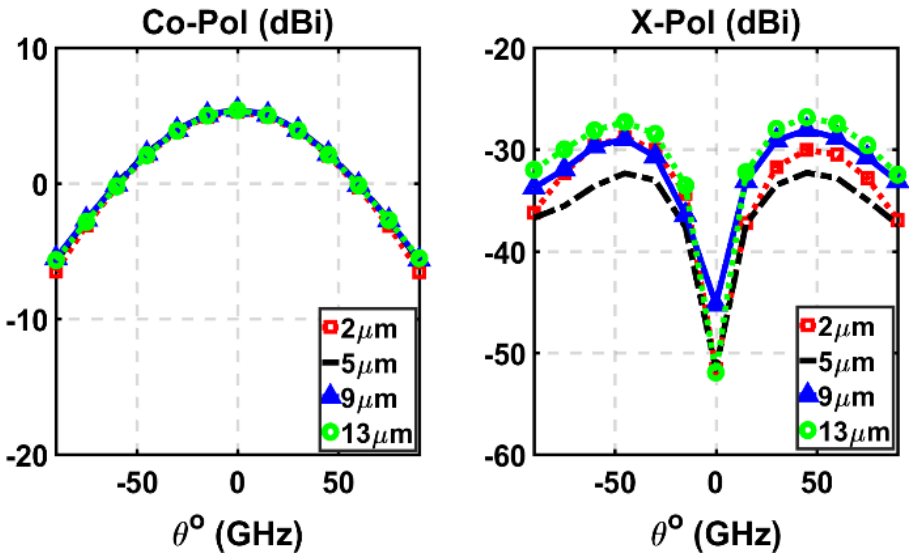

Figure 6.16: Simulated Co-pol and X-pol components at 29 GHz for different h_{gap} values.

Finally, the antenna element with BLT phase shifter was simulated as a RAA UC using PBCs. The end of the GCPW line was short circuited to ground so that the incident wave would be reflected back and re-radiated. The simulation setup of the UC inside the PBC is shown in Figure **6.17**. The UC was simulated over the frequency band of 27.5-30 GHz with an h_{gap} variation range of 2-13μm. This gap variation range is the displacement range of a typical 1 cm PET. Simulations showed that when the UC was excited by a normal incident transverse electric (TE) wave and the h_{gap} was varied over the range of 2-13μm, a reflection phase ranges of 395° and 391° were realized at 27.5 GHz and 30 GHz, respectively. Furthermore, maximum reflection losses of 3.2 dB and 2.2 dB were observed,

with variations in the reflection loss of 2.5 dB and 1.15 dB, at 27.5 GHz and 30 GHz, respectively. Figure **6.18**a depicts the simulated reflection phase ($S_{11}{}^{o}$) versus h_{gap} size at different frequencies. The UC shows a minimal variation of phase over the frequency band; hence, a flat gain performance can be realized from a reflectarray made of the proposed element. The simulated reflection loss of the UC is shown in Figure **6.18**b.

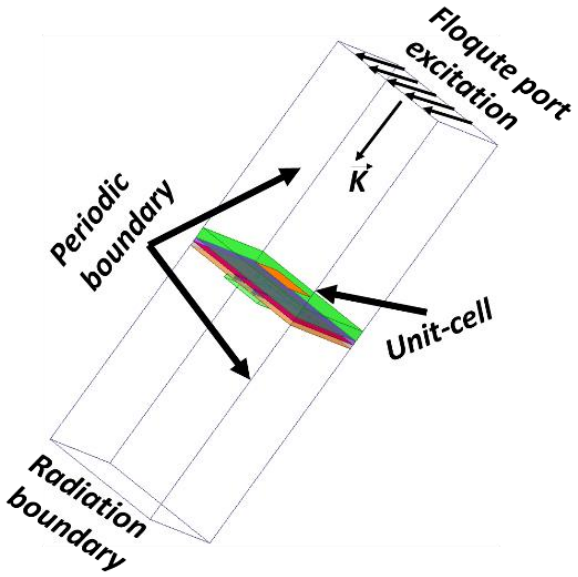

Figure 6.17: UC simulation setup.

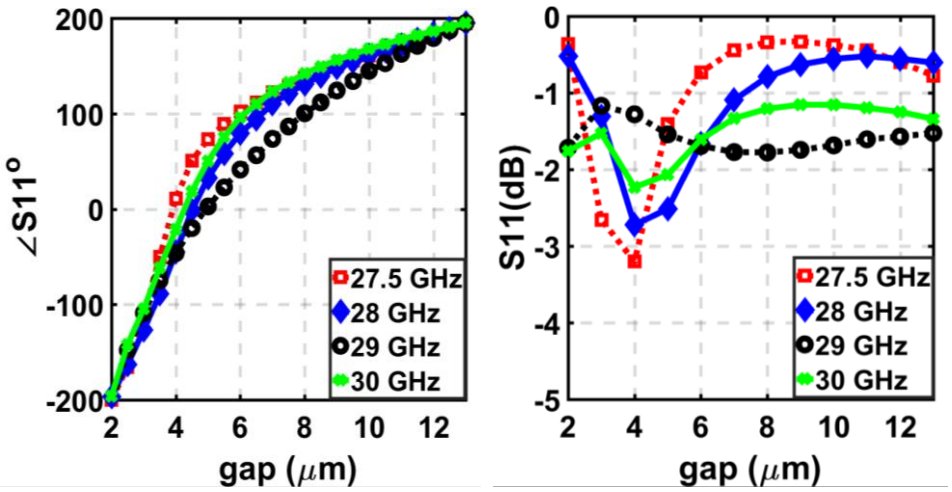

(a) (b)

Figure 6.18: Simulation results for RAA UC: (a) reflection phase (degrees), (b) reflection loss (dB).

The simulations reported in Figure **6.19** illustrate the operation of the proposed UC when it is excited by a normally incident plane wave (y-polarized electric field) with the proper polarization. It

can be seen from this figure that the incident wave is coupled to the GCPW line through the patch-slot. It then propagates over the GCPW line, experiencing different propagation delays based on the location of the BLT slab in relation to the GCPW line. The wave is reflected by the short circuit at the end of the GCPW. The reflected wave is re-radiated to space with the reflection phase determined by the gap size h_{gap}. The simulations were performed for three different values of h_{gap}. As h_{gap} becomes smaller, the electric length of the GCPW line increases; hence, a tunable true-time-delay reflectarray can be realized by using this concept.

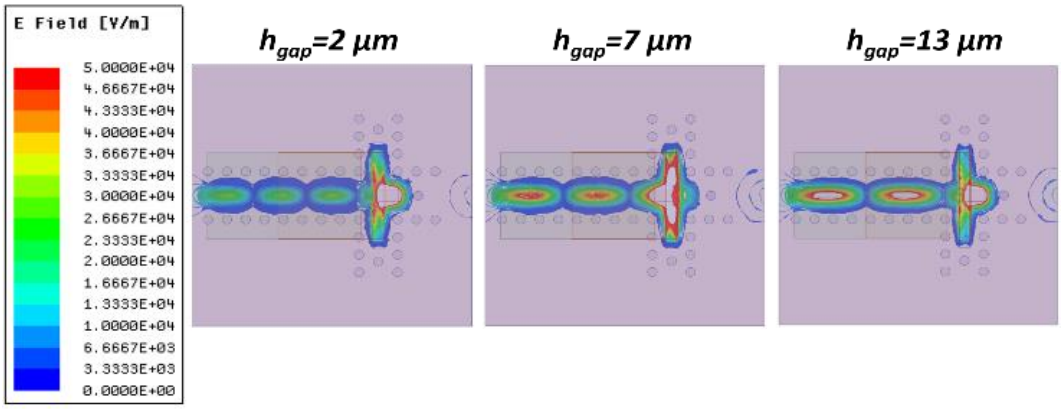

Figure 6.19: Simulated electric field (V/m) inside GCPW substrate at different h_{gap} sizes at 28.75 GHz.

6.4.4 Fabrication and measurement results

A common practice when designing an RAA is to evaluate the antenna UC experimentally to validate its design performance before using it to realize a large antenna array. The measurement setup consists of a standard metallic rectangular waveguide fed by a coaxial cable and a metallic rectangular waveguide transition (Figure **6.20**) to host the antenna UC. The antenna UC is embedded inside the waveguide transition to include the mutual coupling effects (based on infinite image theory [84]). A TE_{10} wave is excited inside the metallic waveguide; this can be modeled by the two plane-wave incidents on the transverse walls of the waveguide. The incident angle can be calculated based on the equation (6.1):

$$sin\theta = \frac{\lambda_o}{\lambda_c} \qquad (6.1)$$

Where θ is the incident angle, λ_o is the free space wavelength at the operating frequency, and λ_c is the cut-off wavelength of the propagating mode. The Ka-band WR-28 metallic rectangular waveguide operates in the frequency range of 26.5 to 40 GHz, and has dimensions of WWR-28 =7.112 mm and

LWR28 =3.556 mm. It was used as a measurement sensor. A metallic rectangular transition (dimensions of W_1=W_2=WWR-28 and L_1=LWR-28, L_2= 5mm and d=20 mm) was designed and optimized by full-wave simulator to be connected to the WR-28, to be terminated by the antenna UC as shown in Figure **6.20**.

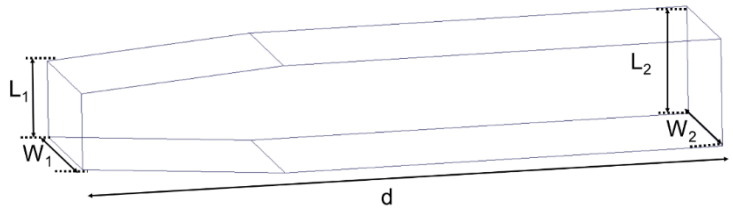

Figure 6.20: Ka-band metallic rectangular waveguide transition.

The proposed reflectarray UC was fabricated by using a low-cost PCB process. substrates. A rectangular annular metal ring was etched on the top layer and connected to the ground with plated vias to mimic the infinite array condition. The top and bottom views of the fabricated UC are shown in Figure **6.21**. A WR-28 metallic waveguide-coaxial transition was used to test the fabricated UC. Furthermore, a commercial PET with dimensions of *L*, *W*, *h* = 3×3×11 mm^3 (can generate up to 11μm normal displacement range), was used as an actuation mechanism in this proof-of-concept prototype. A PNA-X from Keysight Technologies was employed to measure the reflection phase and reflection loss over the operating frequency band. The measurement setup is shown in Figure **6.22**.

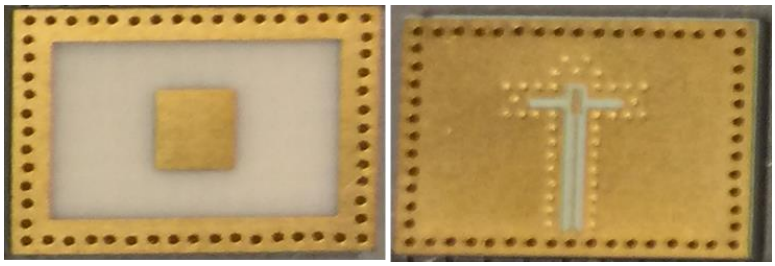

(a) (b)

Figure 6.21: Fabricated RAA UC: (a) top view, (b) bottom view.

The proposed RAA UC was measured for different h_{gap} sizes. The measured reflection phase is presented in Figure **6.23**a for the frequency range of 27.5-30 GHz. The figure shows that the reflection phases correlates quite well with the simulated results shown in Figure **6.18**a. The measured reflection phase ranges are 0º-357º and 0º-340º at 27.5 GHz and 30 GHz, respectively. In addition, Figure **6.23**b shows that the maximum measured reflection losses were 4.6 dB and 3.4 dB, with variations of 4 dB and 2.5 dB, at 27.5 GHz and 30 GHz respectively. The discrepancies between

the measurement and simulation (Figure **6.18**b) results are attributed to two main factors. First, there is a misalignment between the BLT slab and the GCPW line (the main source of the discrepancies as described in Subsection 5.3.1). Second, there are fabrication errors and uncertainties of the dielectric constant. Table **6.4** compares the performance of the proposed UC with state-of-the-art reconfigurable RAA elements. The proposed UC exhibits the widest operating frequency band, while realizing a reflection phase of almost 360°.

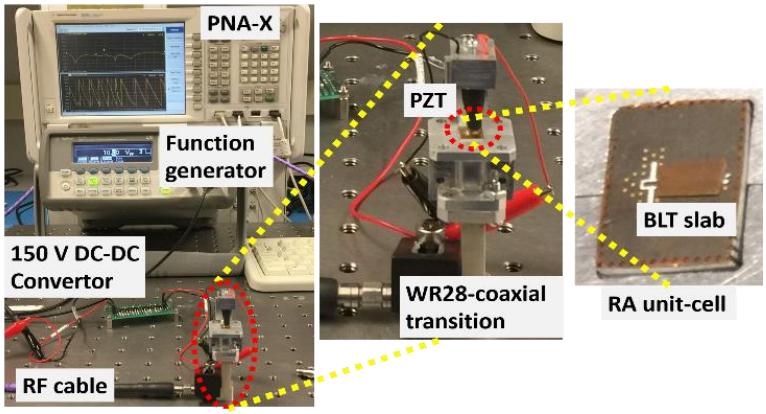

Figure 6.22: Measurement setup for RAA UC.

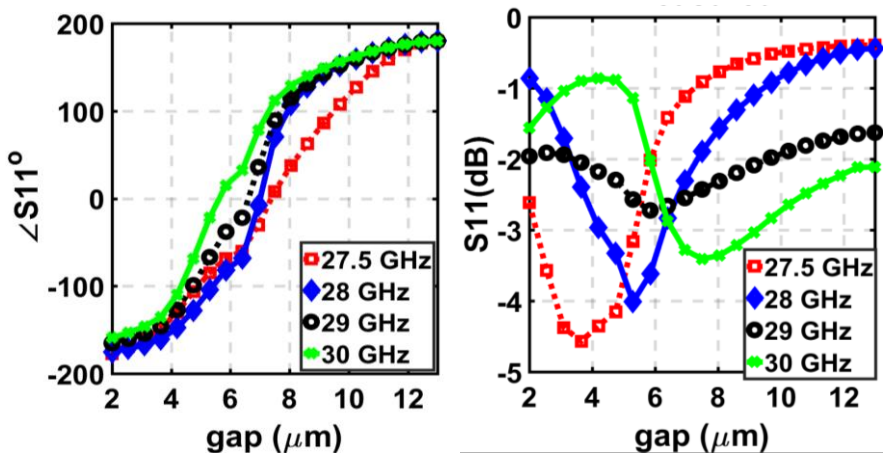

(a) (b)

Figure 6.23: Measurement results for proposed RAA UC: (a) reflection phase (degrees), (b) reflection loss (dB).

Table 6.4: Comparison of proposed RAA UC versus legacy reconfigurable RAA elements.

Ref	[91]	[92]	[93]	This work
Frequency (GHz)	5.4	58.14	30	27.5
Maximum reflection phase (Deg.)	380	200.6	298	357
Maximum reflection loss (dB)	3.5	12	16	4.5
Bandwidth (%)	2.4	<1	5.7	8.7

6.5 Conclusion

The process of developing and successfully fabricating a novel Ka-band CP passive PAA was presented, along with measurement results. To the best of the author's knowledge, it is the first time that a multi-antenna module, employing a BLT-based phase shifter, has been introduced for a CP passive PAA with full electronic control of each individual antenna element. The proposed system was implemented using a low-cost PCB technology. A low-profile and efficient magnetic actuator, developed at CIARS, was utilized to control the phase shifter. A wide scanning angle was achieved with high precision. Given these results, the presented module is an excellent candidate for large-scale mm-W PAA systems with full electronic beam-control capabilities toward any azimuth and elevation.

Finally, the design, analysis, and measurement of a new broadband reconfigurable RAA UC were presented and the proposed design was fabricated to operate in the Ka-band. A true-time-delay reflection mechanism was realized by placing a rectangular slab with a high dielectric constant on top of a GCPW line coupled to a patch antenna through a slot. A waveguide simulator was used to characterize the proposed UC and a PET was employed to control the reflection phase. A measured reflection phase range of 357^{o} was realized at 27.5 GHz with a maximum reflection loss of 4.5 dB; hence, it is believed that the performance of the proposed design is superior to that of legacy reconfigurable RAA element designs reported to date for this frequency range. The measured results agree well with those from simulations. Finally, the developed structure and its fabrication method use a low-cost standard PCB process making it a simple and highly cost-effective solution for large-scale high-performance mm-W RAAs with wide angle beam-steering capabilities.

Chapter 7
Conclusion and Future Work

7.1 Conclusions

This chapter presents an overall summary of the thesis chapters and contributions made by this PhD thesis. A list of the journal and conference papers disseminating findings from this research is included in Appendix A.

The currently available solutions (e.g., reflector antenna, fixed beam array antennas with mechanical steering, digital beam-forming-based PAAs) are not the optimal for SOTM applications due to the high-profile and slow response of mechanical steering systems and the high-cost and complexity of digital beam-forming PAAs. On the other hand, it has been shown that the available passive phased arrays suffer from limited beam-steering capabilities because of the size and configuration of the phase shifters. In addition, state-of-the-art passive phased arrays utilize a bulky PET to steer the radiation beam of the phased array, and to the best of the author's knowledge, no CP passive phased array has been reported in the literature to date. Available reconfigurable RAA elements are limited in operating bandwidth as well as exhibit high reflection losses at mm-W frequencies.

In chapter 3, a novel single-fed wideband (> 2GHz) CP antenna was proposed based on the ACMPA concept on low-cost PCB technology. The proposed antenna generates a CP radiation pattern by exciting multi modes from a multimode slot resonator that is loaded by an elliptical microstrip patch antenna. A GCPW line was utilized to excite the aperture slot making the proposed antenna suitable for direct integration with the beam-forming systems and reducing mutual coupling and surface wave effects, particularly for wide-beam steering CP PAAs. The proposed antenna's performance showed low sensitivity to relatively large PCB fabrication errors. A 4×4 fixed beam subarray module was successfully designed, fabricated, and measured to validate the proposed wideband CP performance. Furthermore, as a proof-of-concept, 16 of these modules were mounted on a 1×16 power splitter in a square grid in order to study the modularity concept. Despite all of the mechanical and excitation discrepancies, measured results from the modular structure matched very well with the AF simulated results in terms of AR, radiation pattern, and directivity without needing to introduce any phase or amplitude corrections.

The proposed CP antenna was used in a 4×16 APAA operating at Ka-band. The radiation pattern of the 4×16 APAA was experimentally steered up to ±40^{o} off-boresight with good AR (< 4dB) level over the frequency range of 29.5-30 GHz without any calibration at off-boresight steering angles. Moreover, to show the excellent capabilities of the proposed antenna for SOTM applications, CIARS intelligent beam-forming circuit was used to perform an amplitude tapering and complex excitations to control the SLL and to generate a multi beam pattern, respectively.

To develop a fully working prototype system that meets all the stringent SOTM requirements (Section 2.2) for wideband SOTM communications, a highly integrated and low-profile 4×4 sub-array, to be used in CIARS intelligent beam-forming module, was proposed in chapter 4. The intelligent sub-array module comprises a 4×4 dual-polarized antenna elements, their feed circuits, and active beam-forming MMICs integrated in multi-layer high performance PCB technology. Each 4×4 antenna sub-array was designed on a 2×2 cm^2 area with 0.5λ_o (at 30 GHz) inter-element spacing to avoid grating lobes. The proposed antenna element sustained 2 GHz S_{ii} < -10 dB centered at 30 GHz and the isolation between the two polarizations was S_{ij} < -20 dB at the boresight.

Using the aforementioned 4×4 intelligent module, a 16×16 APAA was fabricated and measured. Measurements show that the beam can be easily steered toward 60^{o} off-boresight over a 3 GHz frequency bandwidth (28-31 GHz) with high pointing accuracy, and high CP purity was sustained up to 30^{o} without calibration. Simulation results showed that if the amplitudes of the two orthogonal polarizations are adjusted properly, very high CP purity can be realized with the aforementioned APAA for wide beam-steering angles.

As a promising wideband, low-cost, and high-performance mm-W phase shifting mechanism, a high dielectric constant slab on top of a GCPW line was employed to develop a passive phased-array in chapter 6. The CIARS phase shifter is an excellent candidate to be employed in the development of a low-cost, compact, and steerable passive phased array. A simple empirical equation was developed to design the phase shifter quickly and accurately. The proposed design equation can be used to analyze the required phase response based on the effective permittivity of the dielectric slab and length to determine the required actuation range at the operating frequency without using a time consuming full-wave simulator. Four different phase shifter configurations were designed, fabricated and tested on low-cost PCB technology to operate at the Ka-band. Measurement results show that a high FOM (> 180^{o}/dB) was realized by the phase shifting approach with low IL variation < 1 dB over the operating frequency band (29-31 GHz); the first time such results were reported.

I had significant contribution to a novel low-cost and low-profile (< 2mm) magnetic actuator, invented in CIARS, for precise control the phase shifter response, replacing the traditional bulky and high-cost piezoelectric actuator. The magnetic actuator was successfully tested with two different phase shifter structures.

The low-profile phase shifter presented in chapter 5, and the single-fed CP antenna presented in chapter 3, were integrated together to construct a novel high performance 1×4 CP passive PAA in chapter 6. It was designed, fabricated, and measured over a 1 GHz frequency bandwidth (29.5-30.5 GHz) with large beam-steering off-boresight (±38^{o}) and high CP purity. The proposed CP passive PAA showed a high radiation efficiency with low-power consumption (40 mW)—such performance is superior to reported state-of-the-art passive PAAs.

Finally, as an attractive alternative solution, a reconfigurable RAA was explored in the second half of the chapter 6. The RAA element operated over a wide frequency bandwidth (≥ 2.5 GHz) with large reflection phase and relatively low reflection loss at Ka-band. It consists of an ACMPA integrated with the BLT phase shifter. A proof-of-concept the UC was designed, fabricated, and measured successfully. It showed a maximum reflection loss of 4.5 dB and reflection phase of 357^{o}. Compared to the legacy reconfigurable RAA reported in the literature, the proposed RAA shows a higher operating frequency bandwidth (8.7%) with lower reflection loss at Ka-band.

7.2 Future work

In an effort to develop modular and scalable architecture for mm-W beam-forming antenna systems that overcome the limitations and drawbacks of currently available solutions, four new antenna element and array concepts were proposed as part of this PhD thesis. These concepts were successfully verified by their incorporation into CIARS array configurations: single-fed CP APAA, dual-fed APAA, CP passive PAA, and reconfigurable RAA.

Simulation and measurement results show that the proposed concepts exhibit remarkable performance; however, there are several opportunities for future research and continuation of this PhD research to further enhance and mature the proposed concepts, such as:

1) The CIARS low-profile magnetic actuator consists of many layers. Rapidly growing 3-D printed additive manufacturing technology offers the opportunity to integrate the actuator body as well as the packaging enclosure in a sophisticated and optimized structure; thereby, an easy assembly and predictable actuator could be developed for large-scale

passive PAAs. On the other hand, the current source of the planar magnetic coil could be integrated with the PCB of the planar coil to further reduce the power consumption and improve the integration. Moreover, repeatability test in different environment conditions and analysis of the mutual interaction among the magnetic actuators in an array form are necessary to evaluate the proposed magnetic actuation concept in more realistic scenarios.

2) The single-fed CP antenna introduced in this research shows a good active impedance performance for wide steering angles (> 50^{o}) over the entire azimuthal range, but the AR > 3 dB was limited to $\theta_s=30^{o}$ in the azimuthal angle of ($\phi_s=0^{o}$). The scanning angle should be extended for larger steering angles by further optimization and extension of the via walls to the antenna substrate. Moreover, multi-layer PCB integration could be used to implement an APAA module based on the proposed wideband CP antenna concept as a low-cost building block for SOTM systems. On the other hand, a dual CP antenna (e.g., work presented by author [130]), could be utilized to develop a switchable RHCP/LHCP APAA module as a building block for SOTM systems with full polarization functionality as a low-cost and simple alternative solution.

3) The CIARS 4×4 intelligent APAA architecture using the proposed dual-fed antenna is an excellent candidate to construct a working prototype that meets all the requirements of a SOTM system. However, further enhancement is required to overcome mutual coupling effects at ≥70^{o}; in other words, to ensure less variation can be seen by the active feed network. Such an improvement could be achieved by utilizing some electromagnetic band gap techniques. Moreover, a large-scale APAA (> 1k elements) would need to be implemented to test the proposed concept in a realistic environment with wideband modulated single.

4) The current CP passive PAA using the proposed CP antenna element showed a high-performance beam-steering capability with low-cost technology. An extension of this research is urgently needed to develop a planar CP passive PAA that takes into consideration the suggestions regarding the phase shifter made in point one above.

5) An initial high-performance reconfigurable RAA element, using BLT phase shifter, was presented in this research. A steerable passive RAA could be developed by utilizing the proposed UC in combination with an improved phase shifter based on the suggestions made in point one above. Utilizing the CP antenna that was proposed in chapter 4 to

develop a CP reconfigurable RAA is another important aspect should be considered in the future. Moreover, another direction that could be followed would be to utilize a dual-band antenna (e.g., work presented by author [131]), could be utilized to develop a Tx/Rx passive RAA. Such a contribution is seen as an excellent research opportunity.

Bibliography

[1] S. Sanzgiri, D. Bostrom, W. Pottenger and R. Q. Lee, "A hybrid tile approach for Ka band subarray modules," in IEEE Transactions on Antennas and Propagation, vol. 43, no. 9, pp. 953-959, Sept. 1995.

[2] T. Lambard, O. Lafond, M. Himdi, H. Jeuland, S. Bolioli and L. Le Coq, "Ka-Band Phased Array Antenna for High-Data-Rate SATCOM," in IEEE Antennas and Wireless Propagation Letters, vol. 11, pp. 256-259, 2012.

[3] X. Ding, B. Wang and G. He, "Research on a Millimeter-Wave Phased Array With Wide-Angle Scanning Performance," in IEEE Transactions on Antennas and Propagation, vol. 61, no. 10, pp. 5319-5324, Oct. 2013.

[4] T. Chaloun et al., "Wide-angle scanning active transmit/receive reflectarray," in IET Microwaves, Antennas & Propagation, vol. 8, no. 11, pp. 811-818, August 19 2014.

[5] S. Vaccaro, L. Diamond, D. Runyon and M. C. Vigano, "Ka-band mobility terminals enabling new services," The 8th European Conference on Antennas and Propagation (EuCAP 2014), The Hague, 2014, pp. 2617-2618.

[6] H. Fenech, S. Amos, A. Tomatis and V. Soumpholphakdy, "High throughput satellite systems: An analytical approach," in IEEE Transactions on Aerospace and Electronic Systems, vol. 51, no. 1, pp. 192-202, January 2015.

[7] Q. Luo et al., "Design and Analysis of a Reflectarray Using Slot Antenna Elements for Ka-band SatCom," in IEEE Transactions on Antennas and Propagation, vol. 63, no. 4, pp. 1365-1374, April 2015.

[8] Y. Rahmat-Samii and A. C. Densmore, "Technology Trends and Challenges of Antennas for Satellite Communication Systems," in IEEE Transactions on Antennas and Propagation, vol. 63, no. 4, pp. 1191-1204, April 2015.

[9] Zhou, Haifeng, Mingchinq Jong, and Guoqiang Lo. "Evolution of satellite communication antennas on mobile ground terminals." International Journal of Antennas and Propagation 2015 (2015).

[10] J. S. Silva, E. B. Lima, J. R. Costa, C. A. Fernandes and J. R. Mosig, "Tx-Rx Lens-Based Satellite-on-the-Move Ka-Band Antenna," in IEEE Antennas and Wireless Propagation Letters, vol. 14, pp. 1408-1411, 2015.

[11] S. B. Yeap, X. Qing and Z. N. Chen, "77-GHz Dual-Layer Transmit-Array for Automotive Radar Applications," in IEEE Transactions on Antennas and Propagation, vol. 63, no. 6, pp. 2833-2837, June 2015.

[12] Q. Luo, S. Gao and L. Zhang, "Millimeter-wave smart antennas for advanced satellite communications," 2015 IEEE MTT-S International Microwave Symposium, Phoenix, AZ, 2015, pp. 1-4.

[13] L. S. Chuan, S. Ru-Tian, and Y. P. Hon, "Ka band satellite communications design analysis and optimization," Defense, Science and Technology Agency (DSTA) Horizons 2015 [Online]. Available:https://www.dsta.gov.sg/docs/default-source/dsta-about/ka-band-satellite-communications-design-analysis-and-optimisation.pdf?sfvrsn=2.

[14] E. B. Lima, S. A. Matos, J. R. Costa, C. A. Fernandes and N. J. G. Fonseca, "Circular Polarization Wide-Angle Beam Steering at Ka-Band by In-Plane Translation of a Plate Lens Antenna," in IEEE Transactions on Antennas and Propagation, vol. 63, no. 12, pp. 5443-5455, Dec. 2015.

[15] S. Kutty and D. Sen, "Beamforming for Millimeter Wave Communications: An Inclusive Survey," in IEEE Communications Surveys & Tutorials, vol. 18, no. 2, pp. 949-973, Secondquarter 2016.

[16] R. Bonjour et al., "Ultra-Fast Millimeter Wave Beam Steering," in IEEE Journal of Quantum Electronics, vol. 52, no. 1, pp. 1-8, Jan. 2016.

[17] Z. Cao et al., "Advanced Integration Techniques on Broadband Millimeter-Wave Beam Steering for 5G Wireless Networks and Beyond," in IEEE Journal of Quantum Electronics, vol. 52, no. 1, pp. 1-20, Jan. 2016.

[18] J. Helander, K. Zhao, Z. Ying and D. Sjöberg, "Performance Analysis of Millimeter-Wave Phased Array Antennas in Cellular Handsets," in IEEE Antennas and Wireless Propagation Letters, vol. 15, pp. 504-507, 2016.

[19] Hasan, Mohamed, and Christopher Bianchi. "Ka band enabling technologies for high throughput satellite (HTS) communications." International Journal of Satellite Communications and Networking 34, no. 4 (2016): 483-501.

[20] T. Chaloun, C. Waldschmidt and W. Menzel, "Wide-angle scanning cavity antenna element for mobile Satcom applications at Ka band," 2016 10th European Conference on Antennas and Propagation (EuCAP), Davos, 2016, pp. 1-5.

[21] Rohrdantz, Benjamin, Karsten Kuhlmann, Alexander Stark, Alexander Geise, and Arne F. Jacob. "Digital beamforming antenna array with polarisation multiplexing for mobile high-speed satellite terminals at Ka-band." The Journal of Engineering 1, no. 1 (2016).

[22] H. Bayer, A. Krauss, T. Zaiczek, R. Stephan, O. Enge-Rosenblatt and M. A. Hein, "Ka-Band User Terminal Antennas for Satellite Communications [Antenna Applications Corner]," in IEEE Antennas and Propagation Magazine, vol. 58, no. 1, pp. 76-88, Feb. 2016.

[23] Fenech, Hector, Alessia Tomatis, S. Amos, V. Soumpholphakdy, and J. L. Serrano Merino. "Eutelsat HTS systems." International Journal of Satellite Communications and Networking 34, no. 4 (2016): 503-521.

[24] Z. Briqech, A. Sebak and T. A. Denidni, "Low-Cost Wideband mm-Wave Phased Array Using the Piezoelectric Transducer for 5G Applications," in IEEE Transactions on Antennas and Propagation, vol. 65, no. 12, pp. 6403-6412, Dec. 2017.

[25] D. Liu, X. Gu, C. W. Baks and A. Valdes-Garcia, "Antenna-in-Package Design Considerations for Ka-Band 5G Communication Applications," in IEEE Transactions on Antennas and Propagation, vol. 65, no. 12, pp. 6372-6379, Dec. 2017.

[26] X. Gu et al., "A multilayer organic package with 64 dual-polarized antennas for 28GHz 5G communication," 2017 IEEE MTT-S International Microwave Symposium (IMS), Honololu, HI, 2017, pp. 1899-1901.

[27] D. Liu, W. Hong, T. S. Rappaport, C. Luxey and W. Hong, "What will 5G Antennas and Propagation Be?," in IEEE Transactions on Antennas and Propagation, vol. 65, no. 12, pp. 6205-6212, Dec. 2017.

[28] O. Jo, J. Kim, J. Yoon, D. Choi and W. Hong, "Exploitation of Dual-Polarization Diversity for 5G Millimeter-Wave MIMO Beamforming Systems," in IEEE Transactions on Antennas and Propagation, vol. 65, no. 12, pp. 6646-6655, Dec. 2017.

[29] B. Sadhu et al., "A 28-GHz 32-Element TRX Phased-Array IC With Concurrent Dual-Polarized Operation and Orthogonal Phase and Gain Control for 5G Communications," in IEEE Journal of Solid-State Circuits, vol. 52, no. 12, pp. 3373-3391, Dec. 2017.

[30] B. Yu, K. Yang, C. Sim and G. Yang, "A Novel 28 GHz Beam Steering Array for 5G Mobile Device With Metallic Casing Application," in IEEE Transactions on Antennas and Propagation, vol. 66, no. 1, pp. 462-466, Jan. 2018.

[31] J. Zhao, F. Gao, Q. Wu, S. Jin, Y. Wu and W. Jia, "Beam Tracking for UAV Mounted SatCom on-the-Move With Massive Antenna Array," in IEEE Journal on Selected Areas in Communications, vol. 36, no. 2, pp. 363-375, Feb. 2018.

[32] Li, Y., Xiao, S. and Guo, J., 2018. A Review of Wideband Wide-Angle Scanning 2-D Phased Array and Its Applications in Satellite Communication. Journal of Communications and Information Networks, 3(1), pp.21-3.

[33] G. Raney, B. Unruh, R. Lovestead and B. Winther, "64-Element 28 Gigahertz Phased Array 5G Prototyping Platform," 2018 11th Global Symposium on Millimeter Waves (GSMM), Boulder, CO, USA, 2018, pp. 1-4.

[34] J. M. McKinnis, I. Gresham and R. Becker, "Figures of Merit for Active Antenna Enabled 5G Communication Networks," 2018 11th Global Symposium on Millimeter Waves (GSMM), Boulder, CO, USA, 2018, pp. 1-7.

[35] K. Kibaroglu, M. Sayginer and G. M. Rebeiz, "A Low-Cost Scalable 32-Element 28-GHz Phased Array Transceiver for 5G Communication Links Based on a2×2Beamformer Flip-Chip Unit Cell," in IEEE Journal of Solid-State Circuits, vol. 53, no. 5, pp. 1260-1274, May 2018.

[36] M. Stoneback and K. Madsen, "A Planar All-Silicon 256-Element Ka-band Phased Array for High-Altitude Platforms (HAPs) Application," 2018 IEEE/MTT-S International Microwave Symposium - IMS, Philadelphia, PA, USA, 2018, pp. 783-786.

[37] F. Tabarani, L. Boccia, T. Purtova, A. Shamsafar, H. Schumacher and G. Amendola, "0.25-μmBiCMOS System-on-Chip for K-/Ka-Band Satellite Communication Transmit–Receive Active Phased Arrays," in IEEE Transactions on Microwave Theory and Techniques, vol. 66, no. 5, pp. 2325-2339, May 2018.

[38] J. I. Herranz-Herruzo, A. Valero-Nogueira, M. Ferrando-Rocher, B. Bernardo, A. Vila and R. Lenormand, "Low-Cost Ka-band Switchable RHCP/LHCP Antenna Array for Mobile SATCOM Terminal," in IEEE Transactions on Antennas and Propagation, vol. 66, no. 5, pp. 2661-2666, May 2018.

[39] B. Lesur et al., "A Large Antenna Array for Ka-band Satcom-onthe-Move Applications – Accurate Modelling and Experimental Characterization," in IEEE Transactions on Antennas and Propagation.

[40] K. Kibaroglu, M. Sayginer and G. M. Rebeiz, "A Low-Cost Scalable 32-Element 28-GHz Phased Array Transceiver for 5G Communication Links Based on a2×2Beamformer Flip-

Chip Unit Cell," in IEEE Journal of Solid-State Circuits, vol. 53, no. 5, pp. 1260-1274, May 2018.

[41] http://www.c-comsat.com/solutions/ka-band-mobile-antennas/

[42] S. S. Holland, D. H. Schaubert and M. N. Vouvakis, "A 7–21 GHz Dual-Polarized Planar Ultrawideband Modular Antenna (PUMA) Array," in IEEE Transactions on Antennas and Propagation, vol. 60, no. 10, pp. 4589-4600, Oct. 2012.

[43] R. Mayo and S. Harmer, "A cost-effective modular phased array," 2013 IEEE International Symposium on Phased Array Systems and Technology, Waltham, MA, 2013, pp. 93-96.

[44] K. Bhattacharyya, "A modular approach for probe-fed and capacitively coupled multilayered patch arrays," in IEEE Transactions on Antennas and Propagation, vol. 45, no. 2, pp. 193-202, Feb. 1997.

[45] X. Ding, B. Wang and G. He, "Research on a Millimeter-Wave Phased Array With Wide-Angle Scanning Performance," in IEEE Transactions on Antennas and Propagation, vol. 61, no. 10, pp. 5319-5324, Oct. 2013.

[46] Y. Wen, B. Wang and X. Ding, "A Wide-Angle Scanning and Low Sidelobe Level Microstrip Phased Array Based on Genetic Algorithm Optimization," in IEEE Transactions on Antennas and Propagation, vol. 64, no. 2, pp. 805-810, Feb. 2016.

[47] T. Lee, D. Lee, H. Choo and G. Byun, "A Method of Substrate Shaping to Improve Gain of Active-Element Pattern for Small Arrays," in IEEE Antennas and Wireless Propagation Letters, vol. 16, pp. 1601-1604, 2017.

[48] B. Abbasi Arand, A. Bazrkar and A. Zahedi, "Design of a Phased Array in Triangular Grid with an Efficient Matching Network and Reduced Mutual Coupling for Wide-Angle Scanning," in IEEE Transactions on Antennas and Propagation, vol. 65, no. 6, pp. 2983-2991, June 2017.

[49] Soroush Rasti Boroujeni, Hussam Al-Saedi, Mohammad-Reza Nezhad-Ahmadi, Safieddin Safavi-Naeini, “Investigation of active load pulling effect on radiated power of the antenna elements in a finite phased array transmitter for satellite communication” presented at the 2018 IEEE International Symposium on Antennas and Propagation and USNC-URSI Radio Science Meeting.

[50] E. Adas, F. De Flaviis and N. G. Alexopoulos, "Realization of Scan Blindness Free Finite Microstrip Phased Arrays Based on Mode-Free Radiating Electromagnetic Bandgap Materials," in IEEE Transactions on Antennas and Propagation, vol. 66, no. 7, pp. 3375-3382, July 2018.

[51] Al-Saedi, H., Abdel-Wahab, W., Gigoyan, S., Taeb, A., & Safavi-Naeini, S. (2018). A low-cost wideband phase shifter for two-way mm-wave phased array antenna system. International Journal of Microwave and Wireless Technologies, 10(1), 77-86.

[52] T. Merkle and R. Götzen, "Millimeter-Wave Surface Mount Technology for 3-D Printed Polymer Multichip Modules," in IEEE Transactions on Components, Packaging and Manufacturing Technology, vol. 5, no. 2, pp. 201-206, Feb. 2015.

[53] B. K. Tehrani, B. S. Cook and M. M. Tentzeris, "Inkjet Printing of Multilayer Millimeter-Wave Yagi-Uda Antennas on Flexible Substrates," in IEEE Antennas and Wireless Propagation Letters, vol. 15, pp. 143-146, 2016.

[54] B. Zhang, Y. Guo, H. Zirath and Y. P. Zhang, "Investigation on 3-D-Printing Technologies for Millimeter- Wave and Terahertz Applications," in Proceedings of the IEEE, vol. 105, no. 4, pp. 723-736, April 2017.

[55] R. Bahr, B. Tehrani and M. M. Tentzeris, "Exploring 3-D Printing for New Applications: Novel Inkjet- and 3-D-Printed Millimeter-Wave Components, Interconnects, and Systems," in IEEE Microwave Magazine, vol. 19, no. 1, pp. 57-66, Jan.-Feb. 2018.

[56] L. Baggen, M. Böttcher, S. Otto, O. Litschke, R. Gieron and S. Holzwarth, "Phased array technology by IMST: A comprehensive overview," 2013 IEEE International Symposium on Phased Array Systems and Technology, Waltham, MA, 2013, pp. 21-28.

[57] Recommendation, I. T. U. R. S. "524-9 “Maximum Permissible Levels of Off-Axis eirp Density from Earth Stations in Geostationary-Satellite Orbit Networks Operating in the Fixed-Satellite Service Transmitting in the 6 GHz, 13 GHz, 14 GHz and 30 GHz Frequency Bands,”."

[58] L. Gonzalez and R. E. Greel, "“A regulatory study and recommendation for EIRP Spectral Density requirement/allowance for SOTM terminals at Ka-Band on WGS system”," 2010 - MILCOM 2010 MILITARY COMMUNICATIONS CONFERENCE, San Jose, CA, 2010, pp. 1992-1997.

[59] C. McLain, L. Gonzalez and W. Hall, "Relative performance of mobile networks in the Ku, commercial Ka and government Ka bands," 2011 - MILCOM 2011 Military Communications Conference, Baltimore, MD, 2011, pp. 2081-2086.

[60] Arinc 791-1” Mark I Aviation Ku-Band And Ka-Band Satellite Communication System Part 1 Physical Installation And Aircraft Interfaces”.

[61] Garg, Ramesh. Microstrip antenna design handbook. Artech house, 2001.

[62] Garcia-Aguilar, J. Inclan-Alonso, L. Vigil-Herrero, J. Fernandez-Gonzalez and M. Sierra-Perez, "Low-Profile Dual Circularly Polarized Antenna Array for Satellite Communications in the X Band," in IEEE Transactions on Antennas and Propagation, vol. 60, no. 5, pp. 2276-2284, May 2012.

[63] D. M. Pozar, "Analysis of an infinite phased array of aperture coupled microstrip patches," in IEEE Transactions on Antennas and Propagation, vol. 37, no. 4, pp. 418-425, April 1989.

[64] S. D. Targonski and D. M. Pozar, "Design of wideband circularly polarized aperture-coupled microstrip antennas," in IEEE Transactions on Antennas and Propagation, vol. 41, no. 2, pp. 214-220, Feb. 1993.

[65] C. -. Huang, "Designs for an aperture-coupled compact circularly polarised microstrip antenna," in IEE Proceedings - Microwaves, Antennas and Propagation, vol. 146, no. 1, pp. 13-16, Feb. 1999.

[66] K. Davies and E. K. Smith, “Ionospheric effects on satellite land mobile systems,” IEEE Antennas and Propagation Magazine, vol. 44, no. 6, pp. 24–31, Dec 2002.

[67] J. L. Volakis, R. C. Johnson, and H. Jasik, Antenna Engineering Handbook, 4th ed. McGraw—Hill Book Company, 2007.

[68] B. R. Elbert, Introduction to Satellite Communication, 2nd ed. Artech House, 1999.

[69] Balanis, C. A. (2016). Antenna theory: analysis and design. John Wiley & Sons, ch.6.

[70] R. Cox and W. Rupp, "Circularly polarized phased array antenna element," in IEEE Transactions on Antennas and Propagation, vol. 18, no. 6, pp. 804-807, November 1970.

[71] X. Tang, X. Qing, W. Liu, Nasimuddin, G. Zhai and Z. N. Chen, "Effect of mutual coupling on Ka-band circularly polarized beam scanning antenna array," 2016 IEEE International Symposium on Antennas and Propagation (APSURSI), Fajardo, 2016, pp. 2193-2194.

[72] R. R. George, A. T. Castro and S. K. Sharma, "Investigations of an aperture coupled circular polarized via walls backed microstrip patch linear array antenna for beam steering performance," 2017 USNC-URSI Radio Science Meeting (Joint with AP-S Symposium), San Diego, CA, 2017, pp. 119-120.

[73] W. E. I. Liu, Z. N. Chen and X. Qing, "Compact wideband metasurface-based circularly polarized antenna for Ka-band phased array," 2017 IEEE-APS Topical Conference on Antennas and Propagation in Wireless Communications (APWC), Verona, 2017, pp. 17-20.

[74] D. Parker and D. C. Zimmermann, "Phased arrays - part 1: theory and architectures," in IEEE Transactions on Microwave Theory and Techniques, vol. 50, no. 3, pp. 678-687, Mar 2002.

[75] Norvell, B. R., Hancock, R. J., Smith, J. K., Pugh, M. L., Theis, S. W., & Kriatkofsky, J. (1999). Micro electro mechanical switch (MEMS) technology applied to electronically scanned arrays for space based radar. In Aerospace Conference, 1999. Proceedings. 1999 IEEE (Vol. 3, pp. 239-247). IEEE.

[76] Collin, Robert E. Antennas and radiowave propagation. McGraw-Hill, 1985.

[77] R. R. Romanofsky, "Advances in Scanning Reflectarray Antennas Based on Ferroelectric Thin-Film Phase Shifters for Deep-Space Communications," in Proceedings of the IEEE, vol. 95, no. 10, pp. 1968-1975, Oct. 2007.

[78] J. Huang and J. A. Encinar, Reflectarray Antennas. Hoboken, NJ: Wiley, 2008.

[79] S. V. Hum and J. Perruisseau-Carrier, "Reconfigurable Reflectarrays and Array Lenses for Dynamic Antenna Beam Control: A Review," in IEEE Transactions on Antennas and Propagation, vol. 62, no. 1, pp. 183-198, Jan. 2014.

[80] P. Nayeri, F. Yang and A. Z. Elsherbeni, "Beam-Scanning Reflectarray Antennas: A technical overview and state of the art.," in IEEE Antennas and Propagation Magazine, vol. 57, no. 4, pp. 32-47, Aug. 2015.

[81] M. H. Dahri, M. H. Jamaluddin, M. I. Abbasi and M. R. Kamarudin, "A Review of Wideband Reflectarray Antennas for 5G Communication Systems," in IEEE Access, vol. 5, pp. 17803-17815, 2017.

[82] M. Niroo-Jazi, H. Al-Saedi, S. Gigoyan and S. Safavi-Naeini, "Design and analysis of reconfigurable reflectarray antennas for Ka-band satellite communications on the move," 2016 17th International Symposium on Antenna Technology and Applied Electromagnetics (ANTEM), Montreal, QC, 2016, pp. 1-2.

[83] Baggen, L., Böttcher, M., Otto, S., Litschke, O., Gieron, R., & Holzwarth, S. (2013, October). Phased array technology by IMST: A comprehensive overview. In Phased Array Systems & Technology, 2013 IEEE International Symposium on (pp. 21-28). IEEE.

[84] Sang-Gyu Kim and Kai Chang, "Ultra wideband 8 to 40 GHz beam scanning phased array using antipodal exponentially-tapered slot antennas," 2004 IEEE MTT-S International Microwave Symposium Digest (IEEE Cat. No.04CH37535), Fort Worth, TX, USA, 2004, pp. 1757-1760 Vol.3.

[85] Chia-Chan Chang, C. W. Domier and N. C. Luhmann, "Microwave beam focusing/shaping phased antenna arrays," 2004 IEEE MTT-S International Microwave Symposium Digest (IEEE Cat. No.04CH37535), Fort Worth, TX, USA, 2004, pp. 1765-1768 Vol.3.

[86] Lu Yang, C. W. Domier and N. C. Luhmann, "Ka-Band True Time Delay E-plane Beam Scanning and Broadening Phased Array System using Antipodal Elliptically-Tapered Slot Antennas," 2006 IEEE Antennas and Propagation Society International Symposium, Albuquerque, NM, 2006, pp. 2213-2216.

[87] Lu Yang, N. Ito, C. W. Domier, N. C. L. Jr and A. Mase, "20 to 40 GHz Beam Shaping/Steering Phased Antenna Array System using Fermi Tapered Slot Antennas," 2007 IEEE/MTT-S International Microwave Symposium, Honolulu, HI, 2007, pp. 1887-1890.

[88] L. Yang, N. Ito, C. W. Domier, N. C. Luhmann and A. Mase, "18–40-GHzBeam-Shaping/Steering Phased Antenna Array System Using Fermi Antenna," in IEEE Transactions on Microwave Theory and Techniques, vol. 56, no. 4, pp. 767-773, April 2008.

[89] D. Jung, C. H. Kim and K. Chang, "Broadband 8 to 18 GHz phased array system for communications," 2012 Asia Pacific Microwave Conference Proceedings, Kaohsiung, 2012, pp. 406-408.

[90] M. A. Ashraf, S. Alshebeili, M. Alkanhal and A. R. Sebak, "Ultra wideband phased array antenna using slow wave microstrip dielectric loaded phase shifters," 2014 16th International Symposium on Antenna Technology and Applied Electromagnetics (ANTEM), Victoria, BC, 2014, pp. 1-2.

[91] C. Liu and S. V. Hum, "An Electronically Tunable Single-Layer Reflectarray Antenna Element With Improved Bandwidth," in IEEE Antennas and Wireless Propagation Letters, vol. 9, pp. 1241-1244, 2010.

[92] M. Mavridou, K. Konstantinidis and A. P. Feresidis, "Continuously Tunable mm-Wave High Impedance Surface," in IEEE Antennas and Wireless Propagation Letters, vol. 15, pp. 1390-1393, 2016.

[93] K. K. Karnati, Y. Shen, M. E. Trampler, S. Ebadi, P. F. Wahid and X. Gong, "A BST-Integrated Capacitively Loaded Patch for ${K_a}$- and ${X}$-band Beamsteerable Reflectarray Antennas in Satellite Communications," in IEEE Transactions on Antennas and Propagation, vol. 63, no. 4, pp. 1324-1333, April 2015.

[94] K. K. Karnati, M. E. Trampler and X. Gong, "A Monolithically BST-Integrated K_{a} -Band Beamsteerable Reflectarray Antenna," in IEEE Transactions on Antennas and Propagation, vol. 65, no. 1, pp. 159-166, Jan. 2017.

[95] Wu, J., Lou, J., Li, M., Yang, G., Yang, X., Adams, J., and Sun, N. X., “ Compact low-loss, wideband, and high-power handling phase shifters with piezoelectric transducer-controlled

metallic perturber," EEE Transactions on Microwave Theory and Techniques, vol. 60, no. 6, pp. 1587-1594, June 2012.

[96] Pillans, L. Coryell, A. Malczewski, C. Moody, F. Morris and A. Brown, "Advances in RF MEMS phase shifters from 15 GHz to 35 GHz," IEEE International Microwave Symposium Digest (MTT), Montreal, QC, Canada, 2012.

[97] S. Dey and S. K. Koul, "Reliability Analysis of Ku-Band 5-bit Phase Shifters Using MEMS SP4T and SPDT Switches," IEEE Transactions on Microwave Theory and Techniques, vol. 63, no. 12, pp. 3997-4012, Dec. 2015.

[98] S. Abdellatif, A. Abdel Aziz, R. R. Mansour and S. Safavi-Naeini, "Low-loss compact MEMS phase shifter for phased array antennas," Electronics Letters, vol. 51, no. 15, pp. 1142-1144, 2015.

[99] Chicherin, D., Sterner, M., Lioubtchenko, D., Oberhammer, J., and Räisänen, A. V., "Analog-type millimeter-wave phase shifters based on MEMS tunable high-impedance surface and dielectric rod waveguide" International Journal of Microwave and Wireless Technologies, 533-538, 2005.

[100] Gyeong-Seop Shin; Jae-Sun Kim; Hyun-Myung Oh; Sunkyu Choi; Chul Woo Byeon; Ju Ho Son; Jeong Ho Lee; Choul-Young Kim, "Low Insertion Loss, Compact 4-bit Phase Shifter in 65 nm CMOS for 5G Applications," IEEE Microwave and Wireless Components Letters, vol.26, no.1, pp.37-39, Jan. 2016.

[101] Li, J., Shu, R., & Gu, Q. J., "10 GHz CMOS hybrid reflective-type phase shifter with enhanced phase shifting range," Electronics Letters, vol. 51, no. 23, pp. 1935-1937, 2015.

[102] Wang, C. W., Wu, H. S., and Tzuang, C. K. C.," CMOS passive phase shifter with group-delay deviation of 6.3 ps at K-band," IEEE Transactions on Microwave Theory and Techniques, vol. 59, no. 7, pp. 1778-1786, July 2011.

[103] Jin, C., Okada, E., Faucher, M., Ducatteau, D., Zaknoune, M., and Pavlidis, D., "A GaN Schottky Diode-based analog phase shifter MMIC," European Microwave Integrated Circuit Conference (EuMIC), Rome, pp. 96-99, 2014.

[104] Lambard, T., Lafond, O., Himdi, M., Jeuland, H., and Bolioli, S, "A novel analog 360 phase shifter design in Ku and Ka bands," European Conference on Antennas and Propagation (EuCAP), Barcelona, Spain, pp. 1-4, 2010.

[105] De Paolis, R., Payan, S., Maglione, M., Guegan, G., and Coccetti, F., " High-Tunability and High Q-Factor Integrated Ferroelectric Circuits up to Millimeter Waves," IEEE Transactions on Microwave Theory and Techniques, vol. 63, no. 8, pp. 2570-2578, Aug. 2015.

[106] Yang, X., Gao, Y., Wu, J., Zhou, Z., Beguhn, S., Nan, T., and Sun, N. X.,"Voltage Tunable Multiferroic Phase Shifter with YIG/PMN-PT Heterostructure,", IEEE Microwave and Wireless Components Letters, vol. 24, no. 3, pp. 191-193, March 2014.

[107] Zhang, L. Y., Laur, V., Pothier, A., Simon, Q., Laurent, P., Martin, N., and Tanné, G., "KTN ferroelectrics-based microwave tunable phase shifter." Microwave and Optical Technology Letters, vol. 52(5), pp. 1148-1150, 2010.

[108] Zhao, Z., Wang, X., Choi, K., Lugo, C., & Hunt, A. T.," Ferroelectric phase shifters at 20 and 30 GHz," IEEE Transactions on Microwave Theory and Techniques, vol. 55, no. 2, pp. 430-437, Feb. 2007.

[109] Jost, M., Strunck, S., Heunisch, A., Wiens, A., Prasetiadi, A. E., Weickhmann, C., and Follmann, R.,"Continuously tuneable liquid crystal based stripline phase shifter realised in LTCC technology," European Microwave Conference (EuMC), Paris, 2015, pp. 1260-1263.

[110] Sebastian strunck et al, "Reliability study of a tunable Ka-band SIW-phase shifter based on liquid crystal in LTCC-technology", International Journal of Microwave and Wireless Technologies, 2014.

[111] Bulja, S., Mirshekar-Syahkal, D., James, R., Day, S. E., and Fernández, F. A. , "Measurement of dielectric properties of nematic liquid crystals at millimeter wavelength," IEEE Transactions on Microwave Theory and Techniques, vol. 58, no. 12, pp. 3493-3501, Dec. 2010.

[112] Romano, P., Araromi, O., Rosset, S., Shea, H., and Perruisseau-Carrier J., "Tunable millimeter-wave phase shifter based on dielectric elastomer actuation," Applied Physics Letters, 104(2), 2014.

[113] Kim, C. H., and Chang, K. ," A reflection-type phase shifter controlled by a piezoelectric transducer," Microwave and Optical Technology Letters, 53(4), pp.938-940, 2011.

[114] Kim, S. G., Yun, T. Y., and Chang, K,"Time-delay phase shifter controlled by piezoelectric transducer on coplanar waveguide," IEEE Microwave and Wireless Components Letters, vol. 13, no. 1, pp. 19-20, Jan. 2003.

[115] Yang, G. M., and Sun, N. X.," Tunable Ultra-wideband Phase Shifters With Magnetodielectric Disturber Controlled by a Piezoelectric Transducer," IEEE Transactions on Magnetics, vol. 50, no. 11, pp. 1-4, Nov. 2014.

[116] A.S. Abdellatif, M. Faraji-Dana, N. Ranjkesh, A. Taeb, M. Fahimnia, S. Gigoyan, and S. Safavi-Naeini, "Low Loss,Wideband, and Compact CPW-Based Phase Shifter for Millimeter-Wave Applications," IEEE Transactions on Microwave Theory and Techniques, vol. 62,no. 12, Dec. 2014.

[117] Abdellatif, A.S.; Aziz, A.Abdel; Ranjkesh, N.; Taeb, A.; Gigoyan, S.; Mansour, R.R.; Safavi-Naeini, S., "Wide-band phase shifter for mmWave phased array applications," Global Symposium On Millimeter Waves (GSMM), pp.1,3, 25-27 May 20.

[118] J. Liu et al., "Single-Feed Circularly Polarized Aperture-Coupled Stack Antenna With Dual-Mode Square Loop Radiator," in IEEE Antennas and Wireless Propagation Letters, vol. 9, pp. 887-890, 2010.

[119] Chang, K. and Hsieh, L.H., 2004. Microwave ring circuits and related structures (Vol. 156). John Wiley & Sons, pp: 29-40.

[120] Liang Shen, "The elliptical microstrip antenna with circular polarization," in IEEE Transactions on Antennas and Propagation, vol. 29, no. 1, pp. 90-94, January 1981.

[121] X. Zhang, D. Xue, L. Ye, Y. Pan and Y. Zhang, "Compact Dual-Band Dual-Polarized Interleaved Two-Beam Array With Stable Radiation Pattern Based on Filtering Elements," in IEEE Transactions on Antennas and Propagation, vol. 65, no. 9, pp. 4566-4575, Sept. 2017.

[122] N. Kumprasert, "Theoretical study of dual-resonant frequency and circular polarization of elliptical microstrip antennas," IEEE Antennas and Propagation Society International Symposium. Transmitting Waves of Progress to the Next Millennium. 2000 Digest. Held in conjunction with: USNC/URSI National Radio Science Meeting (C, Salt Lake City, UT, 2000, pp. 1015-1020 vol.2.

[123] Wolff, C. Günner, J. Kassner, R. Kulke and P. Uhlig, "New Heights for Satellites: LTCC Multilayer Technology for Future Satellites," in IEEE Microwave Magazine, vol. 19, no. 1, pp. 36-47, Jan.-Feb. 2018.

[124] S. K. Padhi, N. C. Karmakar, C. L. Law and S. Aditya, "A dual polarized aperture coupled circular patch antenna using a C-shaped coupling slot," in IEEE Transactions on Antennas and Propagation, vol. 51, no. 12, pp. 3295-3298, Dec. 2003.

[125] Ibrahim, H. Shaman and K. Sarabandi, "A Sub-THz Rectangular Waveguide Phase Shifter Using Piezoelectric-Based Tunable Artificial Magnetic Conductor," in IEEE Transactions on Terahertz Science and Technology.

[126] https://www.thorlabs.com/drawings/624e3d7f7e50d6a9-9EB49D4A-C790-7148-66CF972C9F125FA7/AE0203D08F-SpecSheet.pdf.

[127] Zárate, Juan José, Giordano Tosolini, Simona Petroni, Massimo De Vittorio, and Herbert Shea. "Optimization of the force and power consumption of a microfabricated magnetic actuator." Sensors and Actuators A: Physical, vol. 234, pp. 57-64, October 2015.

[128] Farid Rahman, B. M., Ralu Divan, Hanqiao Zhang, Daniel Rosenmann, Yujia Peng, Xuehe Wang, and Guoan Wang. "High performance tunable slow wave elements enabled with nano-patterned permalloy thin film for compact radio frequency applications." Journal of Applied Physics, vol. 115, no. 17. pp. 17A508-1-3, 2014.

[129] P. Hannan and M. Balfour, "Simulation of a phased-array antenna in waveguide," in IEEE Transactions on Antennas and Propagation, vol. 13, no. 3, pp. 342-353, May 1965.

[130] H. Al-Saedi, J. K. Ali, W. M. Abdel-Wahab, S. Gigoyan and S. Safavi-Naeini, "A dual circularly polarized patch antenna for broadband millimeter wave (MMW) communication systems," 2016 IEEE International Symposium on Antennas and Propagation (APSURSI), Fajardo, 2016, pp. 593-594.

[131] Hussam Al-Saedi, Jawad Al Attari, Wael M. Abdel Wahab, Raj Mittr, and Safieddin Safavi-Naeini "Single-feed Dual-band Aperture-coupled Antenna for 5G applications" presented at the 18th International Symposium on Antenna Technology and Applied Electromagnetics ANTEM.

[132] M. Fakharzadeh, "Optical and Microwave beamforming for phased array antennas," Ph.D. dissertation, Univ. Waterloo, Waterloo, ON, Canada, 2008.

Appendix A
List of Papers

Journal Papers

J1. **Al-Saedi, H**., Abdel-Wahab, W., Gigoyan, S., Taeb, A., & Safavi-Naeini, S. "A low-cost wideband phase shifter for two-way mm-wave phased array antenna system," in International Journal of Microwave and Wireless Technologies, vol. 10, no. 1, pp. 77-86, 2018.

J2. **H. Al-Saedi**, W. M. Abdel-Wahab, S. Gigoyan, R. Mittra and S. Safavi-Naeini, "Ka-Band Antenna with High Circular Polarization Purity and Wide AR Beamwidth," in IEEE Antennas and Wireless Propagation Letters, vol. 17, no. 9, pp.1697-1701, Sept. 2018.

J3. Abdel-Wahab WM, **Al-Saedi H**, Safavi-Naeini S. "RWG-integrated SIW splitter for large scale SATCOM phased array applications," in Microwave and Optical Technology Letters, vol. 59, no. 10, pp.59:2675–2680, 2017.

J4. **Al-Saedi Hussam**, Gigoyan Suren, Abdel-Wahab Wael, Palizban Ardeshir, Taeb Aidin, Ehsandar Ahmad, Nenasheva, Elizaveta, Safavi-Naeini Safieddin," A Low-cost Ka-band Circularly Polarized Passive Phased-Array Antenna for Mobile Satellite Applications" **Accepted** on October 14, 2018 in IEEE Transactions on Antennas & Propagation.

J5. **Al-Saedi Hussam**, Gigoyan Suren, Abdel-Wahab Wael, Palizban Ardeshir, Taeb Aidin, Safavi-Naeini Safieddin," A Low Power Consumption and High Figure of Merit mm-W Phase Shifter" **1st revision will be submitted soon** to IEEE Microwave and Wireless Components Letters.

J6. **Al-Saedi Hussam**, Abdel-Wahab Wael, Raeis-Zadeh S. Mohsen, Alian Ehsan, Palizban Ardeshir, Ehsandar Ahmad, Chen Guoyan, Rasti Boroujeni Soroush, Nezhad-Ahmadi Mohammad-Reza, Safavi-Naeini Safieddin," An Integrated Circularly Polarized Transmitter Active Phased-Array Antenna for Emerging Ka-Band Satellite Mobile Terminals" **submitted** on April 5, 2018 to IEEE Transactions on Antennas & Propagation.

J7. **Al-Saedi Hussam**, Gigoyan Suren, Abdel-Wahab Wael, Mittr Raj, Safavi-Naeini Safieddin," Tunable Ka-Band Reflectarray antenna element" **submitted** on June 26, 2018 to IET Microwaves, Antennas & Propagation.

Conference Papers

C1. **A. Hussam**, F. Mohmmad, W. M. Abdel-Wahab, G. Rafi and S. Safavi-Naeini, "A 4×4 circularly polarized aperture coupled antenna array for Ka-band satellite communication," 2015 IEEE International Symposium on Antennas and Propagation & USNC/URSI National Radio Science Meeting, Vancouver, BC, 2015, pp. 1896-1897.

C2. **H. Al-Saedi**, J. K. Ali, W. M. Abdel-Wahab, S. Gigoyan and S. Safavi-Naeini, "A dual circularly polarized patch antenna for broadband millimeter wave (MMW) communication systems," 2016 IEEE International Symposium on Antennas and Propagation (APSURSI), Fajardo, 2016, pp. 593-594.

C3. M. Niroo-Jazi, **H. Al-Saedi**, S. Gigoyan and S. Safavi-Naeini, "Design and analysis of reconfigurable reflectarray antennas for Ka-band satellite communications on the move," 2016 17th International Symposium on Antenna Technology and Applied Electromagnetics (ANTEM), Montreal, QC, 2016, pp. 1-2.

C4. **H. Al-Saedi**, W. Abdel-Wahab, S. M. Raeis-Zadeh, S. Gigoyan and S. Safavi-Naeini, "A wide axial ratio beamwidth circularly polarized antenna for Ka-band satellite on the move (SOTM) phased array applications," 2017 IEEE International Symposium on Antennas and Propagation & USNC/URSI National Radio Science Meeting, San Diego, CA, 2017, pp. 2557-2558.

C5. **Hussam Al-Saedi**, Wael Abdel-Wahab, Mohsen Raeis-Zadeh, Suren Gigoyan, Safieddin Safavi-Naeini, "An Ultra-Wideband Modified Aperture-Coupled Millimeter-Wave Reflectarray Antenna" **presented** at the 2018 IEEE International Symposium on Antennas and Propagation and USNC-URSI Radio Science Meeting, Boston, MA, 2018.

C6. Soroush Rasti Boroujeni, **Hussam Al-Saedi**, Mohammad-Reza Nezhad-Ahmadi, Safieddin Safavi-Naeini, "Investigation of active load pulling effect on radiated power of the antenna elements in a finite phased array transmitter for satellite communication" **presented** at the 2018 IEEE International Symposium on Antennas and Propagation and USNC-URSI Radio Science Meeting, Boston, MA, 2018.

C7. **Hussam Al-Saedi**, Wael M. Abdel-Wahab, S. Mohsen Raeis-Zadeh, Ehsan Alian, Ardeshir Palizban, Ahmad Ehsandar, Guoyan Chen, Mohammad-Reza Nezhad-Ahmadi, and Safieddin Safavi-Naeini, "Active Phased-Array Antennas for Ka/K Mobile Satellite Communications" **presented** at the 18th International Symposium on Antenna Technology and Applied Electromagnetics ANTEM, Waterloo, ON., 2018.

C8. **Hussam Al-Saedi**, Suren Gigoyan, Wael M. Abdel-Wahab, Ardeshir Palizban, and Safieddin Safavi-Naeini "A Continuous 2π Phase Shifter for Ka-Band Applications" **presented** at the European Microwave Week, Madrid, Spain, 2018.

C9. Wael M. Abdel-Wahab, **H. Al-Saedi**, M. Raeiszadeh, E. Alian, G. Chen, A. Ehsandar, N. Ghafarian, H. El-Sawaf, A. Palizban, M. R. Nezhad-Ahmadi, S. Safavi-Naeini, "A Modular Architecture for Low Cost Phased Array Antenna System for Ka-Band Mobile Satellite Communication" **presented** at the 36th International Communications Satellite Systems Conference (ICSSC), Niagara, ON., 2018.